Studies of Active Galactic Nuclei with the MAGIC telescopes

Dissertation

zur Erlangung des akademischen Grades

doctor rerum naturalium

(Dr. rer. nat.)

im Fach Physik

eingereicht an der

Mathematisch-Naturwissenschaftlichen Fakultät

der Humboldt-Universität zu Berlin

von

Frau Dott. Mag. Gessica De Caneva

Präsident der Humboldt-Universität zu Berlin

Prof. Dr. Jan-Hendrik Olbertz

Dekan der Mathematisch-Naturwissenschaftlichen Fakultät

Prof. Dr. Elmar Kulke

Gutachter/innen:
1. Dr. Elisa Bernardini
2. Prof. Dr. Barbara De Lotto
3. Prof. Dr. Thomas Lohse

Tag der mündlichen Prüfung: 27.01.2015

Abstract

This PhD thesis addresses the problem of understanding the very high energy emission from active galactic nuclei as detected with the MAGIC telescopes.

Active galactic nuclei are galaxies which exhibit an usual activity in their nuclear region. These objects are powered by the release of gravitational energy of stellar material falling into a black hole, located in their core. Two highly collimated, opposed jets extend from the central region outwards, covering distances of several parsecs. If one of the two jets points towards the observer, the source is called a blazar. Objects belonging to this class emit non-thermal radiation extending for more than ten orders of magnitudes, from radio frequencies up to very high energy γ rays. While observations of blazars in the optical and radio bands were extensively performed in the past century, only in the last decades γ-ray observations became possible. Very high energy γ rays ($100\,\mathrm{GeV} \lesssim E \lesssim 100\,\mathrm{TeV}$) are detected on Earth's ground using atmospheric Cherenkov telescopes. With this indirect technique the Cherenkov radiation emitted by air showers generated in the interaction between energetic γ rays and molecules of the atmosphere is measured. The MAGIC (Major Atmospheric Gamma-ray Imaging Cherenkov) telescopes are a system of two Cherenkov telescopes, located on the Canary island of La Palma (Spain) in the observatory "Roque de Los Muchachos". Being located in the Northern hemisphere, MAGIC is optimally suited for observing the extragalactic sky.

In this thesis the analysis of MAGIC observations of three different blazars is presented: the newly discovered very high energy blazar 1ES 1727+502, and the two known objects 3C 279 and PKS 1510-089. The source 1ES 1727+502 belongs to the subclass of BL Lac objects, which is the most numerous class of extragalactic very high energy emitters. The observations presented here show that this source has similar properties to the ones of the same class. The source 1ES 1727+502 was selected for observations from an X-ray catalogue and was observed even if no high activity states were reported at lower energies. For this reason, this discovery proves the importance of using several criteria for the selection of very high energy observation targets. The other two objects, 3C 279 and PKS 1510-089, belong to the subclass of flat spectrum radio quasars. They are blazars with a larger density of low energy radiation and stellar material in their central region. Their phenomenology

presents some differences with respect to the one observed in BL Lac objects. We count only three representatives of this class in the very high energy domain. Their detection is indeed critical because during quiescent states they have low flux levels at very high energies, as indicated by an extrapolation of the steep spectra with a cut-off measured in the *Fermi*-LAT band. During flaring states, flat spectrum radio quasars exhibit flux enhancements of orders of magnitudes and short time scales. Observations during such states, difficult to catch, are extremely interesting because extreme processes are taking place.

Besides the three blazars, the results of MAGIC observations for the source RGB 0505+612, an active galactic nucleus of an unknown type and not detected at VHE γ rays, are shown. These observations were triggered by a neutrino alert sent by the IceCube Collaboration. MAGIC follow-up observations did not lead to a detection of the source and an upper limit on the flux is derived which can be used to constrain and test emission models.

This thesis is structured in the following manner: in Chapter 1 a brief overview of γ-ray astrophysics is given. Galactic and extragalactic γ-ray emitters are presented and the mechanisms responsible for the production of γ rays are briefly summarised. In Chapter 2 the experimental techniques used for the detection of very high energy γ rays are outlined. After an overview of the phenomenon of air showers, MAGIC telescopes, their hardware and the standard analysis chain, are explained in detail. In Chapter 3 the phenomenology of active galactic nuclei and blazars is outlined and instruments operating at lower energy bands, whose observations are often combined with MAGIC data, are listed. In Chapter 4 the analysis of MAGIC data of the sources 1ES 1727+502, 3C 279 and PKS 1510-089 is presented. Very high energy observations are complemented with measurements at lower energies into the broad band spectral energy distribution. Interpretations of the observed behaviours are discussed. In Chapter 5 the results obtained in the previous chapter are examined and compared with historical observations, highlighting open questions and problems which should be addressed by future studies. In Appendix B the results obtained for the neutrino follow-up observations of the source RBG 0505+612 are presented. These results prove that the follow-up program of neutrino triggers is in operation and a multimessenger approach can be adopted to study active galactic nuclei.

Zusammenfassung

Schwerpunkt dieser Arbeit ist die Emission von hochenergetischer Gammastrahlung aus Aktiven Galaxienkernen, anhand von Beobachtungen mit den MAGIC Teleskopen.

Aktive Galaxien sind Galaxien, in deren Kernen eine außergewöhnlich hohe Aktivität stattfindet, die durch die Freisetzung von Gravitationsenergie der Stellarmaterie, die in das zentrale Schwarze Loch fällt, entsteht. Zwei diametral entgegengesetzte Jets strömen aus dem Kern, die eine Entfernung von mehreren parsec erreichen. Falls einer von diesen Jets zum Beobachter zeigt, wird der aktive Galaxienkern als Blazar bezeichnet. Diese Klasse von Objekten emittiert nicht-thermische Strahlung deren Frequenzen mehr als zehn Größenordnungen umfasst: von Radiowellen bis hin zu sehr hochenergetischer Gammastrahlung. Während Blazare im optischen und Radiowellen Bereich schon seit hundert Jahren bekannt sind, ist ihre Beobachtung im hochenergetischen Bereich erst seit einigen Jahrzehnten möglich. Die hochenergetischen Gammastrahlen ($100\,\mathrm{GeV} \lesssim E \lesssim 100\,\mathrm{TeV}$) werden am Boden mit Hilfe von Atmosphärischen-Cherenkov-Teleskopen gemessen. Diese indirekte Messmethode basiert auf der Cherenkov-Strahlung die von Luftschauern bei der Wechselwirkung von Gammastrahlen und Molekülen in der Atmosphäre erzeugt wird. Die MAGIC Teleskope sind zwei Atmosphärische-Cherenkov-Teleskope, die in dem Roque de los Muchachos Observatorium auf der Kanarischen Insel La Palma stehen. Weil sie sich auf der nördlichen Halbkugel befinden, sind sie für die Beobachtung von Extragalaktischen Objekten ideal geeignet.

In dieser Doktorarbeit wird die Analyse der MAGIC Beobachtungen von drei Blazaren präsentiert: der bisher unbekannte hochenergetische Blazar 1ES 1727+502 und die bekannten Objekte 3C 279 und PKS 1510-089. Die Quelle 1ES 1727+502 gehört zu der Unterklasse der BL Lac Objekte, die die zahlenmäßig größte Klasse an extragalaktischen hochenergetische Objekten ist. Die Ergebnisse dieser Analyse zeigen, dass 1ES 1727+502 ein typisches BL Lac Objekt ist. Diese Entdeckung beweist, wie wichtig es ist, mehrere und verschiedene Kriterien für die Auswahl von Objekten zu benutzen. Der Blazar 1ES 1727+502 wurde aus einem X-ray Katalog ausgesucht, die Datennahme war unabhängig von dem Aktivitätsstatus der anderen Energiebänder. Die Blazare 3C 279 und PKS 1510-089 gehören zu der Unterklasse

des Flat Spectrum Radio Quasars. In der zentralen Region von solchen Objekten gibt es eine hohe Dichte von niederenergetischer Strahlung und Stellarmaterie. Die Phänomenologie des Flat Spectrum Radio Quasars ist anders als die von BL Lac Objekten. Es gibt nur drei bekannte Flat Spectrum Radio Quasare. Die Entdeckung von Flat Spectrum Radio Quasaren ist schwierig, weil im leisen Zustand der hochenergetische Fluss extrapoliert aus Fermi Daten niedrig ist. Während eines Flares steigt der Fluss in sehr kurzer Zeit um mehrere Größenordnungen an, deswegen ist die Beobachtung eines Flares schwer zu realisieren aber physikalisch äußerst interessant.

Zusätzlich zu den Ergebnissen der drei Blazare werden die Ergebnisse der MAGIC Beobachtungen der Quelle RGB 0505+612, einem aktiven Galaxienkern von unbekanntem Typ, präsentiert. Es wurden keine von ihm erzeugten hochenergetischen Gammastrahlen entdeckt. Die Beobachtungen wurden durch die Information eines erhöhten Neutrinoflusses von der IceCube Collaboration ausgelöst. Aufgrund dieser Warnung beobachtete MAGIC die Quelle, konnte aber keinen Gammafluss entdecken. Daher kann man nur eine obere Abschätzung des Flusses aus diesen Daten gewinnen. Dies ist jedoch nützlich um einige Emissions-Modelle einzuschränken oder auszuschliessen.

Die Gliederung dieser Doktorarbeit ist die folgende: Im ersten Kapitel ist eine kurze Einführung über Gammastrahlung und Astrophysik vermittelt: Galaktische und Extragalaktische Quellen der Gammastrahlung und die Wechselwirkungen, in der Gammastrahlung produziert wird, werden präsentiert. In Kapitel 2 werden die experimentellen Methoden der Erkennung der hochenergetischen Gammastrahlung umrissen. Nach einer Einführung zum Thema Luftschauer sind die MAGIC Teleskope und deren Hardware und Software im Detail erklärt. Experimente, die in anderen Energiebereichen beobachten und deren Beobachtungen mit MAGIC kombiniert werden können, werden auch aufgelistet. Kapitel 3 handelt von der Phänomenologie der aktiven Galaxienkerne und Blazare. In Kapitel 4 ist die Analyse der Daten der Quellen 1ES 1727+502, 3C 279 und PKS 1510-089 erläutert. Die MAGIC Beobachtungen sind mit Messungen aus anderen Energiebändern kombiniert. Mögliche Interpretationen des beobachteten Verhaltens werden diskutiert. In Kapitel 5 werden die Ergebnisse, die in Kapitel 4 präsentiert wurden, erläutert und mit historischen Beobachtungen verglichen. Die offenen Fragen und Probleme, die Ziel zukünftiger Studien sein sollen, werden am Schluss hervorgehoben.

In Appenix B werden die Ergebnisse der durch die Neutrino-Trigger erfolgten Beobachtungen des Objekt RBG 0505+612 erläutert. Diese Ergebnisse zeigen, dass das Programm der auf den Neutrino Trigger folgenden Beobachtungen voll funktional ist und dass ein “Multimessenger” Ansatz, bei dem Informationen anhand von verschiedenen kosmischen Teilchen kombiniert werden, benutzt werden konnte, um Aktiven Galaxienkernen zu untersuchen.

Contents

1

Introduction to gamma-ray astrophysics

In 1912 the Austrian physicist Victor Hess measured the ionization of the atmosphere by flying an electroscope on board a balloon. He reached a height of 5 km and found out that the ionization was increasing with altitude: the existence of a penetrating radiation of extraterrestrial origin (later called cosmic radiation or cosmic rays) was discovered. Over the successive century, the study of cosmic rays lead to important discoveries in several fields of physics and promoted the development of different experimental techniques.

In this chapter a brief overview on γ-ray astrophysics will be presented: cosmic-ray properties and experimental techniques used for their detection, γ-ray sources, production and propagation of γ rays are the discussed topics.

1.1 Cosmic rays and gamma rays

Cosmic rays consist mainly of protons and nuclei (protons $\sim 90\%$, helium nuclei $< 10\%$, ionized heavier elements $< 1\%$), with a small fraction of electrons and positrons ($\sim 2\%$) and neutral particles as γ rays, neutrons and neutrinos. Gamma rays are photons with energy larger than 1 MeV and constitute $\sim 0.1\% - 1\%$ of cosmic rays. Gamma rays with energies up to 100 GeV are detected by satellite experiments and are called "high energy" γ rays while those with energies larger than 100 GeV are very high energy (VHE) γ rays and are detected on ground.

The all-particle spectrum of cosmic rays (Fig. 1.1) extends over more than ten orders of magnitude in energy, from tens of MeV to $\sim 10^{20}$ eV. It has a power

law shape $dN/dE \propto E^{-\alpha}$ with constant spectral index $\alpha \sim 2.7$, with a spectral steepening at $E \sim 10^{15.5}$ eV (the *knee*) and a flattening around $E \sim 10^{18.5}$ eV (the *ankle*). It is generally believed that cosmic rays with energies up to 10^{18} eV are of galactic origin, while more energetic cosmic rays are produced by extragalactic sources. The knee could be caused by the fact that galactic accelerators reached their maximum energy, but could also result from propagation and confinement in the Galaxy or change in the cross section with energy. The ankle could be caused by the fact that the extragalactic flux starts to dominate over the galactic one or by e^+e^- pair production resulting from interactions between energetic protons and low energy photons of the cosmic microwave background radiation [54]. A strong flux suppression has been observed at energies $\sim 5 \times 10^{19}$ eV [74, 122], which can result from absorption after interaction with the cosmic microwave background radiation (GZK-cut-off [99, 198])[1], but can also reflect the maximum particle energy at which cosmic rays are accelerated in astrophysical sources [120].

The mass composition of ultra high energy cosmic rays ($> 10^{18}$ eV) is matter of current investigation. The Pierre Auger Observatory and the Telescope Array, two currently operational experiments consisting of ground array of particle detectors and fluorescence telescopes, reported non-consistent results. The former experiment indicates that protons are dominating up to the ankle, while at higher energies heavy mass compositions are favoured. On the other hand, Telescope Array data show that protons dominate at all energies [120]. Another open question is the distribution of arrival directions in the sky of ultra high energy cosmic rays. No significant deviations from an isotropic distribution have been measured yet, despite anisotropies are expected, if current source models are valid, due to deflection in magnetic fields and interaction with background photons fields [120]. Instead at lower energies, at a few TeV, different experiments (MILAGRO, IceCube and Tibet-III air shower array), measured anisotropy at the level of $\sim 10^{-3}$, possibly because of nearby sources [54].

1.2 Detection of cosmic rays

Different techniques are used for the detection of cosmic rays. Two approaches are possible: direct detection with instruments on board satellites and balloons, or indirect detection on ground. In general, instruments for the direct detection have small sizes so that only measurements in the low energy part of the cosmic-ray spectrum are performed. Because of the low flux of high energetic cosmic rays, large instruments (on ground) are used. Cosmic rays interact with atmospheric nuclei and molecules producing air showers in which fluorescence and Cherenkov radiation

[1] Photo-pion production if protons are dominating at these energies or photo-disintegration in case of heavy nuclei.

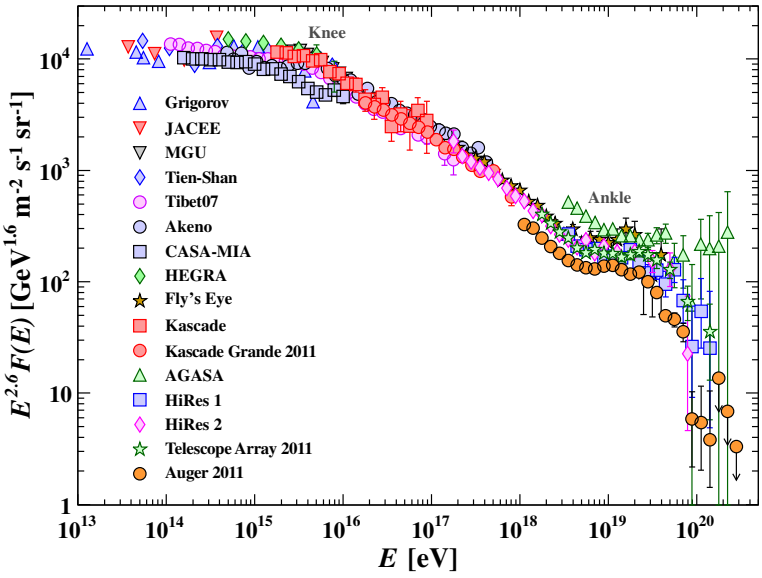

Figure 1.1: The all-particle spectrum of cosmic rays (flux multiplied by $E^{2.6}$) measured by various experiments. The two deviations from a power law function with spectral index $\alpha \sim 2.7$ (knee and ankle) together with the flux suppression at energies $\sim 5 \times 10^{19}$ are visible [54].

are emitted (see Section 2.1.1): current experiments are able to detect one or more of these interaction products and reconstruct the main properties of the cosmic ray incident on top of the atmosphere. The major cosmic ray detectors currently operational can be grouped into the following categories:

- Instruments on ground for indirect detection:
  - surface arrays: scintillation or water Cherenkov detectors. They detect shower particles and can be used for measuring both the hadronic component of cosmic rays and VHE γ rays (Pierre Auger Observatory - energy range: $10^{17} - 10^{21}$ eV, Telescope Array - energy range: $10^{18} - 5 \times 10^{19}$ eV, HAWC - energy range: $10 - 10^{5}$ GeV);
  - air fluorescence telescopes: detect fluorescence radiation with a camera made of photo-multipliers. They are usually combined with surface arrays and are used for studying hadronic cosmic rays (Pierre Auger Observatory, Telescope Array);
  - Cherenkov telescopes: detect Cherenkov radiation emitted by showers initiated by VHE γ rays ($\sim 100 - 10^{4}$ GeV - MAGIC, H.E.S.S., VERITAS).

- Neutrino detectors: due to their small interaction cross-sections, neutrinos penetrate the atmosphere without being attenuated: deep detectors in the sea (ANTARES - from $5 - 15\,\mathrm{GeV}$ to $\sim$PeV energies) and in the ice (IceCube - energy range $100\,\mathrm{GeV} - 10^5\,\mathrm{TeV}$) measuring Cherenkov radiation emitted by charged muons produced in interactions between neutrinos and the detector are used for their detection.

- Instruments on board satellites for direct detection:

  - magnetic spectrometers to detect charged cosmic rays (electrons, positrons, anti-protons and light nuclei at energies from tens of MeV to hundreds of GeV). Their main objective is the study of dark matter nature and the apparent absence of antimatter (PAMELA, AMS);
  - pair-conversion instruments for detection of γ rays with energies $0.1\,\mathrm{GeV} \lesssim E \lesssim 100\,\mathrm{GeV}$ and electrons and positrons (Fermi Gamma-ray Space Telescope).

- Balloon-borne experiments for direct detection: detection of antiparticles and light nuclei using a spectrometer (BESS, energy range 100 MeV-4 GeV for antriprotons), measurement of the spectra of protons, helium and heavier elements up to iron with the ionisation calorimeter technique (ATIC, energy range from 50 GeV to $> 100\,\mathrm{TeV}$).

1.3 Very high energy gamma-ray sources

The VHE γ-ray sky is populated, at the moment, by around 150 sources (Fig. 1.2), among galactic and extragalactic ones.

1.3.1 Galactic sources

Galactic sources are mostly the evolutionary end-products of massive stars. The H.E.S.S. experiment performed a survey of the inner Galaxy detecting around 50 sources [91]. Gamma-ray telescopes located in the Northern hemisphere (MAGIC, VERITAS, Milagro, ARGO-YBJ) observe the outer regions of the galaxy, which are less densely populated but contain unique objects (e.g. Crab).

- **Supernova remnants**: are the left-overs of supernova explosion of massive stars. A shock-wave, expanding and interacting with the surrounding medium, accelerates particles through the Fermi diffusive shock mechanism (see Section 1.4.1). Gamma rays are produced through inverse Compton process (see

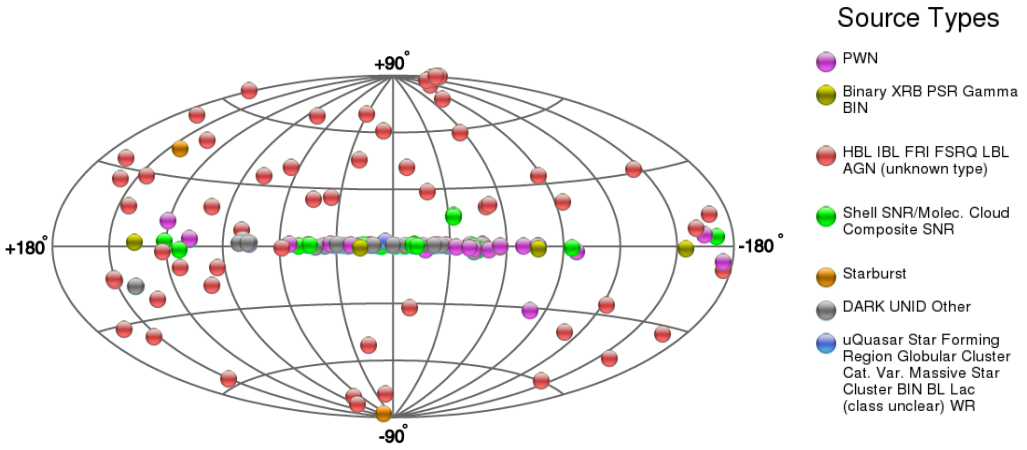

Figure 1.2: The VHE γ ray sky (`http://tevcat.uchicago.edu/`). Sources along the Milky way plane are galactic sources and consist of pulsar wind nebulae (magenta), supernova remnants (green), binary systems (yellow), stellar clusters and star forming regions (blue), and unidentified objects (grey). Extragalactic sources are dominated by AGN (red) with a few starburst galaxies (orange).

Section 1.4.2). Recent observations showed that interactions between energetic protons and ambient gas contribute significantly to γ-ray emission (e.g. RX J1713.7-3946 [20], Tycho's supernova remnant [9], IC 443 [22]).

- **Pulsar wind nebulae or plerions**: are supernova remnants with a pulsar in the central region. The pulsar powers a stellar-wind outflow of electrons and positrons which are accelerated and emit strong synchrotron and inverse Compton radiation (see Section 1.4.2). Young pulsar wind nebulae have point-like extension with the pulsar located in their core, while old pulsar wind nebulae ($> 10^4$ years) are extended objects in which the pulsar does not coincide any more with the centre of the TeV emission (the nebula can be distorted by the reverse shock). At the moment pulsar wind nebulae are the most numerous class of VHE γ-ray galactic sources (about 30 objects).

- **Crab Nebula and pulsar**: it is a pulsar wind nebula and was the first TeV source to be discovered [191]. The Crab Nebula is one of the most observed sources in γ rays and because of its constant flux[1] is the standard candle for VHE astronomy. The Crab Nebula is the remnant of a supernova explosion whose light reached Earth in 1054 AD. It is located at a distance of 2 kpc in

[1]Recently pronounced short-term variability has been reported at γ rays with $E < 1$ GeV [63, 178] but no flux variations have been reported so far at VHE.

the Taurus constellation and is formed by expanding gas clouds and a pulsar in the central region, which is the most energetic pulsar in the Galaxy. The non-thermal emission of the Crab nebula has two components: synchrotron emission extending up to 100 MeV and inverse Compton above 1 GeV (see Section 1.4.2). The pulsed emission has been recently detected at VHE [30, 40, 44, 190].

- **Binary systems**: consist of a compact object (neutron star or black hole) interacting with a companion star (e.g. LSI+61 303 [28]). The compact object accretes material from the star, in some cases relativistic jet are observed (microquasar). The emission from these sources is variable.

- **Stellar clusters**: in star-forming regions, strong stellar winds collide and form termination shocks in which particles are accelerated. These regions contain supernova remnants, neutron stars and binary systems and it is not clear which are the processes responsible for the γ ray emission (Westerlund 1 and 2 [8, 15]);

- **Galactic centre**: called the SgrA complex, is the rotational centre of the Galaxy. It is a bright TeV source with two components: a central, steady and point-like source and a diffuse fainter component extending towards the Galactic plane. This region has been observed at lower energies[1]. Radio observations show that SgrA consists of three different components: a central black hole (SgrA*), clouds of dust and gas orbiting around the black hole and a supernova remnant (SgrA east). The brightest TeV source is located close to the black hole, while the diffuse component is spatially correlated with the molecular clouds and the TeV emission could be caused by the decay of light mesons produced in the interactions between hadronic cosmic rays and clouds (see Section 1.4.2). A firm counterpart for the source of TeV emission has not been identified yet [162].

- **Unidentified sources**: many sources detected with the galactic-plane scan have no counterparts at lower energies. Their absence could result from insufficient exposure with instruments in the radio and X-ray bands but also could hide new types of sources (no synchrotron emission in X-ray and radio bands is possible in proton accelerators or sources with small magnetic fields). Some of the unidentified sources have been recently identified with known objects as pulsars and supernova remnants (e.g.. HESS J1813-178 [61], HESS J1857+026 [110]).

[1] optical and UV observations are not feasible due to visual extinction.

- **Diffuse galactic emission**: a diffuse component of γ rays with $E > 100\,\mathrm{GeV}$ has been detected by the H.E.S.S. experiment [85]. It is believed to be originated by the decay of light mesons resulting from interactions between cosmic rays, molecular clouds and dust of the galactic plane (see Section 1.4.2).

1.3.2 Extragalactic sources

Extragalactic sources are mainly active galactic nuclei, especially blazars. The detection of distant sources is limited to objects located in the nearby universe (redshift $z \lesssim 0.6$)[1], due to the absorption of VHE γ rays by low energy photons of the extragalactic background light (see Section 1.4.3).

- **Active galactic nuclei (AGN)**: are galaxies with very bright nuclei, powered by the release of stellar material falling into a black hole. AGN are the topic of this work and a review on these objects is given in Chapter 3.

- **Starburst galaxies**: are galaxies with a high star formation rate, often triggered by the interaction with another galaxy. The explosion rate of supernova is very high in these regions, so high densities of cosmic rays are expected. Also the density of ambient gas is high, so these sources are expected to emit γ rays through hadronic interactions (proton-proton collisions). Currently only two starburst galaxies are known to emit very high energy γ rays: M 82 [189] and the spiral galaxy NGC 253 [11].

1.4 Production and propagation of gamma rays

Very high energy γ rays are produced by the interaction of relativistic charged particles (like electrons and protons) with magnetic fields, low energy photons and matter.

1.4.1 Acceleration of electrons and protons

Various acceleration mechanisms are taking place in different types of astrophysical sources. Among them, the Fermi diffusive shock acceleration is the most commonly accepted because it predicts naturally a distribution of non thermal particles with spectral index ~ 2, matching observations, and because shocks are widely present in the universe. In AGN jets shocks are formed when the outflow encounters ambient material in the host galaxy or in the intergalactic medium.

[1] During the writing of this thesis a gravitationally lensed blazar, S3 0218+357, located at the redshift of $z = 0.9$ has been discovered by the MAGIC telescopes [144].

Fermi acceleration theory, now called Fermi second order acceleration, was proposed in 1949 to explain the acceleration of cosmic rays in the interstellar space: charged cosmic rays interact with magnetised clouds and gain energy stochastically [86]. The most remarkable result of this theory is that the spectrum of accelerated particles is a power law function. On the other hand, since the energy gain per interaction is very small, this process is not efficient enough to explain acceleration of particles in short time scales. In the following years this theory was modified by several authors into a scenario in which charged particles are accelerated by shocks (diffusive shock acceleration or Fermi first order acceleration - for reviews see [77, 127, 159]).

Other acceleration mechanisms are for example magnetic reconnection occurring in the sun corona and eventually in AGN (for a review [199]), and electrodynamic acceleration processes taking place in neutron stars, pulsars and magnetars [47].

1.4.2 Radiative processes

In ambients in which energetic charged particles, low energy photons and magnetic field are present, the following interactions are expected: synchrotron radiation emitted by charged particles, Compton scattering, $\gamma\gamma$ pair production, and if also protons are accelerated to high energies, photo-meson production. In ambients with high density of matter (like supernova remnants) bremsstrahlung, proton-proton collisions, Bethe-Heitler pair production (electron-positron pair production by a nucleus on ambient photons) and photo-disintegration (the emission of a subatomic particle, like proton, neutron or alpha particle, by an atom after the interaction with an energetic γ ray) occur. In the following only the processes most likely to occur in sources with low particle densities, like in AGN, will be briefly summarised. Only most important features and relations required for the understanding of the work presented in the successive chapters are recalled. This discussion is based on [58, 92]; for a more detailed discussion and formula derivations see [77, 164].

Synchrotron radiation

A charged particle moving through a region with magnetic field follows a spiral trajectory along the magnetic field lines and emit synchrotron radiation. Non-relativistic particles emit cyclotron radiation, while relativistic particles emit synchrotron radiation over a broad range of frequencies. We will restrict ourself to relativistic particles, the common case in astrophysics. The energy loss rate for a charged particle with mass m, electric charge q, Lorentz factor γ and velocity βc is

$$\left(\frac{d\gamma}{dt}\right)_{syn} = -\frac{4}{3} c\sigma_T \frac{u_B}{m_e c^2} Z^4 \left(\frac{m_e}{m}\right)^3 \beta^2\gamma^2 \tag{1.1}$$

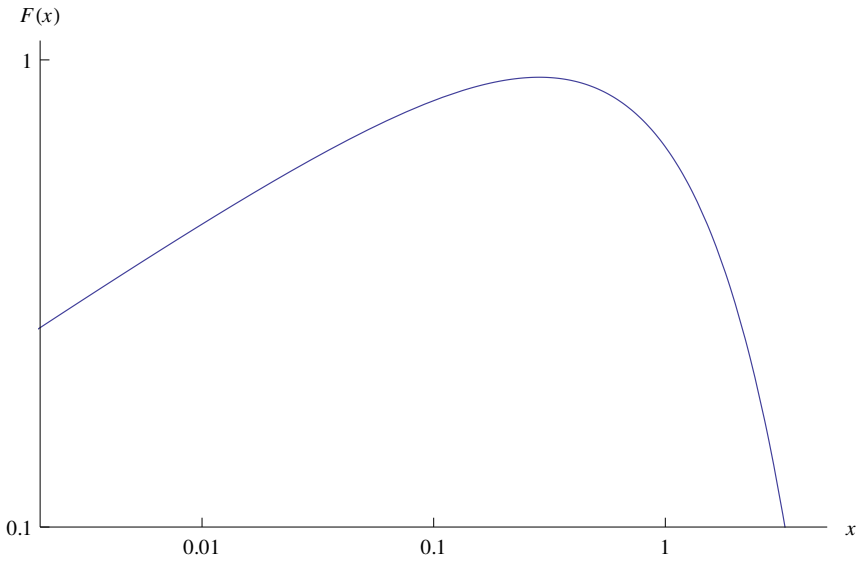

Figure 1.3: The synchrotron spectrum emitted by a single electron defined in Eq. 1.3 plotted as a function of the variable $x = \nu/\nu_c$.

where σ_T is Thomson cross-section, m_e the electron mass, $u_B = B^2/8\pi$ the energy density in the magnetic field B and Z the particle charge in units of the elementary charge e. Since the energy loss rate is proportional to m^{-3}, lighter particles radiate more efficiently than massive ones, therefore fast radiative losses compete, eventually prevent, acceleration to high energies. On the other hand, heavier particles like protons can be accelerated easily but they need to reach extreme energies to produce radiative output.

The power per unit frequency emitted by an electron with given pitch angle ϑ (angle between the particle velocity vector and the magnetic field line) is

$$P_s(\nu, \gamma, \vartheta) = \frac{\sqrt{3} e^3 B \sin\vartheta}{m_e c^2} F\left(\frac{\nu}{\nu_c}\right) \tag{1.2}$$

$$F\left(\frac{\nu}{\nu_c}\right) = \frac{\nu}{\nu_c} \int_{\nu/\nu_c}^{\infty} K_{5/3}(y) dy \tag{1.3}$$

$$\nu_c = \frac{3}{2}\nu_s \sin\vartheta, \qquad \nu_s = \gamma^2 \nu_L, \qquad \nu_L = \frac{eB}{2\pi m_e c} \tag{1.4}$$

where $K_{5/3}(y)$ is the modified Bessel function of order 5/3, ν_c is the critical frequency, ν_s and ν_L are the typical frequencies at which the particle emits most of its power, respectively in the relativistic and non-relativistic case. The function $F(\nu/\nu_c)$ has a

peak at $\nu \sim 0.29\nu_c$ and its asymptotic behaviour is

$$F\left(\frac{\nu}{\nu_c}\right) \xrightarrow{\nu \ll \nu_c} \frac{4\pi}{\sqrt{3}\Gamma(1/3)} \left(\frac{\nu}{2\nu_c}\right)^{1/3} \tag{1.5}$$

$$F\left(\frac{\nu}{\nu_c}\right) \xrightarrow{\nu \gg \nu_c} \left(\frac{\pi}{2}\right)^2 \left(\frac{\nu}{\nu_c}\right)^{1/2} e^{-\nu/\nu_c} \tag{1.6}$$

as shown in Fig. 1.3. The emission from a population of electrons whose distribution is a power law

$$n(\gamma) = k\gamma^{-p} \qquad \text{for } \gamma_{min} < \gamma < \gamma_{max} \tag{1.7}$$

assuming the pitch angle distribution is the same for low and high γ, is

$$j_s(\nu, \vartheta) = \frac{1}{4\pi} \int_{\gamma_{min}}^{\gamma_{max}} n(\gamma) P_s(\nu, \gamma, \vartheta) d\gamma \tag{1.8}$$

$$\propto k B^{(p+1)/2} \nu^{-(p-1)/2} \tag{1.9}$$

hence $j_s \propto \nu^{-\alpha}$. The emitted photons have a power law distribution whose spectral index is related with the spectral index of the electrons by $\alpha = (p-1)/2$.

In this process, photons can be absorbed by relativistic electrons in the magnetic field (**synchrotron self-absorption**). The absorption coefficient is proportional to $\nu^{-(p+4)/2} B^{(p+2)/2}$, so the opacity increases with decreasing frequencies. The resulting spectrum depends on the self-absorption frequency ν_{SSA}, defined by $\tau_{SSA} = R\nu_{SSA} = 1$. If it is larger than the critical frequency of the lowest energy electron $\nu_{SSA} > \nu_c(\gamma_1)$, the spectrum is $S_\nu \propto \nu^{5/2}$, otherwise ($\nu_{SSA} < \nu_c(\gamma_1)$) it will be $S_\nu \propto \nu^2$. The overall synchrotron spectrum, including the effects of self-absorption, is shown in Fig. 1.4.

A property of synchrotron radiation is its high degree of polarisation. Synchrotron radiation emitted by a relativistic particle is beamed in the direction of motion into a cone, being thus elliptically polarised. In a distribution of particles with different pitch angles, the elliptical polarisation averages out and the overall emission is partially linearly polarised [164].

Compton scattering

Compton interaction is the scattering between an electron and a photon. Consider an electron with energy γ and a photon with energy $\varepsilon = (h\nu)/(m_e c^2)$; the total cross-section, integrated over all scattered photons energies ε'_s and directions, of the Compton scattering is

$$\sigma_C(\varepsilon') = \frac{\pi r_e^2}{\varepsilon'^2} \left[4 + \frac{2\varepsilon'^2(1+\varepsilon')}{(1+2\varepsilon')^2} + \frac{\varepsilon'^2 - 2\varepsilon' - 2}{\varepsilon'} \ln(1+2\varepsilon')\right] \tag{1.10}$$

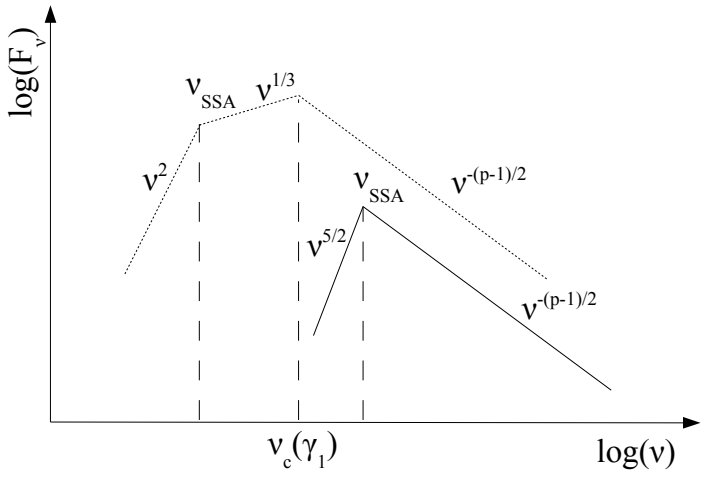

Figure 1.4: The synchrotron spectrum emitted by a population of relativistic electrons whose distribution is a power law function with index p. For frequencies larger than the synchrotron self-absorption frequency ν_{SSA} the emitted spectrum is described by a power law function with index $-(p-1)/2$. For frequencies $\nu < \nu_{SSA}$ two different cases are possible depending on wether $\nu_{SSA} < \nu_c(\gamma_1)$ (dotted line) or $\nu_{SSA} > \nu_c(\gamma_1)$ (solid line).

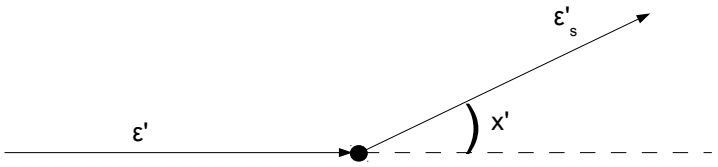

Figure 1.5: The Compton scattering in the electron rest frame.

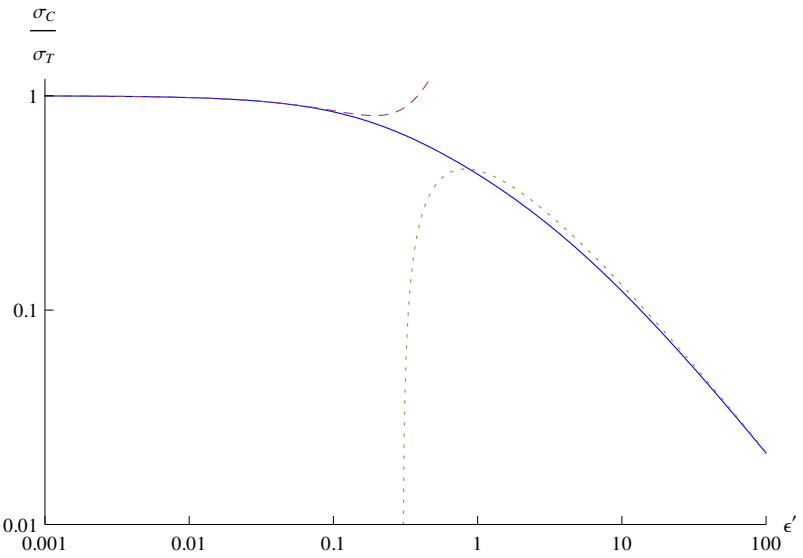

Figure 1.6: The cross-section of Compton scattering (blue full line). The ratio σ_C/σ_T is shown as a function of the photon energy ε' in electron rest frame. The asymptotes for $\varepsilon' \ll 1$ (Thomson regime, violet dashed line) and $\varepsilon' \gg 1$ (Klein-Nishina regime, yellow dotted line) are also shown.

where ε' is the energy of the photon in the rest frame of the electron before scattering and r_e the classical electron radius (Fig. 1.5). For energies $\varepsilon' \ll 1$ (Thomson regime) the cross-section is constant $\sigma_C \sim \sigma_T$. For large values of ε there is a substantial transfer of energy from the photon to the electron but the cross-section is reduced. The case $\varepsilon' \gg 1$ is called Klein-Nishina limit. To sum up, the cross-section of the Compton process has the following asymptotic behaviours

$$\sigma_C(\varepsilon') \approx \begin{cases} \sigma_T(1 - 2\varepsilon' + \frac{26}{5}\varepsilon'^2) & \text{for } \varepsilon' \ll 1 \\ \frac{3}{8}\frac{\sigma_T}{\varepsilon'}\left[\ln(2\varepsilon') + \frac{1}{2}\right] & \text{for } \varepsilon' \gg 1 \end{cases} \tag{1.11}$$

and it is shown in Fig. 1.6.

In the case of scattering between a relativistic electron with energy γ and normalised velocity β and a photon field it is convenient to adopt as laboratory frame (unprimed) the rest frame of the emission region. The energies of the photon before ε and after ε_s the scattering, in the two reference frames are related by

$$\varepsilon' = \varepsilon\gamma(1 - \beta\mu), \qquad \varepsilon_s = \varepsilon'_s\gamma(1 + \beta\mu'_s) \tag{1.12}$$

where $\mu = \cos\vartheta$, $\mu'_s = \cos\vartheta'_s$ are related to the angles between the electron velocity vector and the photon direction before the scattering in the laboratory frame (ϑ)

and after the scattering in the electron rest frame (ϑ'_s). In Thomson regime, the scattering is elastic in the electron rest frame $\varepsilon'_s \sim \varepsilon'$, but in the laboratory frame its energy after the scattering is $\varepsilon'_s \approx \gamma\varepsilon$. In case of a scattering between a relativistic electron and a low energy photon, energy is transferred to the photon (inverse Compton scattering).

The energy-loss rate for an electron of energy γ travelling at an angle $\psi_e \cos^{-1}\eta_e$ with respect to the z-axis scattering on a radiation field with photons isotropically distributed $n_{ph}(\varepsilon)$, in the Thomson limit and with $\beta \to 1$ is

$$\left(\frac{d\gamma}{dt}\right)_C \approx -\frac{4}{3} c\sigma_T \frac{u_{ph}}{m_e c^2}\gamma^2 \tag{1.13}$$

which is analogous to the synchrotron energy-loss, replacing u_{ph} with u_B implying the following relations

$$\frac{L_{Thomson}}{L_{sy}} = \frac{\dot{\gamma}_{Thomson}}{\dot{\gamma}_{sy}} = \frac{u_{ph}}{u_B} \tag{1.14}$$

where L indicates the total luminosity produced through inverse Compton in the Thomson limit ($L_{Thomson}$) and synchrotron processes (L_{sy}). For large electron and photon energies ($\gamma\varepsilon \gtrsim 1$), the Klein-Nishina suppression of the cross-section causes a reduction of the energy-loss rate, which is $-\dot{\gamma} \propto \ln\gamma$ [56].

The Compton radiation spectrum produced by a population of electrons $n_e(\gamma, \Omega_e)$ scattering on photons $n_{ph}(\Omega_{ph})$ with angles $\Omega_e(\psi_e, \phi_e)$ and $\Omega_{ph}(\psi_{ph}, \phi_{ph})$, at the frequency $\nu = e_s m_e c^2/h$ in the direction $\Omega_s(\psi_s, \phi_s)$ is

$$j_\nu(\varepsilon_s, \Omega_s) = hc\varepsilon_s \int_{4\pi} d\Omega_e \int_1^\infty d\gamma n_e(\gamma, \Omega_e) \times \int_{4\pi} d\Omega_{ph} \int_0^\infty d\varepsilon n_{ph}(\varepsilon, \Omega_{ph})(1-\beta\mu)\frac{d\sigma_C}{d\varepsilon_s d\Omega_s} \tag{1.15}$$

where the angles are

$$\mu'_s = \frac{\mu_s - \beta}{1-\beta\mu_s}, \qquad \mu' = \frac{\mu - \beta}{1-\beta\mu} \tag{1.16}$$

and $d\sigma_C/d\varepsilon_s d\Omega_s$ is the differential Klein-Nishina cross-section. In the general case, for arbitrary distributions of electrons and photons, the solution of Eq. 1.15 is very difficult. This can be simplified using approximated formula for the cross-section. In addition, for applications to astrophysical environments, and particular AGN, it is safe to assume an azimuthal symmetry and that electrons and photons are isotropically distributed in the rest frame of the emission region. Restricting ourselves to the Thomson regime, using the δ approximation for the cross-section, the emissivity for monoenergetic photons $n_{ph}(\varepsilon) = n_{ph,0}\delta(\varepsilon - \varepsilon_0)$ and a power-law distribution with

index p of electrons is

$$j_\nu = \frac{hc\sigma_T n_0 n_{ph,0}}{8\pi(p+3)} \left(\frac{\varepsilon_s}{\varepsilon_0}\right)^2 \left[\left(\max\left[\gamma_1, \varepsilon_s, \sqrt{\frac{\varepsilon_s}{2\varepsilon_0}}\right]\right)^{-(p+3)} - \gamma_2^{-(p+3)}\right] \times H\left(\gamma_2 - \max\left[\varepsilon_s, \sqrt{\frac{\varepsilon_s}{2\varepsilon_0}}\right]\right) \quad (1.17)$$

where $H(x)$ is the Heaveside function defined $H(x) = 1$ if $x \geq 0$ and $H(x) = 0$ elsewhere. It is worth to note that in the energy range $\varepsilon_s > 2\varepsilon_0\gamma_1^2$ and $\varepsilon_s < 1/(2\varepsilon_0)$ (when the last term in the "max" function dominates), the emission has a power law spectrum with index

$$\alpha_C = \frac{p-1}{2} \quad (1.18)$$

which is the same spectral shape found for synchrotron emission.

Photo-meson production

Relativistic protons interact with low energy photons through photo-meson production $p\gamma \to N\pi$, charged pions decay into leptons and neutrinos and neutral pions into γ rays. This process takes place if the energy of the photon in proton rest frame is larger than the threshold energy

$$\sqrt{s_{thr}} = m_\pi c^2 \left(1 + \frac{m_\pi}{2m_p}\right) \quad (1.19)$$

where m_p and m_π are the mass of the proton and pion ($m_{\pi^0} = 135.0\,\mathrm{MeV}$, $m_{\pi^\pm} = 139.6\,\mathrm{MeV}$), respectively.

The cross-section for hadronic photo-meson production depends on the invariant energy of the interaction and up to $\sqrt{s}$ of a few GeV is given by collider experiments, but for the energies reached in astrophysical environments ($\sqrt{s} \sim 10^3\,\mathrm{GeV}$) there are no measurements available and Monte Carlo methods are used (e.g. the SOPHIA software is a Monte Carlo generator which computes the total cross-section of this process and it has been used in the contest of modelling the emission of AGN [149]). The following processes contribute to the total photo-meson cross-section (Fig. 1.7):

- resonance production: the most important one is the $\Delta^+(1232)$ resonance;
- direct pion production:

$$p\gamma \to n\pi^+, \qquad p\gamma \to \Delta^{++}\pi^-, \qquad p\gamma \to \Delta^0\pi^+$$

- diffractive scattering: coupling of photons to vector mesons ρ^0 and w which are produced at energies $\sqrt{s} \geq 2\,\mathrm{GeV}$;

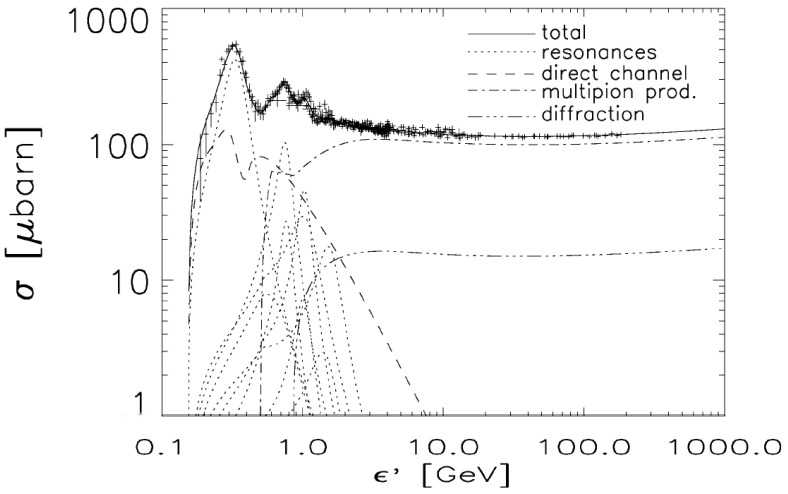

Figure 1.7: The total cross-section of photo-meson production together with the partial cross-sections [149].

- multi-pion production.

The dominant type of mesons produced in photohadronic interactions are pions: neutral pions decay to two photons $\pi^0 \to 2\gamma$ with half-life time $t_{1/2} \approx 8.4 \times 10^{-17}$ s and charged pions into muons and neutrinos $\pi^{\pm} \to \mu^{\pm} + \nu_{\mu}(\bar{\nu_{\mu}})$ with $t_{1/2} \approx 2.6 \times 10^{-8}$ s, and muons in turn decay into $\mu^{\pm} \to e^{\pm} + \nu_e(\bar{\nu_e}) + \nu_{\mu}(\bar{\nu_{\mu}})$. Kaons and η mesons are also produced $(10 - 20\%)$ contributing to the overall photon, lepton and neutrino production.

In highly magnetised environments, the time scale for synchrotron loss can become shorter than the decay time scale. Synchrotron radiation emitted by charged pions and muons affects the total flux of both γ rays and neutrinos.

Bethe-Heitler pair production

Nuclei interact with low energy photons producing an electron-positron pair $p+\gamma \to p' + e^+ + e^-$ if the condition on the energy threshold is fulfilled

$$s = m_p^2 c^4 + 2E_{photon}E_p(1 - \beta_p \cos\vartheta) \geq s_{thr} = (m_p c^2 + 2m_e c^2)^2 \tag{1.20}$$

where $\beta_p c$ is the proton velocity, m_p its mass, E_{photon} and $E_p = \gamma_p m_p c^2$ are respectively the photon and proton energy, γ_p the proton Lorentz factor, ϑ the interaction angle and m_e is the mass of the electron. The cross-section averaged over the angle

is

$$\langle \sigma_{BH}(\gamma_p, x) \rangle = \frac{1}{2} \int_{-1}^{\cos\vartheta_{thr}} (1 - \beta_p \cos\vartheta) \sigma_{BH}(s) d\cos\vartheta \tag{1.21}$$

$$= \frac{1}{8\beta_p E_p^2 E_{photon}^2} \int_{s_{thr}}^{s_{max}} \sigma_{BH}(s)(s - m_p^2 c^4) ds \tag{1.22}$$

with $s_{max} = m_p^2 c^4 + 2E_p E_{photon}(1 + \beta_p)$ (head-on collisions). Bethe-Heitler pair production is less efficient than hadronic interactions if the target photon field is a power law with index < 2 [132, 171].

Photon-photon pair production

Energetic photons interact with low energy photons producing electron-positron pairs $\gamma\gamma \rightarrow e^+e^-$. The energy threshold of this process, in the centre of mass frame assuming a head-on collision, is

$$\varepsilon_{1,thr} = \frac{1}{\varepsilon_2} \tag{1.23}$$

where $\varepsilon_1, \varepsilon_2$ are the energies of the photons. The cross section of this process is [108]

$$\sigma_{\gamma\gamma}(\beta) = \frac{3}{16}\sigma_T(1 - \beta^2)\left[2\beta(\beta^2 - 2) + (3 - \beta^4)\ln\left(\frac{1+\beta}{1-\beta}\right)\right] \tag{1.24}$$

where

$$\beta = \sqrt{1 - \frac{2}{\varepsilon_1 \varepsilon_2 (1 - \mu)}} \tag{1.25}$$

with $\mu = \cos\vartheta$, ϑ the collision angle and σ_T the Thomson cross-section. The cross-section has a maximum $\sigma_{\gamma\gamma} \approx \sigma_T/4$ at photon energies $\varepsilon = 2\varepsilon_{thr}$.

Pair-production occurs in interactions with photon fields both inside and outside the emission region. In the first case, the overall effect of absorption has to be evaluated solving the radiative transfer equation. In case of absorption outside the emission region the intrinsic flux emitted F_{em} is then attenuated by a factor $e^{-\tau_{\gamma\gamma}}$

$$F_{obs}(\varepsilon_\gamma) = F_{em}(\varepsilon_\gamma) e^{-\tau_{\gamma\gamma}} \tag{1.26}$$

defining $\tau_{\gamma\gamma}(\varepsilon_\gamma, z)$ the optical depth. This condition is usually met in AGN when the emission is generated in a region close to the core and the emitted radiation interacts with external fields of low energy photons, like the broad line region and the torus (see Chapter 3), and in the intergalactic space, where γ rays interact with background photons (see Section 1.4.3).

1.4.3 Propagation through the universe

Background radiation and magnetic field of the intergalactic and interstellar space affect the propagation of γ rays: photons are absorbed via pair production and the cascades resulting from these interactions are deflected by extragalactic magnetic fields.

The radiation fields in the universe are the cosmic microwave radiation in the mm band, a left over of the big bang which corresponds to the thermal emission of a black body with temperature $2.7\,K$, and the extragalactic background light (EBL) which is composed by starlight (UV and optical band) and the starlight absorbed and re-emitted by dust (infra-red energy range). Cosmic microwave radiation will absorb γ rays with PeV energies, while the EBL will interact with GeV (UV and optical starlight) and TeV γ rays (infra-red emission of dust), as shown by Eq. 1.23. This effect was predicted to be relevant for γ-ray emission [175]. According to Eq. 1.26, the flux emitted by a γ-ray source F_{em} is attenuated by a factor $e^{-\tau_{\gamma\gamma}}$, where the optical depth depends on the energy of the γ ray ε_γ and the distance of the source (expressed in terms of the redshift z):

$$\tau_{\gamma\gamma}(\varepsilon_\gamma, z) = c \int_0^z dz \frac{dt}{dz} \int_0^2 dx \frac{x}{2} \int_{\frac{2m_e^2c^4}{\varepsilon_\gamma \varepsilon_{bkg} x(1+z)}}^{\infty} d\varepsilon_{bkg} \frac{dn_\gamma(\varepsilon_{bkg}, z')}{d\varepsilon_{bkg}} \sigma_{\gamma\gamma}(\beta) \qquad (1.27)$$

with $\sigma_{\gamma\gamma}(\beta)$ computed from Eq. 1.24 using $s = 2\varepsilon_\gamma \varepsilon_{bkg} x(1+z)$ and ε_{bkg} being the energy of the background photon. The term dt/dz depends on the geometry of the universe and $n_\gamma(\varepsilon_{bkg}, z')$ is the photon number density. The calculation of this latter term is a complicated task because it has to account for the light emitted by resolved and unresolved extragalactic sources and its absorption by dust during the whole life of the universe. Direct observations are affected by the strong emission of the Galaxy and the density level of EBL is not known [105, 106]. Lower limits are obtained with galaxy counts in the UV, optical and infra-red bands [84]. Different approaches can be adopted for calculating the luminosity density of the EBL as a function of the redshift and wavelenght, resulting in various models for the EBL intensity and spectral distribution (see for a review [84]); the models used in this work are [81, 89]. The EBL absorption limits the distance and the energy accessible: for instance, from a source located at the redshift $z = 0.5$, only measurements up to a few hundred GeV are possible (see Fig. 1.8).

Recently, observations in the γ-ray band, both with Cherenkov telescopes and with the *Fermi*-LAT instrument, have been used to set upper limits on the EBL in the near and mid infra-red and in the UV-optical bands respectively [12, 14, 29, 141–143, 154].

The effects of the EBL absorption can be used also to derive constraints on the extragalactic magnetic field B_{EG}. The e^+e^- pairs will start an electromagnetic

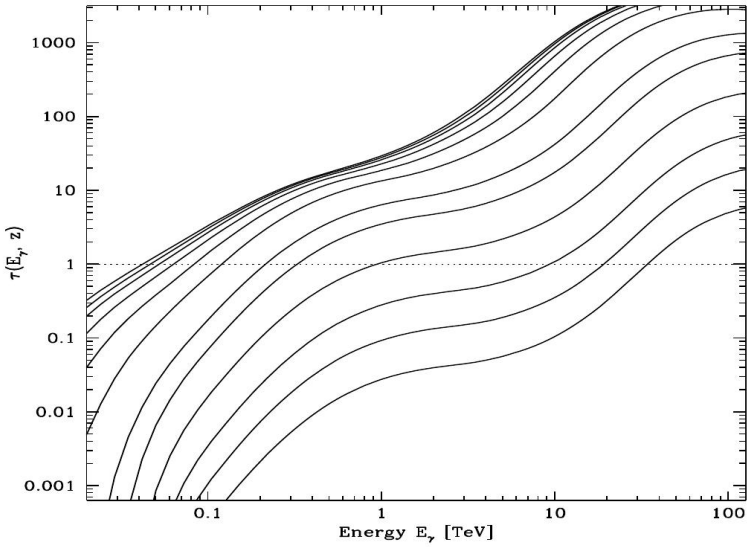

Figure 1.8: The $\gamma\gamma$ opacity due to pair production between γ rays and the EBL according to the model of [89]. The optical depth $\tau_{\gamma\gamma}$ is given as a function of the γ ray energy ε_γ and for different redshifts: $z = 0.003, 0.001, 0.03, 0.1, 0.3, 0.5, 1, 1.5, 2, 2.5, 3, 4$, from bottom to top.

cascade producing secondary γ rays of GeV energies. The e^+e^- of the cascade are deflected by the magnetic field, affecting the spectral shape of the source measured at Earth. From this argument, the limit $B_{EG} \gtrsim 10^{-17}$ G has been derived [182].

2

Observation techniques: the MAGIC telescopes

The γ-ray fluxes in the VHE range are low, strong sources emit only few photons above 1 TeV per m^2-year [112], so direct detection with experiments on board satellites is not feasible. The Earth atmosphere is opaque to high energy radiation (Fig. 2.1), leaving indirect techniques the only possibility for detecting VHE γ rays on ground. Imaging atmospheric Cherenkov telescopes detect Cherenkov light emitted by ultra-relativistic particles generated in the interaction between VHE γ rays and atmospheric nuclei. In this chapter, the phenomena of air showers and emission of Cherenkov radiation will be briefly summarised. After a general introduction to the technique of imaging atmospheric Cherenkov telescopes, the focus will be set to MAGIC telescopes: hardware components and the standard analysis chain will be explained, and in the final section the performance of the system will be presented.

2.1 Gamma-ray propagation in the atmosphere

2.1.1 Extensive air showers

Cosmic rays and γ rays interact with the molecules present in the upper part of the atmosphere, causing a particle cascade, called extensive air shower. Since primary particles of different nature undergo different energy-loss processes and interactions, the shower development is deeply influenced by the particle type (Fig. 2.2).

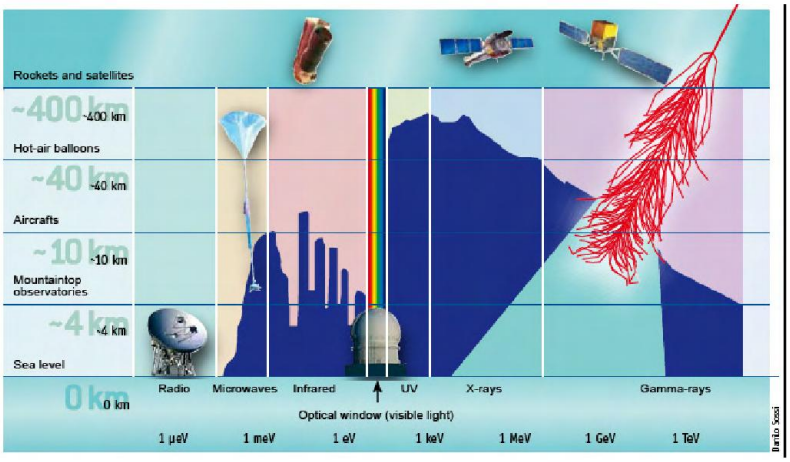

Figure 2.1: The transparency of the atmosphere as function of the energy [75]. The atmosphere is transparent only to radio and optical wavebands and direct detection in other energy ranges is possible with balloon flights and satellites. Gamma rays interact with atmosphere molecules producing air showers at altitudes $\sim 10\,\mathrm{km}$ above the see level, which can be detected with ground-based observatories located at height, on top of mountains.

Electromagnetic showers

High energy photons and electrons lose energy in matter mainly through pair production and bremsstrahlung processes, whose radiation lengths ξ_0[1] are the same in the ultra-relativistic limit. When a photon of energy E_0 enters the atmosphere, it scatters off an atmospheric molecule. After a distance $R = \xi_0 \ln 2$, it creates an electron-positron pair and after a distance R the two particles, each with mean energy $E_0/2$, radiate via bremsstrahlung two photons of energy $E_0/4$ each. After a distance nR there are 2^n secondary particles with mean energy $E = E_0/2^n$ (Fig. 2.2a, [127]). The shower continues to develop as long as $E > E_c$, where E_c is the critical energy which in air is $E_c \sim 80\,\mathrm{MeV}$. Afterwards, the dominant energy loss-process for electrons becomes ionization and for photons the cross-section of pair-production is of the same order of Compton scattering and photoelectric absorption cross-sections.

[1]The radiation length is the mean distance over which the particle energy is reduced by a factor e for electrons and 7/9 of the mean free path for photons.

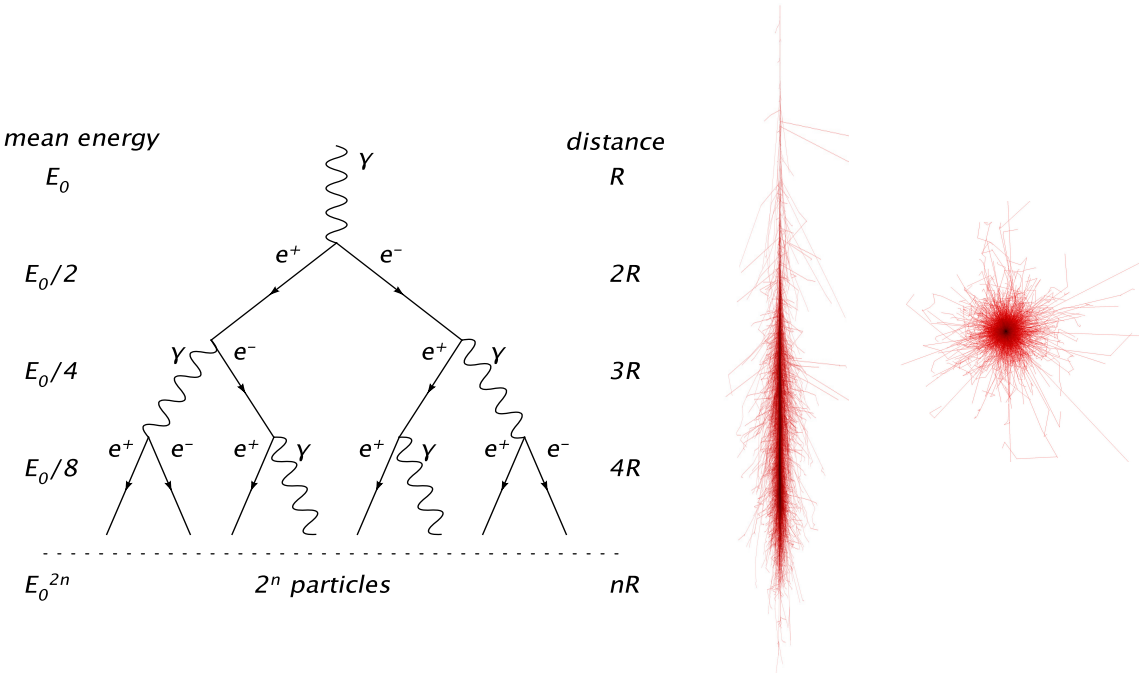

(a) Electromagnetic air shower;

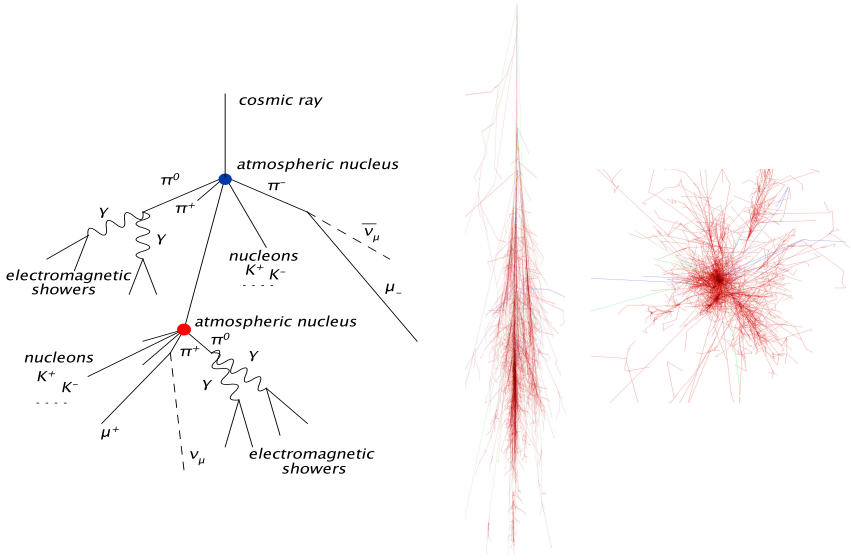

(b) hadronic air shower.

Figure 2.2: Extensive air showers: a sketch showing the cascade development and CORSIKA images of a shower generated by (a) 100 GeV photon (b) 100 GeV proton (F. Schmidt, `http://www.ast.leeds.ac.uk/~fs/showerimages.html`). In electromagnetic air showers two processes with comparable cross-section are taking place, while in hadronic showers several interactions are possible resulting in showers with larger fluctuations and a more irregular shape.

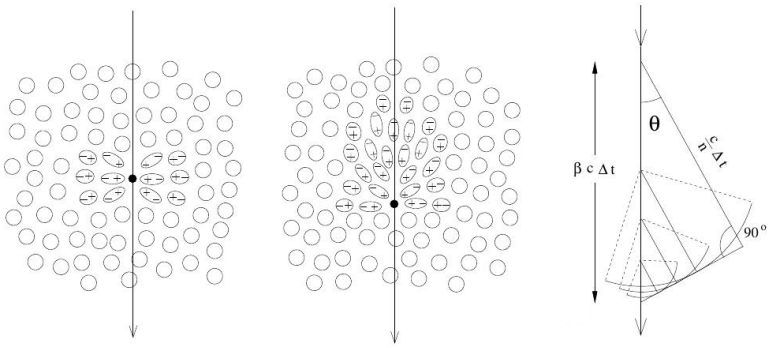

Figure 2.3: A sketch illustrating the polarisation induced by a charged particle in a dielectric medium moving with velocity $v \ll c$ (left) and with $v = \beta c > c/n$ (middle). In the right panel the geometrical description of the Cherenkov cone is shown [158].

Hadronic showers

Protons and atomic nuclei initiate hadronic showers (Fig. 2.2b), in which pions, kaons and heavier particles are produced. Neutral pions decay into two high energetic photons, which in turn initiate electromagnetic showers. Charged pions decay into muons and neutrinos (and anti-neutrinos), and kaons follow the same channel in 21.1% of the cases, while in the other 63.4% cases they produce pions: $k^{\pm} \rightarrow \pi^{\pm} + \pi^0$. Secondary protons lose energy primarily through ionization, and in case of energies $< 1\,\mathrm{GeV}$ they are stopped. Muons produced in the shower do not initiate showers and their only energy-loss process is ionization, however, many are produced with very high energies so their ionization losses are small, and a large number of muons reach Earth's surface.

Because of the numerous interaction channels and the large radiation length of air for protons ($\xi_0 \sim 70\,\mathrm{g\,cm^{-2}}$), hadronic showers have a wider lateral profile and larger shower-to-shower fluctuations than electromagnetic showers. In addition, hadronic showers contain invisible particles (neutrinos) and originate subshowers. Simulations of showers generated by 100 GeV photons and a 100 GeV protons are shown in Fig. 2.2. As explained later, the differences in the shower structure are at the basis of the background suppression techniques used in the analysis of data from imaging atmospheric telescopes.

2.1.2 Cherenkov radiation

A charged particle moving in a medium with velocity v larger than the velocity of light in that medium emits Cherenkov radiation [68, 188]. Since electron-positron

pairs generated in air showers can easily reach ultra-relativistic speeds, Cherenkov radiation is emitted in air showers by electron-positron pairs.

Emission of Cherenkov radiation is caused by transitions of atmospheric molecules between different polarisation states (Fig. 2.3): the passage of a charged particle induces polarisation and when the polarised molecules return to their initial state, they emit incoherent dipole radiation. If $v = \beta c > c/n$, where n is the refraction index of the medium, this radiation is coherent and is emitted in a narrow cone, with emission angle $\cos\vartheta = 1/(\beta n)$. The condition for Cherenkov radiation is $\beta_{min} = 1/n$, which in terms of energy is

$$E_{thr} = \frac{m_0 c^2}{\sqrt{1-\beta_{min}^2}} = \frac{m_0 c^2}{\sqrt{1-n^{-2}}} \tag{2.1}$$

where m_0 is the rest mass of the charged particle (electron and positrons in the case of electromagnetic showers). At the altitude of the MAGIC telescope site, the refraction index of the air is $n_{2200} \sim 1.0003$: the threshold energy for electrons and positrons and is $E^e_{thr} = 26\,\mathrm{MeV}$ and the one for protons is $E^p_{thr} = 47\,\mathrm{GeV}$. Cherenkov photons are generally emitted at small angles ($\vartheta \sim 1^\circ - 2^\circ$). The Cherenkov radiation emitted by an air shower is the superimposition of the Cherenkov light emitted by the single particles and illuminates an area on ground of radius $\sim 100 - 150\,\mathrm{m}$. The Cherenkov light is emitted in the range $300 - 600\,\mathrm{nm}$, but it suffers attenuation and scattering, mainly due to Rayleigh dispersion[1], and at ground it peaks in the UV range at $\lambda \sim 300 - 350\,\mathrm{nm}$.

2.1.3 Imaging Atmospheric Cherenkov telescopes

The technique of imaging atmospheric Cherenkov telescopes is illustrated in Fig. 2.4: Cherenkov light is collected with mirrors, focused and reflected into a camera made of photo-multipliers. The signal is processed by a fast readout system and recorded by a DAQ for off-line analysis. The main background in this technique is the Cherenkov radiation from hadronic showers and it is discriminated from the signal on basis of shape and orientation of the shower image (Fig. 2.5). Particle cascades initiated by γ rays produce compact and elongated images and are closely aligned with the source position. Hadronic showers generate images of irregular shapes (longer, wider and fluctuating) and, since hadronic cosmic rays constitute a diffuse background and are not coming from a particular source, have random arrival directions. Camera images (after noise subtraction and cleaning which removes the effects of the night-sky-background, which is diffuse optical light - see Section 2.2.2) are fitted with ellipses whose axes are the second moments of the light distribution (width and

[1]Rayleigh dispersion is absorption of UV light by air molecules smaller in size than the wavelength of the light.

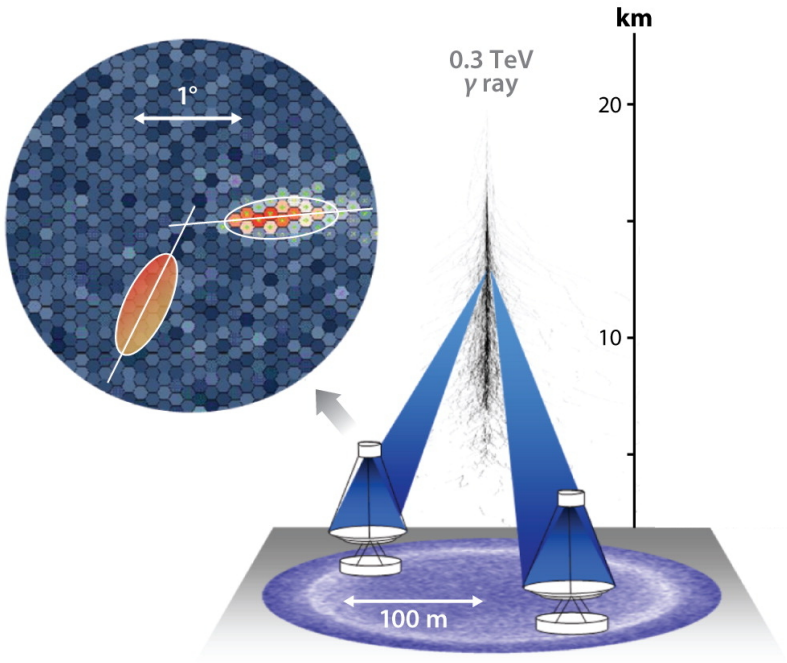

Figure 2.4: The imaging atmospheric Cherenkov technique: a γ ray of 300 GeV initiates an electromagnetic shower and Cherenkov light is emitted. The short light pulse is reflected by telescopes mirrors into a camera producing an elliptical image. The images obtained by different telescopes are combined in a 3-dimensional reconstruction of the shower (adapted from [112]).

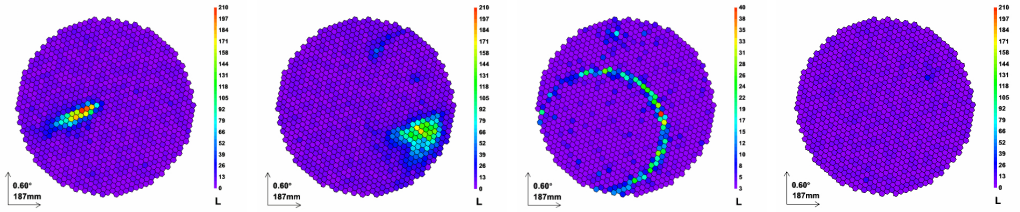

(a) γ ray; **(b)** proton; **(c)** muon; **(d)** NSB.

Figure 2.5: Images registered by the camera of MAGIC telescopes generated by (a) a γ ray (b) a proton (c) a muon (d) the night-sky background (NSB)[1]. Images are first cleaned, to remove the effects of the night-sky background, and fitted with ellipses whose parameters are used to discriminate between γ-ray and hadronic showers (see Section 2.2).

length). If two or more telescopes are positioned within the Cherenkov light pool, single telescope images are combined in a 3-dimensional reconstruction of the shower (stereoscopic technique) achieving a better direction estimation and background rejection with respect to single telescope observations.

History of imaging atmospheric Cherenkov telescopes

The Whipple experiment, a Cherenkov telescope with a 10 m diameter mirror and a 2.6° field of view camera, detected for the first time Cherenkov light from air showers initiated by astrophysical γ rays. In 1989, γ rays coming from the Crab Nebula were discovered [191] and in the following years the first extragalactic sources (Markarian 421 [160] and Markarian 501 [161]) were detected. The imaging technique was applied to an array of telescopes with the HEGRA project: five telescopes each with 8.5 m reflective surface and 4.3° field of view were operated in the years from 1998 to 2002, discovering new sources (Cas A [16], M 87 [17], J2032+4139 [18]). Whipple and HEGRA experiments detected only the brightest TeV sources, for a total of $\sim$ 10 sources by the year 2000. With the present generation of imaging Cherenkov telescopes the sensitivities improved significantly and the number of detected sources is now ~ 150[2].

Currently, there are three major systems of imaging Cherenkov telescopes in operation: MAGIC, VERITAS and H.E.S.S., all arrays consisting of two or more telescopes. The first two experiments are located in the Northern hemisphere, respectively in the Canary Islands and in Arizona, while the H.E.S.S. system is located

[1] The night-sky-background is diffused optical light: stars, diffuse galactic light, zodiacal light, aurorae and light pollution. It amounts to $\sim 7 \times 10^{11}$ photons $\mathrm{m^{-2} s^{-1} sr^{-1}}$ and depends on the sky position: it increases with increasing galactic latitude and zenith angle of observations.

[2] `http://tevcat.uchicago.edu/`

Figure 2.6: The MAGIC experiment: the two telescopes MAGIC-1 (left) and MAGIC-2 (right), located at the distance of 85 m and the counting house. The FACT telescope (close to MAGIC-2) and optical and solar telescopes of the "Observatorio del Roque de Los Muchachos" (in the background) are visible (photo by Robert Wagner `https://wwwmagic.mpp.mpg.de/`).

in the Southern hemisphere, in Namibia. The H.E.S.S. experiment consists of four 12 m telescopes forming a square, with large field of view (5°), optimal for morphological studies of galactic objects. In 2012, a fifth telescope with a 28 m diameter mirror was positioned in the centre of the array. The MAGIC and VERITAS arrays, consisting of two and four telescopes respectively, are instruments optimized for studies of extragalactic sources, with a smaller field of view (3.5°) and lower energy thresholds than H.E.S.S. telescopes (energy thresholds: MAGIC 50 GeV, VERITAS 100 GeV H.E.S.S. 100 GeV). This is a simplified treatment, all three experiments are equipped with complex instruments used for studying various fields of astroparticle physics. The MAGIC experiment is presented in greater detail in the following section, while a more detailed description of VERITAS and H.E.S.S. is available in the web pages of the projects (`https://veritas.sao.arizona.edu/`, `https://www.mpi-hd.mpg.de/hfm/HESS/pages/about/telescopes/`).

2.2 The MAGIC telescopes

The MAGIC telescopes (Fig. 2.6) are located on the Canary Island La Palma (28° N, 18° W), in the "Observatorio del Roque de Los Muchachos"[1], at an altitude of ~ 2200 m above the sea level. The first telescope, MAGIC-1 was built in 2002-2003 and later, in 2009, a second telescope, MAGIC-2, was added at a distance of 85 m. During the first years of stereoscopic operations, camera and readout system of the two telescopes had some differences, removed after a major upgrade in 2011-2012 [41, 42]. Since the observations presented in this work were performed in the years from 2011 to 2013 (before, in an intermediate phase with the new readout system but the old MAGIC-1 camera, and after the upgrades) the system in both configuration will be presented.

2.2.1 Hardware components

Frame and reflector

To achieve fast movement for follow-up observations of transients, the structure of the telescopes is made of carbon fibre tubes joined by aluminium knots and is positioned on azimuth drive rings of 20 m diameter made of railway trails. The telescopes have an alt-azimuth mount designed for operations in the range from $-90°$ to $\sim 320°$ in azimuth and from 100° to $-70°$ in elevation. Movement is powered by three motors for each telescope (two for the azimuth and one for the elevation) whose operations are controlled by a dedicated drive program. The camera is supported by an aluminium tubular arch and thin steel cables.

The two dishes have a diameter of 17 m, for a reflective area of $\sim 236\,\mathrm{m}^2$. MAGIC-1 has 964 aluminium mirrors of dimensions $\sim 50\,\mathrm{cm}\times 50\,\mathrm{cm}$, mounted in groups of four on 247 back-panels. The mirrors of MAGIC-2 are larger ($1\,\mathrm{m}^2$) and are of two types: 134 in aluminium, in the inner region, and 140 in glass, in the outer part. The parabolic shape is isochronous: the temporal structure of the light pulse is preserved. The timing information is used in the data analysis to improve the signal to noise ratio [43]. A dedicated heating system prevents ice formation and dew deposition on the mirrors. Deformations caused by bends of the structure and the dish sagging due to different gravitational loads are corrected with the *active mirror control* system: focusing is achieved by moving each panel in the directions up-down and right-left using two motors whose final position is saved into a look-up table. The procedure is repeated for different zenith angles. A CCD[2] camera (*SBIG camera*), located in the central part of the dish, observes simultaneously the direct

[1] `http://www.iac.es`

[2] CCD is the acronym for charge-coupled device.

image of a star and the reflected one into the *spectralon target* placed in front of the telescope camera. The CCD camera is used to focus the panels with the *active mirror control* and to measure the point spread function and the reflectivity at different wavelengths. The telescope pointing accuracy is monitored with another CCD camera (called *starguider camera*), located in the central part of the reflector, which compares the position of known stars around the source with reference LEDs around the camera.

Camera

The current cameras, located in the focus of the reflector, are arrays of 1039 photo-multipliers with quantum efficiency[1] peaking at $\sim 32\%$ at 350 nm (the intensity of Cherenkov light peaks at these wavelengths, in the blue band) and 1 inch diameter corresponding to an opening angle of 0.1° and a camera field of view of $\sim 3.2^\circ$. The photo-multipliers and their electronics (amplifier and an infra-red laser) are grouped in clusters of 7 or less (for a total of 169 clusters) and are mounted in a hexagonal configuration. Camera temperature is controlled with two aluminium plates with water channels located below the pixels.

The old camera of MAGIC-1, replaced during the 2011-2012 upgrade, had two different types of photo-multipliers: there were 397 inner photo-multipliers with 0.1° field of view and 180 outer photo-multipliers with field of view of 0.2° and had a wavelength shifter which increased their quantum efficiency up to $\sim 25 - 35\%$ in the blue band (MAGIC-2 and MAGIC-1 new camera have no wavelength shifter). With the new camera an increase of the trigger region area of a factor 1.7 has been achieved [173]. The trigger is organised in overlapping macro-cells which do not cover the entire surface of the camera. In the current configuration, the trigger region has a FoV of 2.5° including 547 photo-multipliers, while in the old MAGIC-I camera only inner photo-multipliers were included in the trigger region.

Trigger and readout chain

In order to minimize the weight of the telescopes, the readout electronics is not mounted in the camera but the photo-multipliers signal is transmitted to the counting house using optical fibres. Once the light-pulse reaches the receiver board is converted into electric signal by a photo-diode and amplified. The signal is then split into two branches: a digital one that goes into the trigger and an analogue one fed to the readout. The digital branch consists in a three level trigger:

- level-0: it is activated if the signal in a single pixel is larger than a discriminator threshold;

[1]The quantum efficiency is the number of photo-electrons emitted by the photocatode per incident photons.

- level-1: it is activated in case several pixels (e.g. 3 nearest-neighbours, 4 nearest-neighbours) have triggered the level-0 trigger within a time window of 10 ns. It is divided into hexagonal groups of 36 photo-multipliers which overlap with each other (macro-cells).

- level-3 stereo trigger: it is activated if the telescopes have both triggered level-1 within 100 ns.

The information from level-1 and level-3 is sent to the trigger selector (prescaler unit), together with the information from calibration and pedestal runs (see next section). Simultaneously a copy of the pulse is sent to the analogue to digital converter and stored into a ring of capacitors. In case the prescaler unit issues a trigger, the DAQ extracts from the stored information a time window of a fixed lengths and the event is registered together with its time stamp, trigger number and calibration information; a scheme of the readout is shown in Fig. 2.7. The analogue to digital converter of the present telescope configuration is the domino ring sample (DRS) chip version 4 [172]. Before the upgrade, MAGIC-1 was equipped with a MUX system [98] and MAGIC-2 with DRS2 [183]. The most important difference among these systems is their dead-times (MUX: $\sim 25\,\mu$s, DRS-2: ~ 0.5 ms, DRS-4: $\sim 27\,\mu$s), which need to be taken into account during the analysis (see Section 2.2.2).

Calibration system

The "calibration box", located in the central part of the mirror, consist of a UV laser, two attenuation filter wheels and an Ulbrich sphere[1]. During calibration runs the camera is illuminated by short light pulses of constant intensity. They are taken both at the beginning of observations and during the data-taking at a frequency of 25 Hz (interleaved calibration runs). Pedestal runs on the other hand are runs with random trigger and are taken at the beginning of the night, once the electronics has reached a stable temperature with camera lids closed (pedestal subtraction runs) and, with the camera open, during observations. The calibration is aimed at

- measuring the conversion factor from readout counts to number of photo-electrons (updated with the interleaved calibration);

- measuring the difference in the signal arrival time at different photo-multipliers;

- adjusting the gain of the photo-multipliers (high voltage "flat-fielding": the high voltage for each photo-multiplier is tuned so that the number of read-out counts is the same when photo-multipliers receive a pulse with the same number of photons).

[1] An Ulbrich sphere is a diffuser which, through multiple scattering reflection, diffuses isotropically the light.

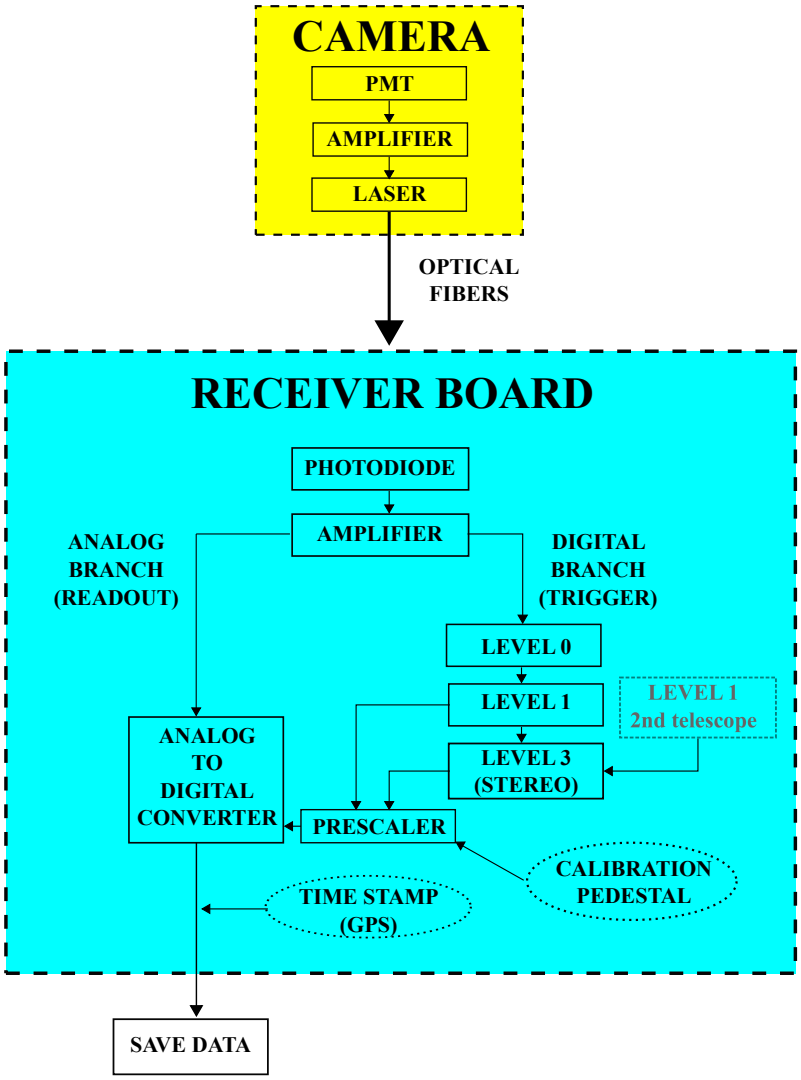

Figure 2.7: A scheme of the readout of the MAGIC telescopes: the signal measured by the photo-multipliers in the camera is transmitted using optical fibres to the counting house, where it is re-converted into an electrical signal and split into two branches: the trigger system and the readout system, after which is registered by the DAQ.

Weather and atmosphere monitoring

The atmosphere and the weather conditions are monitored with different systems:

- weather station: measures temperature, relative humidity, average wind speed, wind gusts and wind direction;
- pyrometer: an infra-red camera which measures the sky temperature. Since the cloud temperature is proportional to altitude, the pyrometer estimates the cloud height and the cloud coverage;
- lidar (light detection and ranging): estimates the cloud coverage by measuring the back-scattered light from a laser beam at 532 nm;
- all-sky camera: a camera with fish-eye lens which can detect clouds over the whole sky;
- electric field mill: measures the atmosphere electric field and detects lightnings.

The information collected by the different subsystems is displayed on a web-page, for monitoring during operations, and stored in the subsystem reports, which are merged to raw data in the first step of the analysis chain, to be used for the quality check.

Central Control system

The central control system is aimed at configuring, monitoring and coordinating the actions of different subsystems, which are all controlled by their own software. The central control system has a graphical interface, where the status of the telescopes is displayed: it is possible to access the subsystem and take actions and information on camera pixels such as current, high voltage, individual pixel rate, trigger rate are shown.

Operation of the telescopes: data taking nights

The MAGIC telescopes can be operated during dark nights and nights with moderate moonlight (observations are possible during up to 75% of the moon phase), for an overall scheduled observing time of $\sim$ 2200 hours per year ($\sim$ 1600 hours of dark time, $\sim$ 600 hours of observations with moonlight). Adverse atmospheric conditions such as high cloudiness, high humidity or rain, strong wind and calima (sand of the Sahara desert driven by winds over the Canary Islands) affect negatively the quality of the data and in the most extreme cases (rain, strong wind) the telescopes cannot be operated, reducing the observation time by $\sim 40 - 60\%$. Exceptionally, during

the years 2011 and 2012 the telescopes were not operated for several months due to the upgrade of the readout system and MAGIC-1 camera.

Ever since the construction of MAGIC-2, the telescopes are operated in stereoscopic mode: the hardware stereoscopic trigger (level-3) is used and only events seen by both telescopes are registered. Because of the small camera field of view, observations of selected sources are performed and two different tracking modes are possible: *on*-source (*on-off* observations) and false-source (wobble observations, [87]) tracking mode. During *on-off* observations, the source is in the centre of the camera, maximising the effective area for the sky position where the source is located. A draw-back of this mode is the necessity of additional time for *off* observations (with no source in the field of view) for the background estimation. In wobble-mode observations, each telescope is pointed with a small offset from the source (false-source, usually 0.4°) and, to minimise the effects of camera inhomogeneities, two or four positions located respectively at angles of 180° or 90° one from each other are used. In this case, *on* and *off* data are taken simultaneously and the observation time is reduced. A check of the telescopes and data-taking status is performed offline, the day after observations.

2.2.2 The standard analysis chain

The data of the MAGIC telescopes are analysed using the software "MARS" (MAGIC Analysis and Reconstruction Software [145]), a collection of programs and classes within the ROOT[1] framework . The analysis chain consists of several steps, starting with the raw data registered by the DAQ and ending with the calculation of physical quantities as significance of the signal, sky maps, spectrum and light curves. The analysis chain is divided into three phases: low-level processing done automatically by the on-site analysis (steps 1 to 3 in Fig. 2.8), intermediate analysis steps (steps 4,5 and 6 in Fig. 2.8) and production of physically relevant output (steps 7 to 10 in Fig. 2.8), which are both carried out by the analysers. The analysis is usually performed by at least two independent analysers: they both start with the same single-telescope data, but all the successive steps (quality check and good data selection, samples of Monte Carlo simulation and hadrons, cuts used in the different analysis stages) are independent. The analysis published in papers is the *main analysis* and the other ones are called *cross-check analyses*.

Signal extraction, calibration and image parameters calculation

The steroscopic trigger rate, under normal conditions, is $\sim 280\,\mathrm{Hz}$ of which $\sim 40\,\mathrm{Hz}$ are accidental triggers due to night-sky background and the electronic noise [41]. In

[1] `http://root.cern.ch`

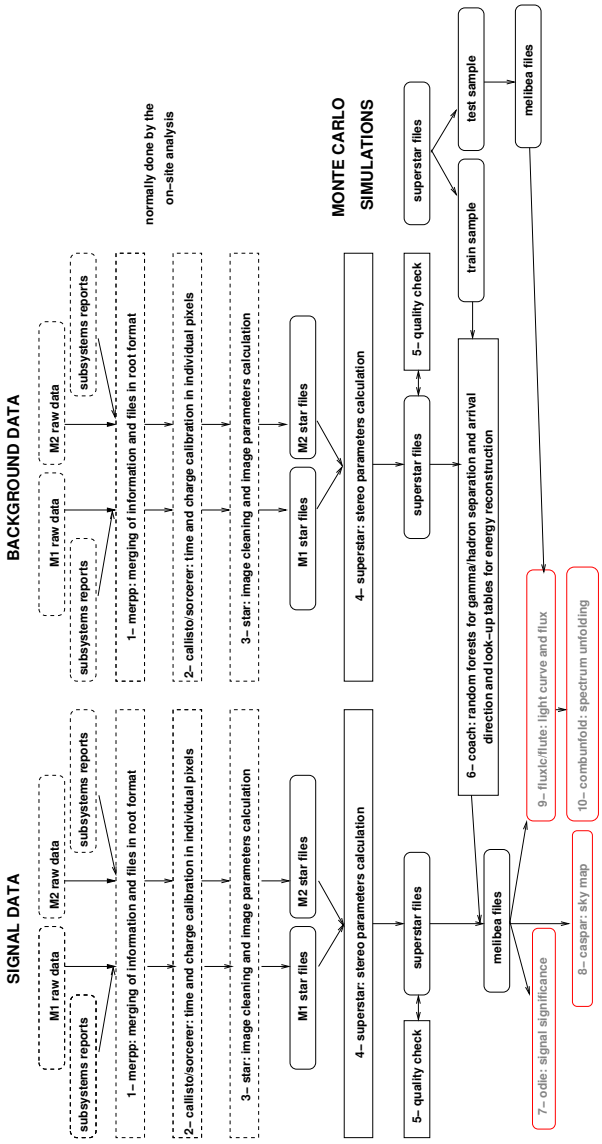

Figure 2.8: The analysis chain of the MAGIC data: each analysis step is performed with a dedicated software. The low-level processing (dashed boxes) is normally done automatically by the on-site analysis, and the analysers start combining single telescope files into stereoscopic files. Background data, observations containing a weak source or without sources in the field of view have to be analysed, since they are required together with Monte Carlo simulations in stereoscopic format as input for the "random forests" for the γ/hadron separation, arrival direction estimation and energy reconstruction look-up tables. The final products of the analysis are: signal significances, sky maps, light curves and spectra or flux upper limits.

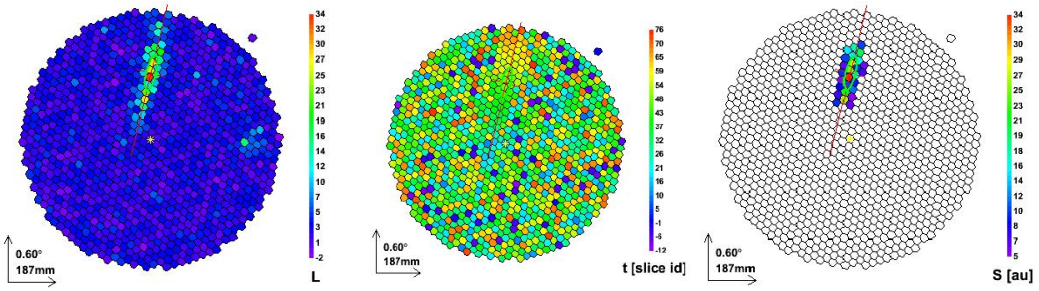

(a) Raw image; **(b)** arrival times; **(c)** after cleaning.

Figure 2.9: A real event recorded by MAGIC-II telescope: (a) the charge distribution in the camera (photo-electrons), (b) distribution of arrival times before image cleaning and (c) the cleaned image (arbitrary units) obtained applying the time-image cleaning algorithm [197].

order to remove images that are not generated by air showers a time-image cleaning is applied after time and image calibration. The surviving images are fitted with ellipses and a geometrical parametrisation of the images is applied.

The calibration consists of the following steps:

- subtraction of noise;
- signal extraction;
- conversion of signal from readout counts into physical units (photo-electrons);
- arrival time calibration.

First the baseline, estimated from pedestal runs, is subtracted. The signal is then extracted by integrating readout counts over a time window (6 time slices corresponding to ~ 3 ns) chosen because it gives the largest signal in a predefined time interval (60 time slices). This method, called sliding window method, is used with the domino ring sample readout system DRS2 (MAGIC-2, before the upgrade) and DRS4 (present configuration). With the old readout system of MAGIC-1 (MUX), the readout counts were instead interpolated with a cubic spline algorithm before integration.

The integrated readout counts are converted into photo-electrons applying in each pixel a calibration factor calculated from calibration runs (F-Factor or excess noise factor method). The arrival time is calibrated using a Fourier expansion of the function describing the pulse mean arrival time in a channel obtained from calibration pulses.

At the successive step of the reconstruction chain, pointing correction and image cleaning are applied. The pointing correction adjusts for bends of the telescope

structure, mostly dependent on the pointing position, and is computed using the *starguider* camera.

Air showers create signal on few to tens of pixels and their arrival time is within a few nanoseconds of each other, while events generated by the night-sky background and the electronic noise illuminate a large part of the camera and their arrival time is uniformly distributed. The time-image cleaning (Fig. 2.9) is aimed at removing pixels which are not part of a shower image and is a two step procedure: first *core* pixels are identified, which are pixels whose charge is above a certain threshold and arrival time is within a fixed time window from the mean arrival time. Then *boundary* pixels are determined, which are pixels neighbouring with at least one core pixel and whose signal is above a certain threshold and arrival time is within a fixed time window. After the upgrade of the MAGIC telescopes, the standard time-image cleaning has been replaced with the sum image cleaning [38, 39, 42]: instead of considering single pixels, a compact group of n next-neighour pixels ($n = 2, 3, 4$) is taken into account. The threshold on the charge and arrival time are respectively the summed charge and the average arrival time of the group of pixels. The values choosen as thresholds have been optimised such that the survival probability for an event generated by NSB or electronic noise is $\lesssim 6\%$ [42]. About $\sim 80\%$ of the events registered by the DAQ are left after the image cleaning in both telescopes. In the following steps an analysis based on the image parameters is applied in order to remove images generated by hadronic showers (the ratio γ-ray showers to hadronic showers is $1 : 10^3$ even for a strong source like the Crab Nebula) and to reconstruct the arrival direction and the energy of the events.

Single telescope images are fitted with an ellipse and the following parameters are computed (Fig. 2.10):

- image parameters:
  - *size*: total number of photo-electrons in the image (strongly correlated with the energy of the γ ray);
  - *width*: semi-major axis, related to lateral shower development;
  - *length*: semi-minor axis, related to longitudinal shower development;
  - *image centroid or CoG*: centre of gravity of the charge distribution;
  - *concentration or compactness*: fraction of image size contained in the two brightest pixels. Simulations first showed that the compactness is larger in γ-ray showers than in hadronic showers [111];
  - *leakage*: fraction of light contained in the outermost pixel ring in the camera;
  - *number of islands*: number of isolated pixel groups;

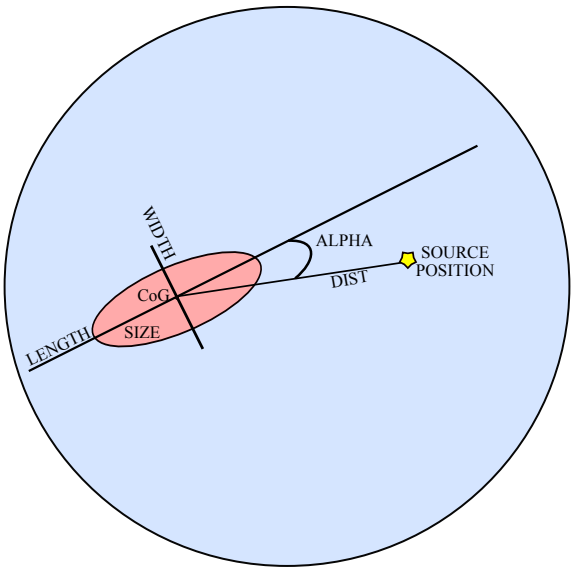

Figure 2.10: The shower image is parametrized using the Hillas parameters: *size* (ellipse area), *width* and *length* (ellipse axes), *image centroid* or *centre of gravity (CoG)*. The yellow star is the source position (position pointed by the telescope). *Dist* is the angular distance between the *image centroid* and the source position and α is the angle between the shower major axis and the line between the *image centroid* and the source position.

  - α: absolute value of the angle between the shower major axis and the line between the image centroid and the source position;
  - *dist*: angular distance between the image centroid and the expected source position in the camera (pointed position);

- time parameters:
  - *the root mean square of pixels arrival times*: the width of the arrival time distribution of all pixels;
  - *time gradient*: it indicates how fast the arrival time changes along the major axis of the ellipse.

In the standard analysis chain, the analysers start their analysis at this point and the first step they perform is the combination of single telescope images and the calculation of the 3-dimensional stereoscopic parameters:

- *shower direction*: incident direction obtained by geometrical reconstruction intersecting the major axes of the two ellipses (one for each telescope);

- *impact parameter*: distance of the shower axis to the telescope pointing axis (different for each telescope);
- *max height*: height of the shower maximum; it is a powerful parameter to distinguish between γ and hadron events.
- *Cherenkov radius*: radius of the Cherenkov light pool on the ground;
- *Cherenkov photon density*: density of the Cherenkov light pool on the ground.

Quality check

Runs affected by hardware problems and data taken in bad weather conditions are removed with the quality check. This selection is mainly based on the trigger rate, which depends on the zenith angle of observations and is strongly reduced in case of cloudiness. Runs with trigger rate varying more than $\pm 10\%$ from a reference value are discarded. The reference value is not defined a-priori for all analyses but is chosen taking into account the average trigger rate of the data to analyse, considering the mean value of the entire campaign compared to nights with excellent weather conditions. A fraction of MAGIC observations is performed during moderate moonlight; these data can be analysed together with dark night observations since images parameters are not affected by the presence of moonlight but during the quality check a cut on the camera current is applied. Moderate moonlight causes a higher night-sky background resulting in a signal with larger values of the camera current and, if the current exceeds a certain threshold, the runs are removed.

The quality check can be performed either for the two telescopes separately or successively with files in stereoscopic format. In the latter case, a large fraction of problematic events are already rejected by the stereoscopic reconstruction.

Gamma/hadron separation

The vast majority of the images are hadron induced showers (as already mentioned, the ratio γ-ray to hadrons initiated showers is $1 : 10^3$ for a strong source like the Crab Nebula). In order to discriminate between signal (γ-ray events) and background (hadron induced showers) a tree classification method called "random forest" is used [24, 57]. With this technique a background rejection better than 90% can be achieved [42]. A collection of decision trees is grown using randomly chosen features. In detail, the random forest is trained starting from a sample of electromagnetic showers and one of hadronic showers. The sample of γ-ray showers are Monte Carlo simulations of γ rays, while the hadronic sample consists of dedicated observations with no γ-ray source in the field of view (*dark patches*) or observations of very weak

γ ray sources. It is important to select both samples with characteristics similar to the analysed data, in particular with same range of zenith angle and the same observation period. A "tree of the forest" is "grown" in the following way: at the beginning the complete sample of hadronic and γ-ray showers are in a single node. The first parameter is randomly chosen in the set of available parameters and by applying a cut the sample is divided into two branches. The criterion for choosing the appropriate parameter cut is the minimisation of the Gini index [24]

$$Q_{Gini} = 4\frac{N_\gamma}{N}\frac{N_h}{N} = 4\frac{N_\gamma(N - N_\gamma)}{N^2} \qquad \in [0, 1] \tag{2.2}$$

where N, N_γ, N_h are respectively the total node population, the number of γ and the number of hadron in the node. The Gini index of the split is obtained combining the Gini indices of the two successor nodes (left l and right r):

$$Q_{Gini,split} = 2\left(\frac{N_{\gamma,l}}{N_l}\frac{N_{h,l}}{N_l} + \frac{N_{\gamma,r}}{N_r}\frac{N_{h,r}}{N_r}\right) \qquad \in [0, 1] \tag{2.3}$$

and its minimisation provides not only the value of the cut but also the choice of the parameter to use. The process is repeated until either the number of events in a node is lower than a predefined minimum (usually 3) or only events of one type are left in the node. At this point, the parameter *hadronness* is computed

$$H = \frac{N_{bkg}}{N_{bkg} + N_{sign}} \tag{2.4}$$

where N_{bkg} and N_{sign} are the number of background and signal events at the end of the decision tree. The *hadronness* is a number in the range $0 - 1$ which describes the probability for an event to be generated by a γ ray ($H = 0$) or by a hadron ($H = 1$). Usually a forest consists of ~ 100 trees, and the final H is the average of the *hadronness* over all trees. The parameters used for growing the random forest are: *size, width, length, impact parameter, time gradient* of each telescope, the *zenith angle* and the *max height* and since they are all source-independent, *hadronness* is independent from the source position (for this reason the *hadronness* parameter is also used for calculation of sky maps).

Arrival direction reconstruction

The shower arrival direction is also determined using the "random forest" method. Since the major axis of the ellipse is the projection of the shower incoming direction in the camera plane, the source position lies on this axis at a certain distance, called *disp*, from the image centroid (Fig. 2.11). The *disp* parameter is calculated for each telescope separately using a "random forest" trained using Monte Carlo

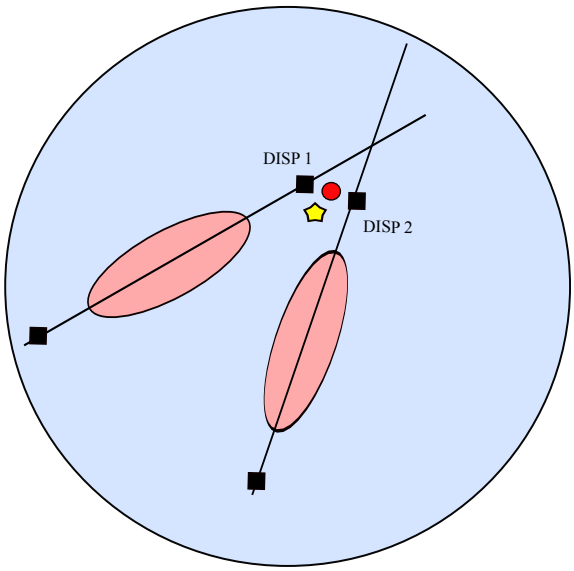

Figure 2.11: Estimation of source position using the *disp* method. For each single telescope image, two postions at a distance *disp* from the center of gravity of the image are possible (black squares). Among the four different pairs, the two closest positions are selected (but with distance $< 0.22°$ otherwise the event is rejected.) The *stereo-disp* (reconstructed source position, red circle) is the average of the two selected positions weighted with the number of pixels contained in each image. The true source position is indicated with a yellow star.

simulations of γ rays. For each image there are two possible solutions, on either side of the image centroid (ambiguity in head-tail discrimination). When single telescope image are combined, there are four possible combinations of positions. The closest pair is selected (if the lowest distance is $< 0.22°$ otherwise the event is rejected) and the *stereo disp* is the average of the chosen pair of positions weigthed with the number of pixels in each image. The *disp* parameter can be considered a *hadronness* estimator and used for obtaining additional background rejection. Indeed, since it is calculated using a "random forest" trained only on Monte Carlo samples of γ-ray events, it often gives non-consistent results for events generated by hadronic showers.

Energy estimation

The energy estimation is based on look-up tables derived from Monte Carlo samples of γ rays using the parameters *size, impact, max height* and the zenith angle of observations. Assuming that most of the light produced by a γ ray in the atmosphere is contained in a light pool of radius r_C, the mean photon density ρ_C within the light

pool can be calculated from the total light emitted at a given height. The look-up tables are filled with the value of $E_{true}\rho_C/size$ as a function of *size* and $impact/r_C$, for each telescope. The energy is reconstructed for each telescope separately and then the final value for the stereoscopic event is obtained by averaging the estimated energy for each telescope.

The random forests and the energy look-up tables are applied to the data and they assign energy, *hadronness* and arrival directions to signal events. After this step, the data contain all the information required for the computation of physically relevant output (significance of the signal, sky map, spectrum or flux upper limits and light curve).

Cuts and energy threshold of the analysis

In the successive steps of the analysis (calculation of significance of the signal, sky map, flux and light curve) the following cuts are applied to the data:

- *hadronness* cut: removes residual hadronic showers;
- *size* cut: since the *size* is proportional to the energy, this cut selects an energy range;
- energy cut: it is used to select a particular energy interval. Its choice is motivated by sensitivity and physical arguments (for example, to study the emission of a source in different energy ranges);
- ϑ^2 or *signal* cut: ϑ^2 is the squared angular distance between the catalogue source position and the reconstructed arrival direction obtained with the *disp* method[1]. Since γ-ray events are expected to be close to the source position while the background is uniformly distributed in the camera, the signal is expected to peak at zero, while the background distribution should be flat. This cut defines the signal region and is expressed in units of deg^2;
- *leakage, number of islands* cuts: are additional cuts used to obtain a purer sample of γ-ray events.

Predefined cuts on all parameters are available in the software MARS, but they need to be optimised and adjusted for the analysis of different objects. The most important cuts are the ones on *hadronness*, *size* and *signal* and are determined on

[1]The angular distance ϑ should not be confused with α which is the angle between the shower major axis and the line between the image centroid and the source position. An analysis based on the parameter α can also be performed, but it is a source-dependent analysis because relies on an assumption of the source position in the camera plane.

the basis of their efficiencies. In detail in the programs for the calculation of the significance and the sky map standard cuts for *hadronness* and *size* are available for different energy ranges: they have been computed obtaining a peak in the cuts efficiencies at $\sim 350\,\mathrm{GeV}$, $\sim 100\,\mathrm{GeV}$,$\sim 1\,\mathrm{TeV}$ respectively for *full range*, *low energy*, *high energy* analyses. In the code for the flux computation, the cuts on *hadronness* and *signal* parameters are determined with a user-defined efficiency computed from Monte Carlo simulations (typical range $70 - 90\%$), in different energy bins.

The energy threshold after cuts depends mainly on the zenith angle of observations and it is estimated from Monte Carlo simulations of γ rays. The analysis cuts are applied to simulation with zenith angle spanning over the same range of data and the peak position of the energy distribution is the energy threshold of the analysis.

Signal significance

Once the cuts have been applied to the data, the ϑ^2 distributions of signal and background events are normalized to the number of events and the quantities N_{on} (events in the signal region) and N_{off} (corresponding background in the signal region) are computed. The excess in the signal region is $N_{ex} = N_{on} - N_{off}$ and its significance is computed using the formula [126]:

$$S = \sqrt{2}\left(N_{on}\ln\left[\frac{1+\alpha}{\alpha}\left(\frac{N_{on}}{N_{on}+N_{off}}\right)\right] + N_{off}\ln\left[(1+\alpha)\left(\frac{N_{off}}{N_{on}+N_{off}}\right)\right]\right)^{1/2} \tag{2.5}$$

where $\alpha = t_{on}/t_{off} = 1$ (for Wobble observations) is the normalization factor expressed in terms of the effective time of *on* and *off* samples. In astrophysics, the threshold for claiming a discovery is $S \geq 5$ standard deviations (σ), which corresponds to a probability of $3 \times 10^{-7}\%$ that the excess is caused by a fluctuation of the background.

Sky map

A sky map is a 2-dimensional histogram of event arrival direction in sky coordinates aimed at studying the morphology of extended sources (source whose extension is bigger than the telescopes point spread function). Sky maps are also used in the analysis of point-like sources since they offer an independent method for the estimation of the signal significance with respect to the one described in the previous section.

First, a camera exposure model (the distribution of camera efficiency to detect Cherenkov light from air showers as a function of the camera polar coordinates) is computed from the distribution of event arrival directions in the camera plane.

In order to have a signal exposure map, if observations were performed in wobble mode, events with arrival direction in the *off*-source position are selected. The background distribution, or *off* map, is obtained by sampling 200 events from the camera exposure model for each event in the *on* map (event distribution). Both *on* and *off* maps are smeared with a Gaussian kernel accounting for the MAGIC point spread function and are rescaled so that the excess map maximum for a point source is the integral of the excess events. The relative flux map, which is the ratio of excess events to background events, and significance sky map based on the *test statistics* method [126] are calculated. It is also possible to compute a likelihood ratio sky map, which is a generalization of the *test statistics* method and it is affected by a smaller number of statistical uncertainties [125].

Spectrum and light curve

The γ-ray flux is the rate of γ rays per unit area and unit time. Related quantities often used in γ-ray astronomy are:

- differential energy spectrum: $d\phi/dE = d^2N_{ex}/(dEdA_{eff}dt_{eff})$
- integral flux: $\phi(E > E_{min}) = \int_{E_{min}}^{\infty}(d\phi/dE)dE$
- spectral energy distribution (SED): $E^2 \times (d\phi/dE)$
- light curve: evolution of the integral flux with time;

where $N_{ex} = N_{on} - N_{off}$ is the number of excess events within the signal region, A_{eff} is the effective collection area and t_{eff} is the effective time of observations, corrected for dead-time. The data are divided into energy bins in which cuts are applied (the analyser chooses the binning in energy by maximising the number of bins with an excess of $\sim 3\sigma$ significance). The effective area A_{eff} represents the collection area of an ideal detector which collects the same rate of γ rays as our real detector. It depends on the energy of the incoming particle and the zenith angle of observations[1]. The effective area is calculated using the formula $A_{eff} = A_{sim}\varepsilon_{ex}$, where the γ-ray efficiency $\varepsilon_{ex} = N_{ex}^{cut}/N_{ex}^{tot}$ is estimated from Monte Carlo events (total N_{ex}^{tot} and after cuts N_{ex}^{cut}). The A_{eff} rapidly increases for low energies close to the energy threshold ($\lesssim 100\,\mathrm{GeV}$), while for higher energies it stays constant.

[1]Low zenith angle observations have smaller collection areas because the light pools are small but the photon density is high, while in high zenith angle observations the showers are more distant and generate larger Cherenkov light pools but they have lower photon density.

Unfolding of the spectrum

The unfolding procedure corrects for distortion in flux measurement caused by the finite energy resolution of the instrument (of the order of 15-25% for the MAGIC telescopes [39, 42]) and for the fact that the energy of the incoming γ rays cannot be directly measured, but is estimated from correlated variables. In our discrete case, the problem can be formalised in the following manner: let E_{true} be the true energy of the γ rays, $(S_j)_{j=1,\dots,n_b}$ its unknown distribution, E_{est} the estimated energy, $(Y_i)_{i=1,\dots,n_a}$ its measured distribution, $(K_{ik})_{i,k=1,\dots,n_a}$ the covariance matrix of $(Y_i)_{i=1,\dots,n_a}$, and $(M_{ij})_{i=1,\dots,n_a,j=1,\dots,n_b}$ the migration matrix. In order to find an estimate of the true distribution S, the equation

$$Y_i = \sum_{j=1}^{n_b} M_{ij} \cdot S_j \qquad i = 1, \dots, n_a \tag{2.6}$$

has to be solved. The elements M_{ij} of the migration matrix, computed using Monte Carlo simulations, represent the probability that an event with E_{true} in the $j-$th bin migrates in the $i-$th bin of E_{est}. In general, $n_a \neq n_b$, and the problem cannot be solved inverting the migration matrix. It is an ill-posed problem and the direct solution of the system of Eq. 2.6 found by minimising

$$\chi_0^2 = \sum_{i,j=1}^{n_a} \left(Y_i - \sum_{k=1}^{n_b} M_{ik} \cdot S_k \right)^T \cdot (K^{-1})_{i,j} \cdot \left(Y_j - \sum_{l=1}^{n_b} M_{jl} \cdot S_l \right) \tag{2.7}$$

gives unstable results. Two different approaches are possible to get a stable result:

- regularisation: additional information is introduced (e.g. a priori assumptions on smoothness, size and shape of the solution). The methods implemented in the MAGIC software are the Tikonov's and the Schmelling's algorithms, in which the regularisation is achieved by adding a term in Eq. 2.7, and the Bertero's method, in which regularisation is achieved through iteration;

- forward-unfolding: it is an implicit unfolding in which a parametric function $S_k(q) = f(E_k; q)$ with parameters $q = (q_1, \cdots, q_{n_q})$ is used to represent S and Eq. 2.7 is minimised as

$$\chi_0^2 = \sum_{i,j=1}^{n_a} \left(Y_i - \sum_{k=1}^{n_b} M_{ik} \cdot S_k(q) \right) \cdot (K^{-1})_{i,j} \cdot \left(Y_j - \sum_{l=1}^{n_b} M_{jl} \cdot S_l(q) \right) \tag{2.8}$$

  with respect to the parameters q.

Once the unfolded distribution S_k has been calculated, the differential energy spectrum $d\phi/dE$ is computed. Parallel to the implementation of the unfolding algorithm, the spectrum is corrected for other effects as the absorption of γ rays due to the interaction with the extragalactic background light. A detailed description of the unfolding procedure and the algorithms implemented in the MAGIC software are presented in a dedicated paper [27]. In practice, the analyser has to specify the type of function for fitting the flux (simple power law, power-law with cut-off, broken power law) and select which bins in estimated and true energy are included. As the result must be independent on the algorithm chosen, it is common procedure to check that different methods produce compatible results.

Upper limits

In the case of observations with no significant detection, upper limits on the flux are computed. The standard method implemented in the MARS software is the *Rolke* method [25, 163]: the flux is assumed to be represented by a power-law function $\phi(E) = k \times (E/E_0)^{-\Gamma}$, with normalization factor k, spectral index Γ, and reference energy E_0. The flux upper limit in estimated energy is

$$\phi_{UL} = k_\star \times (E_\star/E_0)^{-\Gamma} \tag{2.9}$$

where the normalization factor $k_\star$

$$k_\star = \frac{N_{\Delta E_{est}}}{\int_0^\infty A_{eff}(E|\Delta E_{est})(E/E_0)^{-\Gamma} dE \Delta T} \tag{2.10}$$

is obtained from the upper limit of the number of excess events

$$N_{\Delta E_{est}} = \int_0^\infty \phi(E) A_{eff}(E|\Delta E_{est}) dE \Delta T \tag{2.11}$$

and the estimated energy $E_\star$ is computed from the average flux

$$\langle\phi\rangle_{A_{eff}} = \frac{N_{\Delta E_{est}}}{\int_0^\infty A_{eff}(E|\Delta E_{est})(E/E_0)^{\Gamma} dE} \times \frac{\int_0^\infty A_{eff}(E|\Delta E_{est})(E/E_0)^{\Gamma} dE}{\int_0^\infty A_{eff}(E|\Delta E_{est}) dE \Delta T} \tag{2.12}$$

$$= k_\star \langle (E/E_0)^{\Gamma} \rangle_{A_{eff}} \tag{2.13}$$

with $(E_\star/E_0) \equiv \langle (E/E_0)^{\Gamma} \rangle^{1/\Gamma}_{A_{eff}}$. Since the flux $\phi(E)$ depends on true energy, the integrals reported above are computed in true energy dE. In practice, the analyser selects the energy intervals in which differential upper limits are computed (common practice is to select the interval such that it contains more than one energy bin used for flux calculation) and the spectral index Γ, which is chosen using physical arguments (see Section 4.2.1).

2.2.3 Performance of the MAGIC telescopes

The performance of the MAGIC telescopes, expressed in terms of sensitivity, energy threshold, energy resolution and angular resolution, is summarised in Fig. 2.12 (pre-upgrade: [39], post-upgrade: [42]).

The angular resolution is the standard deviation of a two-dimensional Gaussian fit to the distribution of reconstructed event direction of the signal and corresponds to a radius containing 39% of γ rays of a point source. The angular resolution at 250 GeV is $\sim 0.07°$ and it improves at higher energies reaching $\sim 0.04°$. With the upgrades a factor $\sim 5 - 10\%$ improvement has been achieved (Fig. 2.12a).

The energy resolution is defined as the standard deviation of a Gaussian fit to $(E_{est} - E_{true})/E_{est}$ and its mean value is the energy bias introduced by this method and whose effects are corrected with the unfolding procedure (see Section 2.2.2). The energy resolution of the MAGIC telescopes, after the upgrades of 2011-2012, in the energy range of a few hundred GeV is 15% and the energy bias is below a few percent. The energy bias is larger both at low energies, due to energy overestimation (lower photon number, higher relative noise and worse arrival direction estimation) and at high energies, due to energy underestimation (truncated shower images). As shown in Fig. 2.12b, the upgrades of 2011 and 2012 lead to an improvement in the energy resolution at low and medium energies.

The sensitivity is the minimum flux that can be detected with a statistical significance of $5\,\sigma$, for a defined observation time[1]. The differential sensitivity of the MAGIC telescopes, before and after the upgrade is compared in Fig. 2.12c: the post-upgrade system has a better sensitivity, in particular at low energies ($E < 100$ GeV) where the same sensitivity of the pre-upgrade system can be achieved reducing the observation time by a factor of 2.5.

[1]Here the sensitivities are given for 50 hours of effective time of observations ($S_{50\,h}$). For other observation times t', the relation $S_{t'} = \sqrt{50/t'} * S_{50\,h}$ can be used.

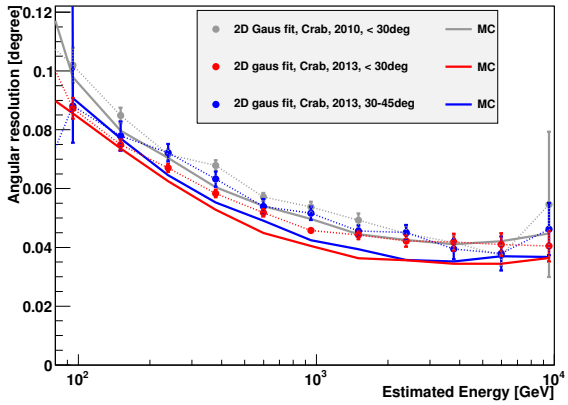

(a) Angular resolution;

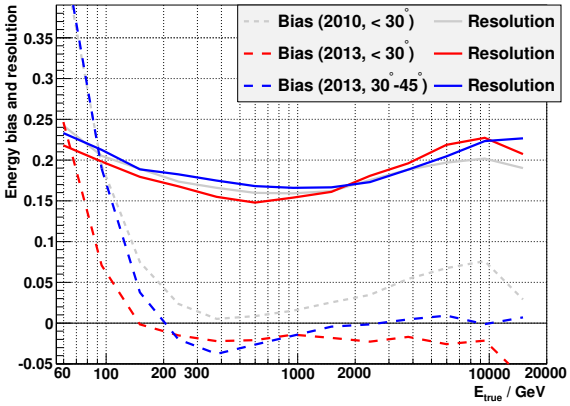

(b) energy resolution and bias;

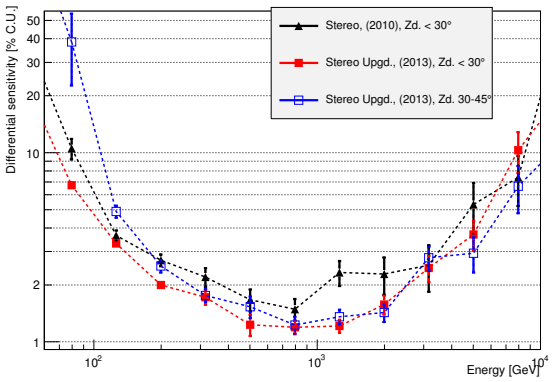

(c) differential sensitivity.

Figure 2.12: The angular resolution (a), the energy resolution and bias (b), and the differential sensitivity for 50 hours of effective time of observations (c) of the MAGIC telescopes after the upgrade for low zenith angles ($< 30°$ red) and medium zenith angles ($30° - 45°$ blue). For comparison, the performace of the pre-upgrade system for low zenith angles are shown in gray in (a),(b) and in black in (c) [42].

3

Active Galactic Nuclei

Active galactic nuclei (AGN) are galaxies which exhibit an unusual activity in their nuclear region. They are not powered by starlight, like "normal" galaxies, but by the release of gravitational energy of stellar material falling into a hole. They are the most luminous persistent sources in our universe, with luminosities that can exceed the ones of "normal" galaxies by factors of 10^4 concentrated in a tiny volume, which can be less than $\sim 1\,\mathrm{pc}^3$.

In this chapter some basic properties and observational characteristics of AGN and blazars in particular are presented. The general structure of an AGN together with the historical discoveries and the present time classification will be introduced first. In the following section the experimental features of blazars will be outlined, together with a review of the emission models for blazars. In the final section experiments whose data are combined with MAGIC observations into multiwavelength light curves and spectral energy distributions are briefly listed.

3.1 Structure, history and classification of active galactic nuclei

According to our present understanding [e.g. 65, 155], AGN (see Fig. 3.1) host in their central region a super massive black hole ($M \sim 10^8 - 10^9\,M_\odot$). The surrounding stellar material is accreted into a disc, the accretion disc. In the case of a

central black hole with mass $\sim 10^8 M_\odot$ and radius $r \sim 10^{-5}$ pc[1], the accretion disc is located within the first $\sim 10^{-4} - 10^{-3}$ pc. It typically rotates and develops two diametrically opposite and narrowly collimated jets which can extend over several pc (from 10^{-1} pc to ~ 4 Mpc of the giant radio galaxy 3C 236 [166]), and are clearly visible in the images at radio wavelengths. A hot, optically-thin corona surrounds the optically-thick accretion disc [70]. In AGN whose optical spectra show broad emission lines, fast moving gas clouds ($\sim 10^{-2} - 10^{-1}$ pc from the central region) are found, forming the so-called broad line region (BLR). Moving out, (~ 0.1 pc), a thick and cold torus of dust and molecules, which obscures the accretion disc, is present. Even farther from the central region ($\sim 1 - 10^2$ pc), in some cases, there is the narrow line region: a region of less dense clouds than the ones in the broad line region which cause absorption features in the optical spectra. The radio jets originate in the central region of the AGN and they may be regarded as a continuous with the core. They stream out energetic particles and magnetic field energy from the nucleus with relativistic velocities, so that the radiation is enhanced through Doppler boosting. The composition of the jet is still unknown: it could be an electron-positron pair plasma, proton-electron plasma or a combination of the two (electron-positron jets [83, 123]; protons/ions energetically dominated jets but with uncertain electron-proton number [66, 169, 170]). The energetic jets interact with the ionized gas which fills and surrounds the host galaxy; they are confined by a medium through which they drive a tunnel. Eventually, the ram pressure of the diffused gas stops the jets and hot spots of radiation form and originate radio lobes.

The first optical spectrum of an AGN was obtained by E. A. Farth in 1908 and the first class of AGN was recognized in 1943 by Carl Seyfert [167]. He was studying the optical spectra of a group of galaxies, thought to be bright nebulae and now called Seyfert galaxies, with star-like cores and the appearance of spiral galaxies. Their emission lines were broader and wider than the lines observed in other galaxies, with the hydrogen lines broader than the others. Later in 1955, two of these objects, NGC 1068 and NGC 1275, were detected as radio emitters. At the end of the 1950s, with the first radio surveys, the identification of the strongest radio sources with optical objects started. Quasars (quasi stellar radio sources), radio sources with stellar appearance, great luminosity and showing variability were discovered during such surveys. 3C 273 was among the first ones to be detected. It is the brightest known quasar, more that 100 times more luminous than our galaxy but with the redshift $z = 0.158$. In the following years other types of AGN were discovered: the radio-quiet quasars and the BL Lacertae objects.

The flow of history and the spread of discoveries over several decades resulted in a sort of zoology of AGN, where the sources were classified according to the

[1]The size of the various components given in the following description refer to a black hole with such dimensions [186].

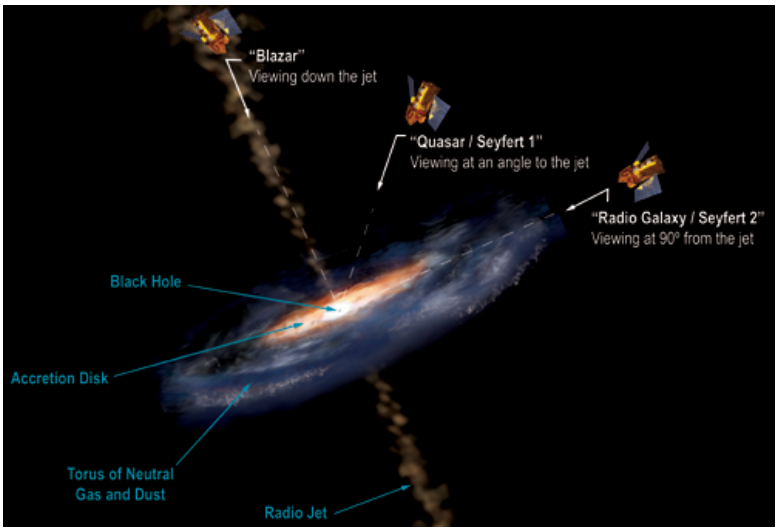

Figure 3.1: The structure of an AGN: the central black hole is surrounded by an accretion disc and a torus of dust. Two diametrically opposite jets propagate over distances of several parsecs. Depending on the observer's viewing angle, AGN are classified into different types (`http://www.nasa.gov/centers/goddard/news/topstory/2007/active_galaxy.html`).

observed properties. Only recently it has been possible to collect all these objects under the phenomenology of AGN in the "unified model" [186] and explain their different emission features in terms of orientation with respect to the observer. In addition, there is also great variety among objects belonging to the same class. Indeed, the features of such complicated objects depend on the relative importance of the various components.

Two big classes of AGN depending on the nature of the emitted radiation exist [7, 186]. If it is thermal radiation originating from in-falling material and it is mainly concentrated in the UV, optical and X-ray band, we call these sources *thermal/disc-dominated*. These represent the vast majority ($\sim 90\%$) of AGN. If the emission has non-thermal origin, being generated by magnetic fields and high energetic, relativistic particles, the AGN are called *non-thermal/jet-dominated*. In the latter case, radiation is produced all over the electromagnetic spectrum, from radio waves to very energetic γ-ray photons. This class corresponds to the one of radio-loud AGN. Non-thermal AGN are further classified according to the orientation of their jets with respect to the line of sight into blazars (one of the jets is pointing towards the observer) and non-aligned non-thermal dominated AGN (radio loud AGN with jets pointed at intermediate and large angles $\sim 15^\circ - 40^\circ$ with the line of sight). Blazars further divide into BL Lacertae objects (BL Lacs) and flat spectrum radio

quasars (FSRQs). Even though their continuum spectra are similar, they display diversity: sources belonging to the former class are characterised by a continuous spectrum with weak or no emission lines in the optical regime, while FSRQs show broad emission lines. The border line is the width of the strongest optical emission line: $< 5\mathring{A}$ in BL Lacs [186].

3.2 Phenomenology of Blazars

All blazars emit highly variable, non-thermal radiation spanning over more than ten orders of magnitude in energy.

The presence of emission lines in the optical spectra of FSRQs points to the existence of the broad line region, fast moving gas clouds located at distances of $\sim 10^{-2} - 10^{-1}$ pc from the central black hole. Low energy photons from the accretion disc or the broad line region, or from both regions, contribute to the overall observed emission. They eventually may absorb the VHE emission. Secondly, pronounced emission lines allow for a good measurement of the redshift, which is usually precisely determined for FSRQs, while for BL Lacs it is often unknown or limited to a range of values.

The spectral energy distribution of blazars has two broad peaks, the first between mm and soft X-ray wavelengths, the second in the MeV/GeV band [94]. Typically FSRQs have lower peak energies and higher bolometric luminosity than BL Lacs. In addition, their high energy peak is more prominent than the low energy one [97]. Blazars with larger bolometric luminosities have a spectral energy distribution with lower peak energies and a more prominent high energy peak, while in lower bolometric blazars the two peaks have approximately the same luminosity (Fig. 3.2). This trend was first outlined in the "blazar sequence" [88]. This traditional classification has been recently posed under discussion being a result of selection effects [96].

It has also been suggested that, since in general FSRQs are located at larger redshifts and are more luminous than BL Lacs, FSRQs evolve into BL Lacs, becoming less luminous and with weaker emission lines due to an increase in the beaming of the continuum (the Lorentz factor increases with cosmic time, equivalently decreases with redshift) [186, 187].

This dichotomy of blazars is observed also at higher energies. The second *Fermi*-LAT catalogue of AGN [13] reports that the high energy spectra of FSRQs is softer than the one of BL Lacs (the distribution of the spectral index peaks at $\sim 2.3 - 2.4$ for FSRQs and $\sim 2.0 - 2.1$ for BL Lacs). An extrapolation of this spectrum to VHE, the band in which the MAGIC telescopes are sensitive, shows that the detection in this range is not very promising. Indeed, out of the ~ 360 FSRQs detected by *Fermi*-LAT, we count only three representatives of this class at VHE to be compared with

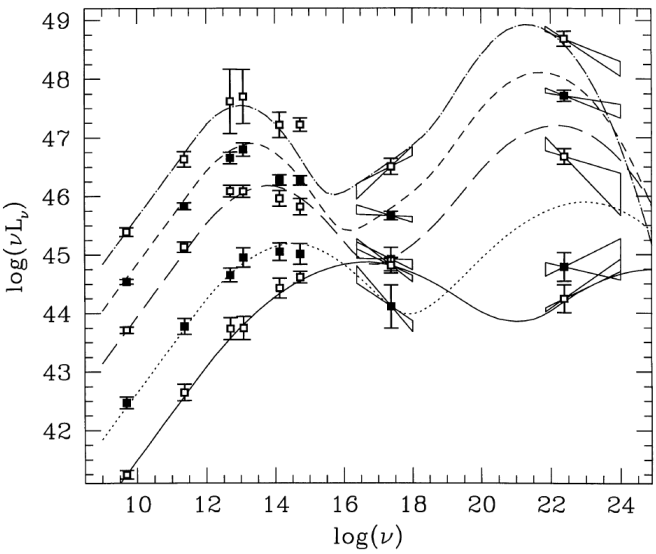

Figure 3.2: The "blazar sequence" [88]: blazars with larger bolometric luminosities have a spectral energy distribution with lower peak energies and a more prominent high energy peak, while in lower bolometric blazars the two peaks have approximately the same luminosity.

$\gtrsim 50$ BL Lacs[1]. An additional feature that makes the detection at VHE challenging is the distance at which FSRQs are found. In general they are located at larger redshifts than BL Lacs (redshift distribution for *Fermi*-LAT detected FSRQs peaks at $z = 1.0$ while for BL Lacs at $z \sim 0.1 - 0.2$ [13]), hence their VHE emission suffers strong absorption by low energy photons of the extragalactic background light.

In the last decade, thanks to the beginning of operations of three satellite-based telescopes, *Swift* satellite, *Fermi*-LAT and the Plank mission, the features of blazars have been studied using large and homogeneous samples of sources. The *Fermi*-LAT team published together with the AGN catalogues [6, 13], the spectral properties [5] and the multiwavelength spectral energy distributions [7] of the detected blazars. The high energy γ-ray emission has been fitted with simple power laws and broken power laws, resulting in lower spectral indices in BL Lacs. A distinctive feature has been found in FSRQs: they show spectral breaks in the energy range $1 - 10\,\mathrm{GeV}$ which have been interpreted as the result of absorption with low energy photons of the broad line region [157]. The difference in the distribution of the peak energies, being higher for BL Lacs, has been confirmed. This fact causes selection effects: the *Fermi*-LAT experiment is more sensitive to the BL Lac class and the vast majority of blazars detected to emit VHE γ-rays are BL Lacs (among more than 50 blazars

[1] `http://tevcat.uchicago.edu/`

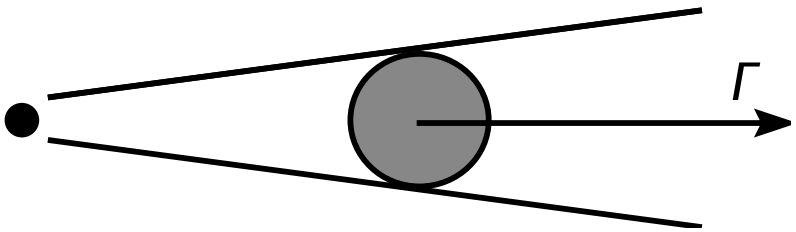

Figure 3.3: The blob geometry: a spherical and uniform blob moves down the jet with normalised speed β_Γ and Lorentz factor $\Gamma = 1/(\sqrt{1-\beta_\Gamma^2})$.

detected by Cherenkov telescopes, only 3 are FSRQs). Observations performed with the *Fermi*–LAT were also merged with the results obtained at lower energies by the *Swift* and *Planck* missions [97], confirming the main findings presented in [7].

Numerous models have been proposed to explain the emission of blazars. They differentiate among each other for geometry, location and size of the emitting feature, for the nature of the relativistic particles they contain and for their magnetic field.

In the simplest scenario, the emitting feature is a spherical and uniform blob moving down the jet with normalised speed β_Γ and Lorentz factor $\Gamma = 1/(\sqrt{1-\beta_\Gamma^2})$ (Fig. 3.3). It can be filled with relativistic particles (electrons in leptonic models, protons and ions in hadronic models) and, depending on its location with respect to the central engine, can interact with various populations of low energy photons (e.g. UV and optical photons of the accretion disc, the corona and the broad line region, infra-red photons from the torus). The propagation of the blob itself and the emitted radiation can be affected by differences in the magnetic field structure and in the geometry of the jet. Another scenario which offers a viable explanation to the variable emission observed in blazars is the colliding shell model in the blast wave geometry. An expanding fireball can create explosive releases of energy. Shells moving with different velocities can cause multiple explosions and in collisions between shells kinetic energy is converted into internal energy to be radiated. In terms of inferred spectral energy densities, the blob and the blast wave geometries are equivalent [77].

3.3 Emission models for blazars

The origin of the high energy emission of blazar is matter of current debate. As explained earlier in this chapter, the multifrequency spectral energy distribution of blazars is characterised by a double-peaked structure. The low energy peak extends from mm-radio frequencies up to infra-red and soft X-ray frequencies while the second peak is located at higher energies, from X rays to VHE γ rays.

The low energy peak results from synchrotron radiation of relativistic electrons, statement supported by observations of very high polarisation degrees ($\sim$ 50%), which cannot be produced by other processes. For the high energy peak instead there is no general agreement and various scenarios are plausible. They form two big groups: **leptonic models**, where the emission is caused only by relativistic electrons[1] and low energy photons, and **hadronic models**, where also protons are accelerated to energies high enough to radiate high energy and very high energy γ rays. In the former scenario, the high energy peak results from the inverse Compton process. According to models of the latter class, the high energy peak can be explained by different processes (or a combination of them): synchrotron radiation of relativistic protons, photo-meson production and synchrotron radiation of the charged unstable intermediates ($\mu^{\pm}$ and, at higher energies, $\pi^{\pm}$)[2].

The low energy photons can be internal to the emission region (photons emitted via synchrotron process by the electrons) or external, coming from [58]:

- **accretion disc**: the accretion disc emits a thermal spectrum in the optical/UV range, in some cases extending up to soft X-rays, visible as a *big blue bump* in the spectral energy distribution of FSRQs during low activity states (in some sources, like PKS 1510-089, it is always detected).
- **broad line region**: cold clouds of interstellar material orbiting around the black hole interact with the emission coming from the accretion disk through photo-excitation and photo-ionisation producing optical emission lines;
- **infra-red torus**: in some cases the emission from the accretion disc and the broad line region is absorbed by dust and re-emitted in the infra-red band;
- **cosmic microwave background**: the isotropic thermal radiation relict of the big bang.

3.3.1 Leptonic models

In leptonic scenarios the high energy peak observed in blazars is explained with the inverse Compton process: energetic electrons scatter on low energy photons (see Section 1.4.2). In the simplest scenario, the emission is produced in a single region and low energy photons are the synchrotron photons (SSC - synchrotron self-Compton models) [55, 117, 121, 133, 140, 180] or photons external to the emission region [78, 168]. In this section, the effects of the inverse Compton process considering different

[1] In leptonic models, the blob is supposed to contain both electrons and protons, but only electrons are accelerated to energies sufficient to radiate high energy γ rays.

[2] As it will be explained in the section on hadronic models, we refer to radiation-dominated jets and not to matter loaded jets.

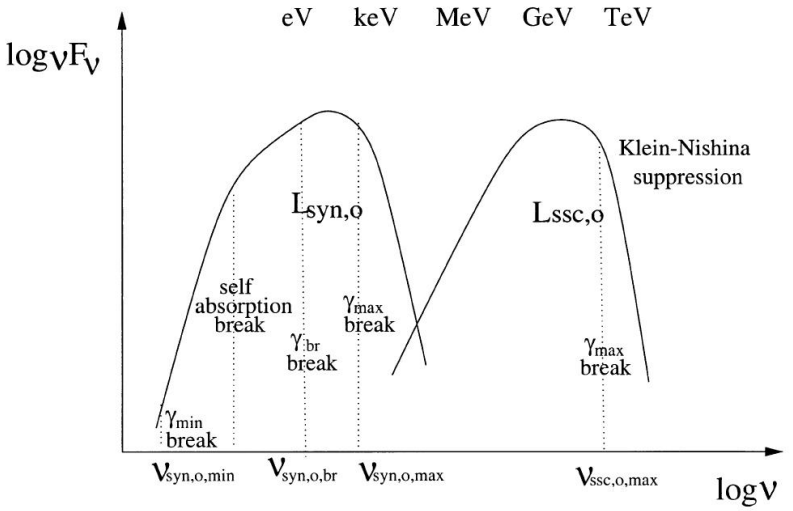

Figure 3.4: The spectral energy distribution in a synchrotron self-Compton scenario [124]. The low energy peak is synchrotron radiation of relativistic electrons (see Fig. 3.5): self-absorption, break and maximum energy of the electron population cause breaks in the emitted synchrotron spectrum. The high energy peak is due to inverse Compton process, targets being synchrotron photons.

low energy photons are summarised: spectral shape, peak and maximum energies are reported [58, 77].

The emission region is moving with Lorentz factor Γ and Doppler factor $\delta = 1/(\Gamma(1 - \beta_\Gamma \cos\vartheta)$ where ϑ is the angle between the direction of motion of the blob and the line of sight. The distribution of electrons has a low energy γ_{min} and a high energy cut-off γ_{max}, and a peak at γ_{peak}, and above the peak is a power-law function with index p.

The **synchrotron photon field** has a broad distribution in energy, and the SSC spectrum is a featureless continuum, extending over a wide range of energies (Fig. 3.4). The effects of Klein-Nishima suppression reduce gradually the emission at higher energies (see Section 1.4.2). Since the synchrotron spectrum is broad, extending from radio up to the UV band and in some cases soft X-rays, photons for scattering in Thomson regime are available ($\varepsilon\gamma_{max} \ll 1$) also for ultra-relativistic electrons ($\gamma_{max} \gtrsim 10^6$). The peak of the SSC spectrum (in Thomson regime) is

$$\varepsilon_{SSC}^{peak} \sim \varepsilon_{syn}^{peak} \gamma_{peak}^2 \tag{3.1}$$

where ε_{syn}^{peak} is the synchrotron spectrum peak. The high energy end of the spectrum, in Klein-Nishima regime, is related to the cut-off energy of the electron distribution

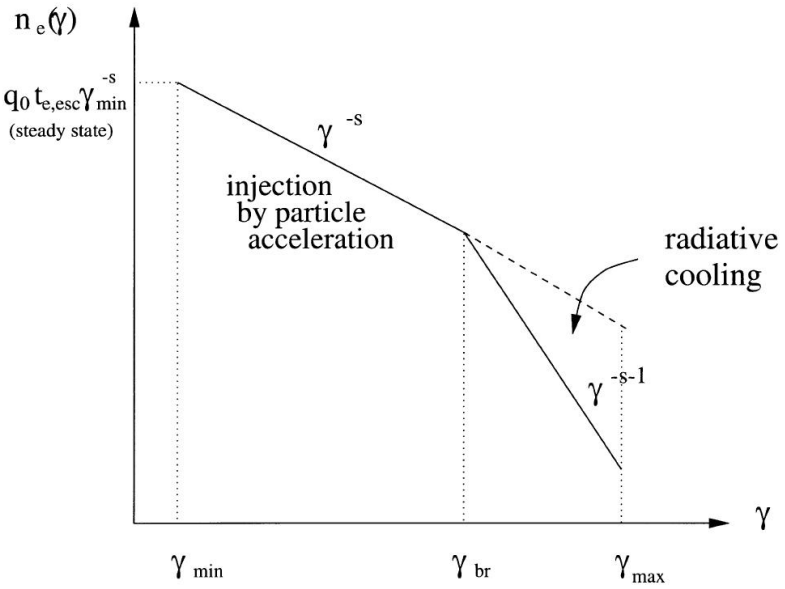

Figure 3.5: The spectrum of accelerated relativistic electrons [124].

γ_{max} by

$$\varepsilon_{SSC}^{max} \sim \gamma_2 \delta \tag{3.2}$$

hence electrons with high energy cut-off $\gamma_{max} \sim 10^6$ radiate TeV γ rays.

Often, together with the SSC emission, scattering on low energy photons external to the emission region contribute to the high energy flux. Consider the target photons listed in the previous section. They all produce a spectrum whose shape between the peak energy ε_{peak} and the maximum energy ε_{max} is a power law whose spectral index α is related to the spectral index of the electron distribution p by $\alpha = (p-1)/2$. The differences are mainly in the processes causing the end of the spectrum at high energies (either the electron maximum energy or the Klein-Nishima suppression). Depending on the geometry, different transformations are applied and low energy photons result de-boosted or blue-shifted in the rest frame of the emission region. In the following discussion photons energies are given in units of the electron rest mass. In detail:

- **accretion disc**: the disc emits in the UV range, so that the peak of disc emission is at $\varepsilon_{disc} \sim 10^{-5}$. If the emission region is located at a distance $d > \Gamma R_{disc}$, where R_{disc} is the disc size, the radial structure of the disc and the angular dependence of the disc emission may be neglected. In this geometry, disc photons enter the emission region from behind and are de-boosted of a

factor $\sim 1/\Gamma$. The peak energy of the inverse Compton is

$$\varepsilon_{disc}^{peak} \sim \varepsilon_{disc}\gamma_{peak}^2 \frac{\delta}{\Gamma} \tag{3.3}$$

and the high energy end of the spectrum, for electrons with $\gamma_{max} \lesssim 10^6$, is determined by the end of electrons distribution

$$\varepsilon_{disc}^{max} \sim \varepsilon_{disc}\gamma_{peak}^2 \frac{\delta}{\Gamma} \tag{3.4}$$

which for typical values of γ_{peak}, δ and Γ corresponds to MeV-TeV γ rays.

- **broad line region**: for optical lines a peak energy of $\varepsilon_{BLR} \sim 10^{-5}$ can be assumed. The emission region is located within the broad line region, low energy photons are isotropic and are boosted by a factor $\sim \Gamma$ in the rest frame of the emission region. In this frame, the peak of Compton emission is located at

$$\varepsilon_{BLR}^{peak} \sim \varepsilon_{BLR}\gamma_{peak}^2 \delta\Gamma \tag{3.5}$$

which corresponds to γ rays in the energy range detectable by *Fermi*-LAT (100 MeV-GeV). The end of the spectrum at high energies (multi-GeV) is due to the Klein-Nishima suppression.

- **infra-red torus**: it consists of low energy photons with $\varepsilon_{IR} \sim 10^{-7}$, which are blue-shifted by a factor $\sim \Gamma$ in the rest frame of the emission region. The inverse Compton peak is given by

$$\varepsilon_{IR}^{peak} \sim \varepsilon_{IR}\gamma_{peak}^2 \delta\Gamma \tag{3.6}$$

and for such low energy photons the Klein-Nishima suppression is negligible and the maximum energy is due to the electrons maximum energy

$$\varepsilon_{disc}^{max} \sim \varepsilon_{disc}\gamma_{peak}^2 \delta\Gamma \tag{3.7}$$

so that inverse Compton on low energy photons of the torus can produce γ rays up to very high energies (> 100 GeV).

- **cosmic microwave background**: are low energy photons with $\varepsilon_{CMB} \sim 10^{-9}$ which are blue-shifted by a factor $\sim \Gamma$ in the rest frame of the emission region due to their isotropy. Applying the same relations used for scattering on the infra-red torus it follows that the radiation from soft X-rays up to medium γ ray energies is emitted.

Simple single zone models are not always successful in reproducing the observed emission (fit of the spectral energy distribution, variability patterns) and often more complicated scenarios are used. Different populations of low energy photons can be considered where the high energy peak results from a super-position of inverse Compton on various target fields [93]. In some cases complex variability patterns indicate that the emission in different energy ranges is not generated in the same region and two or more emission zones are required. Another leptonic scenario is the *slow-sheat model* where the target field of photons comes from a slow outer layer of the jet [95]. In the following chapter different leptonic models are proposed to explain the multiwavelength emission, both spectral energy distribution and light curve, of the three studied blazars:

- 1ES 1727+502 (BL Lac): one zone synchrotron self-Compton model;
- 3C 279 (FSRQ):
  - one zone models considering two different populations of low energy photons (photons from the broad line region or from the infra-red torus: both can fit the spectral energy distribution of *Period-1*);
  - a two-zone model where the high energy emission is generated in an inner region of the blazar and the low energy peak in another one, located further down the jet (fits the spectral energy distribution and is consistent with the constraints from the multiwavelength light curve of *Period-2*);
- PKS 1510-089 (FSRQ): two different scenarios are proposed: a one zone model considering low energy photons from the infra-red torus (accounts only for the spectral energy distribution) and a slow-sheat model (not only fits the spectral energy distribution, but is consistent with multiwavelength constraints).

In general in leptonic models a population of accelerated relativistic electrons is assumed, whose spectrum is a power law function with a break at γ_{break} (where radiative cooling time scale equals escape time scale)

$$\frac{dN_e}{dE_e} = \begin{cases} K_1 E_e^{-p_1} & \text{for } \gamma \leq \gamma_{break} \\ K_2 E_e^{-p_2} & \text{for } \gamma > \gamma_{break} \end{cases} \tag{3.8}$$

and the photons radiated via synchrotron have a power law spectrum with indices $\alpha_i = (p_i - 1)/2$ for $i = 1, 2$ (Fig. 3.5). This approximation reproduces adequately the temporal evolution of the electrons energy distributions obtained solving the kinetic equation [121]. Self-consistent models are also available which include electrons acceleration via Fermi mechanisms [194]. Synchrotron self Compton models contain a number of parameters, specifying the properties of the emission region and of the population of electrons:

- emission region: size R, Doppler factor δ, Lorentz factor Γ and magnetic field B of the emission region;
- distribution of electrons: the minimum, break and maximum energy γ_{min}, γ_{break} and γ_{max}, the spectral indexes p_1, p_2 (usually $p_1 = 2$ for non-relativistic shocks or $p_1 = 2.2-2.3$ for relativistic parallel shocks and $p_2 = -(p_1+1)$), and the normalisation factors K_1 and K_2 related to the total number of electrons.

Estimates of such parameters are problematic, since independent measurements are not always available. For example, the magnetic field is an unknown quantity in blazars jets, and spectral energy distribution models with values of magnetic field spanning over orders of magnitude reproduce satisfactorily the observed behaviour.

For some parameters, however, it is possible to derive constraints from multi-wavelength observations. For example, the variability time scale t_{var}, which can be estimated from the light curves, limits the size of the emission region R according to

$$R \leq \frac{ct_{var}\delta}{1+z} \tag{3.9}$$

where z is the redshift of the source. Correlations and delayed emission among different energy ranges allow to establish co-spatiality and eventually determine the location of the emission region in the jet so that the relevant low energy external photon fields can be included.

3.3.2 Hadronic models

Hadronic scenarios present in literature are divided into two big groups: "fast jet" and "slow jet" models. In "fast jet" models, particles are accelerated linearly by large scale electric fields, which can be induced by the accretion disc, by the rotation of the central black hole in a magnetic field parallel to the disc rotation axis and by magnetic reconnection in the accretion disc or in the corona [52]. In "slow jet" scenarios particles are instead accelerated by relativistic shocks moving along the jet, and in the case that magnetic field and low energy photons are present, γ rays are produced. We can further distinguish between matter-dominated and radiation-dominated jets models. In the former class, proton-proton collisions take place [156]. These models are inefficient in case of optically thin (transparent to radiation) sources [48]. In models for radiation dominated jets, protons interact with magnetic field and low energy photons. The low energy radiation can be internal photons coming from synchrotron radiation of electrons [19, 131, 132, 147, 148, 195] or external ones [48, 59, 80] coming from the accretion disc, the broad line region, the infra-red torus and the cosmic microwave background.

The high energy peak of the spectral energy distribution is due to synchrotron radiation of protons in case of magnetic fields $\gtrsim 20\,\mathrm{G}$ (see Section 1.4.2). Such

models reproduce satisfactorily the spectral energy distribution of different types of blazars but do not account for fast variability. Synchrotron cooling time of protons is of the order of years, while observations showed variability time scales of days and hours. With lower values of the magnetic field, photon-proton interactions via photo-meson and Bethe-Heitler pair production are the dominant processes. Target photon fields in the AGN environment are the ones listed at the beginning of this section and the minimum energy of protons required for interacting via photo-meson and Bethe-Heitler processes can be computed from

$$\sqrt{s_{thr}^{pm}} = m_p c^2 + m_{\pi^0} c^2, \qquad \sqrt{s_{thr}^{BH}} = m_p c^2 + 2 m_e c^2 \tag{3.10}$$

which are the threshold energies for photo-meson (Eq. 1.19) and Bethe-Heitler pair production (Eq. 1.20) presenten in Section 1.4.2, and appling the same argument used for leptonic models. If the magnetic field is high enough the unstable charged intermediate states $(\mu^{\pm}, \pi^{\pm})$ emit synchrotron radiation because the synchrotron loss time scale becomes shorter than the decay time scale. The emitted synchrotron radiation will have higher energies than the one emitted by protons but on the other hand the flux will be smaller. Another contribution to the high energy emission in hadronic models is the cascade emission. Since the threshold conditions of Eq. 3.10 need to be satisfied, the initial energies of protons are so high that the secondary particles they produce initiate pair cascades which depending on the ratio between magnetic field and photon energy density can be synchrotron or Compton supported (in synchrotron supported pair cascades, the dominant energy loss process of the pairs is synchrotron radiation while in Compton supported cascades pair production alternates to Compton scattering).

The spectral energy distribution resulting from a hadronic model is composed by several contributions, which have different importance depending mainly on the magnetic field strength. Since these processes have different time-scales, it is possible to have uncorrelated low and high energy emissions.

Generally, it has not been possible to select any of the above mentioned scenarios as correct for a whole class of sources, but the single-source approach has to be adopted.

3.4 The multiwavelength view

In the analysis presented in Chapter 4 very high energy data are combined with observations at lower energies: γ rays measured with satellite experiments, X-rays, UV, optical, infra-red and radio data. The instruments used for this work are listed in Tab. 3.1 and briefly described below.

Energy band	Instrument
γ rays ($\sim 100\,\mathrm{MeV}$ - $100\,\mathrm{GeV}$)	*Fermi*-LAT
	AGILE/GRID
X-ray	RXTE-PCA
	Swift-XRT
UV	*Swift*-UVOT
Optical	KVA
	Liverpool-RINGO2
	Sternward observatory
	Perkins
Infra-red	GASP-WEBT
Radio	VLBA (43 GHz)
	Metsähovi (37 GHz)
	OVRO (15 GHz)
	F-Gamma program (cm, mm)

Table 3.1: Multiwavelength instruments.

- **Gamma rays from satellites**. The energy range accessible with γ ray satellites borders with the one covered by Cherenkov telescopes: from $\sim 100\,\mathrm{MeV}$ to $100\,\mathrm{GeV}$ (Cherenkov telescopes observe VHE γ rays: $100\,\mathrm{GeV} \lesssim E \lesssim 10\,\mathrm{TeV}$). Gamma-ray detectors on board satellites work on pair-conversion: incident γ rays are converted into $e^- e^+$ pairs through thin layers of heavy materials and detected by a tracker (at early times chambers filled with gas were used, now solid state detectors). The energy is measured with a calorimeter. An anti-coincidence shield is used for rejection of charged particles. The distinguishing features from ground-based γ-ray experiments are the small effective area of the order of $\sim 1\,\mathrm{m}^2$ and the large duty cycle.

  Gamma rays of astrophysical origin were discovered in the 1960s by the military satellites VELA. The first survey of the γ-ray sky was performed by the EGRET instrument[1], on board the Compton Gamma Ray Observatory, operational in 1991-2000. Two γ ray experiments are currently taking data: *Fermi*-LAT [49] and AGILE [179]. They are pair-conversion instruments as

[1] `https://heasarc.gsfc.nasa.gov/docs/cgro/egret/`

filter	Effective Wavelength Midpoint λ_{eff} [μm]	Full Width Half Maximum (Bandwidth $\Delta\lambda$) [μm]
UVW2	0.21	0.05
UVM2	0.23	0.05
UVW1	0.291	0.08
U	0.36	0.04
B	0.44	0.10
V	0.55	0.08
R	0.70	0.21
I	0.90	0.22
J	1.25	0.3
H	1.62	0.2
K	2.2	0.6

Table 3.2: Photometric filters used in UV, optical and infra-red astronomy. There exists a large number of photometric systems, the values reported here belong to the UBVRI system [118, 146] and the parameters of *UVW2,UVM2* and *UVW1* bands are the specifications of the filter wheel of the *Swift*-UVOT telescope.

EGRET[1] but with better performances.

- **X-rays**. Because of their short wavelengths (< 1 nm), X-rays are not easily reflected by mirrors. The "grazing incidence" technique is used: mirrors are arranged in a way that X-rays are reflected at angles $\lesssim 2^\circ$ and focused into a detector (at earlier times and in RXTE-PCA proportional counters were used but current generation instruments like *Swift*-XRT use CCD detectors).

  The Rossi X-ray Timing Explorer (RXTE)[2], in operation from 1995 to 2012, consisted of three different instruments: the Proportional Counter Array (PCA; energy range: $2-60$ keV), the High Energy X-ray Timing Experiment (HEXTE; energy range: $15-250$ keV) and the All-Sky Monitor (ASM) scanning about 80% of the sky every orbit. In this work, data collected with PCA were used.

  The *Swift*[3] satellite is a currently operational satellite equipped with three instruments: X-ray telescope (XRT; $0.3-10$ keV), UV/Optical telescope (UVOT; $170-600$ nm) and Burst Alert Telescope (BAT; $15-150$ keV). The principal

[1] In EGRET a spark chamber was used for tracking particles trajectories while AGILE and *Fermi*-LAT are equipped with silicon strips detectors resulting in improved energy and spatial resolution and longer mission lifetime.

[2] `https://heasarc.gsfc.nasa.gov/docs/xte/xhp_geninfo.html`

[3] `http://swift.gsfc.nasa.gov/`

physical goal of the *Swift* mission is the study of γ-ray bursts but it is used also for monitoring *Fermi*-LAT sources and flaring blazars[1].

- **Optical and UV**. The observations we use in the optical band are of three types:
  - photometry: the brightness of objects is measured, often using filters (see Tab. 3.2);
  - polarimetry: polarisation is measured by placing a filter (polarimeter) in front of the detector. Only light whose electric field vector is parallel to the polarisation direction of the filter passes through it; by rotating the filter, different polarisations are measured.
  - spectroscopy: a spectrum of the object is obtained.

  The KVA (Kungliga Vetenskapsakademien)[2] telescope is a remotely controlled instrument located in the Canary Island of La Palma, close to the site of the MAGIC telescopes. It is used for long-term optical monitoring of blazars, within the Tuorla blazar monitoring program, and it is used as support for MAGIC (i.e. sending alerts of high activity states). It consists of two instruments mounted on the same fork: a 35 cm diameter telescope for photometric measurements in *B,V,R* bands and a 60 cm diameter Cassegrain telescope[3] with a CCD polarimeter for measurements in *B,V,R* bands.

  In this work data from the following instruments are used: the imaging polarimeter RINGO2 of the Liverpool telescope[4], located close to MAGIC site, the Bok 2.3 m telescope[5] of the Steward observatory (used for spectropolarimetry and differential spectrophotometry in support of *Fermi*), and the 1.8 m Perkins telescope[6] (photometry and polarimetry in the *R*-band).

  Techniques used for detection of UV radiation are basically the same ones used for optical light, with the main difference that atmosphere is opaque to UV radiation, hence observations in this energy range are possible only on satellites and balloons. UV data used in this work are from *Swift*-UVOT, a 30 cm diameter Ritchey-Chrétien telescope[7] with a filter wheel for observations in the *V,B,U, UVW1, UVM2,UVW2* bands.

[1] `http://www.swift.psu.edu/monitoring/`

[2] `http://www.astro.utu.fi/research/telescopes/`)

[3] A Cassagrain telescope consists of a primary concave mirror (a parabolic reflector) and a secondary convex mirror (hyperbolic), both aligned about the optical axis. The primary mirror has a hole so that light reaches the camera.

[4] `http://telescope.livjm.ac.uk/Info/TelInst/Inst/RINGO2/`

[5] `https://www.as.arizona.edu/bok-23m-telescope`

[6] `http://perkins.owu.edu/`

[7] A Ritchey-Chrétien reflector is a Cassagrain telescope with two hyperbolic mirrors.

- **Infra-red**. Observation in the infra-red band are usually carried out with optical telescopes. However, there is a problem for measurements in this energy range: telescopes themselves emit thermal radiation peaking in the infra-red band. This effect is reduced using cooling surfaces. Observations in the near-infra-red band (wavelengths of few micrometers) are performed at heights, larger wavelengths are measured with space-based instruments because of the absorption by Earth's atmosphere.

  In this work infra-red instruments part of the WEBT monitoring program are used (see below).

- **Radio**. Because of their low frequencies, radio waves are not absorbed neither by material in the universe nor by Earth's atmosphere, cloudiness or bad weather. Moreover, the Sun is not a strong radio emitter, so that observations in this energy range can be performed also during day time.

  Radio astronomy became a discipline on its own in the 1950s, profiting from the invention of the radar. Telescopes were characterised by excellent sensitivities, but poor angular resolution $\vartheta \approx \lambda/D$, where λ is the observed wavelength and D the telescope diameter. Higher angular resolution is now achieved using interferometry: different radio telescopes are located all over the world and single telescope data are combined together into radio images (the European VLBI Network[1] and VLBA[2]).

  In the list of radio telescopes reported in Tab. 3.1 there are both single dish telescopes and interferometers arrays:

  – single telescopes: Metsähovi[3], OVRO[4], Effelsberg[5] and IRAM[6] telescopes part of the F-Gamma program [46, 90];

  – arrays: VLBA (43 GHz) part of the blazar monitoring program of Boston University[7].

- **GASP-WEBT monitoring program**[8]. The Whole Earth Blazar Telescope (WEBT) is a network of about 40 telescopes in the optical, near-infra-red, and radio frequencies located all over the world used for continuous and long-term

[1] http://www.jive.nl/
[2] https://public.nrao.edu/telescopes/vlba
[3] http://metsahovi.aalto.fi/en/
[4] http://www.ovro.caltech.edu/
[5] http://www.mpifr-bonn.mpg.de/en/effelsberg
[6] http://www.iram-institute.org/EN/30-meter-telescope.php?ContentID=2&rub=2&srub=0&ssrub=0&sssrub=0
[7] http://www.bu.edu/blazars/VLBAproject.html
[8] http://www.to.astro.it/blazars/webt/

observation of blazars. After the begin of the *Fermi* and AGILE missions, the GLAST-AGILE Support Program (GASP) is monitoring a list of γ-ray blazars.

4

MAGIC observations of blazars

In this chapter the results of MAGIC observations for three blazars are presented: 1ES 1727+502, 3C 279 and PKS 1510-089 (Fig. 4.1). The BL Lac 1ES 1727+502 is a newly discovered source in VHE γ rays. The other two objects belong to the subclass of FSRQs and are known VHE emitters. These three sources were observed with the MAGIC telescopes for regular monitoring as well as during target of opportunity observations (triggered by high activity states in other energy bands). In addition to MAGIC results, multiwavelength data and a phenomenological interpretation will be presented.

4.1 1ES 1727+502, a newly discovered BL Lacertae object

The BL Lac 1ES 1727+502 is a close-by source (redshift $z = 0.055$ [76]) and is visible for telescopes located in the northern hemisphere only (Fig. 4.1). It was discovered to be a VHE emitter in 2011 by the MAGIC telescopes [31, 136].

The source 1ES 1727+502 was observed earlier, with the Whipple and the MAGIC-1 telescope, but none of these observation campaigns led to a significant detection [33, 115]. Flux upper limits are summarised in Tab. A.1.

Fermi-LAT measured a hard spectrum for 1ES 1727+502, with index 2.0 in the first source catalogue, and 1.8 in the second one [3, 152][1]. Fig. 4.2 shows an extrap-

[1]The first source catalogue consists of the first 11 months of scientific observations of *Fermi*-LAT, which began on 2008 August 4, and the second one covers the first 24 months.

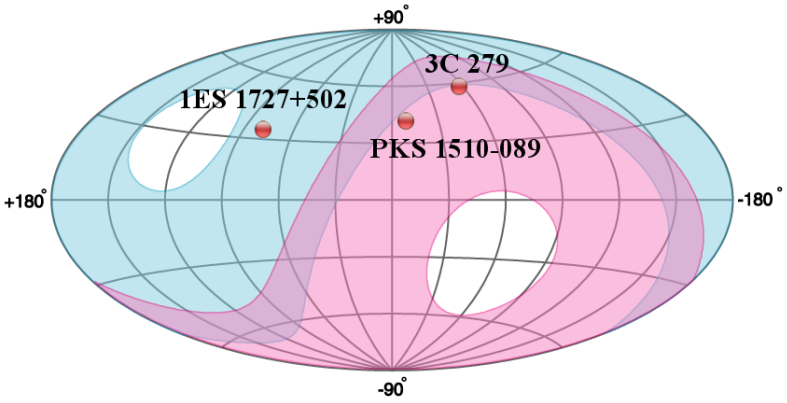

Figure 4.1: The position of the three blazars 1ES 1727+502, 3C 279 and PKS 1510-089. Superimposed, the portions of sky visible for the three existing Cherenkov telescopes: blue for MAGIC and VERITAS, pink for H.E.S.S. (`http://tevcat.uchicago.edu/`).

olation of the flux reported in the second *Fermi*-LAT source catalogue at energies above 10 GeV, taking into account the extragalactic background light (EBL). The resulting flux is comparable to the sensitivity of the MAGIC telescopes (before the upgrades, for 10 hours of observations), indicating that the source could be detected, even in absence of flares at high energies.

The source is included in an X-ray catalogue where a selection of promising candidates for TeV detection is presented [69], based on the connection between TeV and X-ray emission. Indeed, in synchrotron self-Compton leptonic models, both radio and optical fluxes measure the level of relevant seed photons that are up-scattered to TeV energies by electrons through inverse Compton process. From a list of 246 BL Lacs, obtained by merging several samples of BL Lacs which have information in the radio, optical and X-ray energy bands, the authors extract the best candidates for TeV detection. In total 33 sources, which are sources with brightest fluxes in radio and optical bands among a sample of bright X-ray sources, are selected. From this list, a subset of sources was extracted[1] and observed with the MAGIC telescopes. The observations that did not lead to a significant detection were merged and analysed using a stacking method: an excess with $4.9\,\sigma$ statistical significance was found, indicating that at least some of the sources of the sample are VHE emitters [33].

The arguments proposed by the X-ray catalogue [69], combined with the prop-

[1]Sources visible at the site of MAGIC telescopes, non detected at VHE, and fulfilling the criteria: redshift $z < 0.4$, X-ray flux at 1 keV $F_x > 2\,\mu$Jy, zenith angle $< 30°$ at culmination were selected.

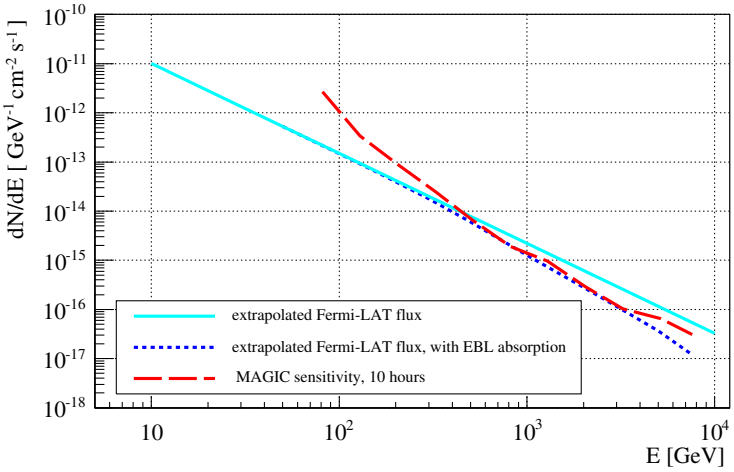

Figure 4.2: Predicted detectability of 1ES 1727+502 by the MAGIC telescopes. The flux measured by *Fermi*-LAT reported in the second source catalogue [152] is extrapolated to VHE (light blue solid line), corrected for EBL absorption (blue dotted line, [81]) and compared with the sensitivity of the MAGIC telescopes, before the upgrades, for 10 hours of observations (red dashed line, [39]).

erties measured by *Fermi*-LAT, motivated MAGIC observations of 1ES 1727+502 in 2011.

4.1.1 MAGIC observations and data analysis

The source 1ES 1727+502 was observed during 14 nights between 6 May and 10 June 2011, for a total of 20.2 hours of data. After quality selection, 14.0 hours were left, corresponding to an effective time (corrected for readout dead-time) of 12.6 hours. The zenith angle ranges from 22° to 50°, the observations were done in standard wobble mode and part of the data were taken under moderate moonlight and during twilight.

The significance distribution of 1ES 1727+502 is shown in Fig. 4.3a. The analysis was performed in the energy range from 150 GeV to $\sim$ 10 TeV, using the cuts $\vartheta^2 < 0.01$, *hadronness* < 0.16 and *image size* > 125 photo-electrons. An excess of 73.8 ± 15.0 events above the background 125.2 ± 5.0 was found, corresponding to a statistical significance of $5.5\,\sigma$ [126]. No significant signal was detected during single nights (see Tab. A.2). The γ-ray and background rates are respectively $(0.10 \pm 0.01)\,\mathrm{min}^{-1}$ and $(0.17 \pm 0.01)\,\mathrm{min}^{-1}$. From these rates, the integral flux above 150 GeV is estimated to be $(2.1 \pm 0.4)\%$ of the Crab Nebula flux.

The sky map (Fig. 4.3b) was obtained with the same cuts used for the calculation

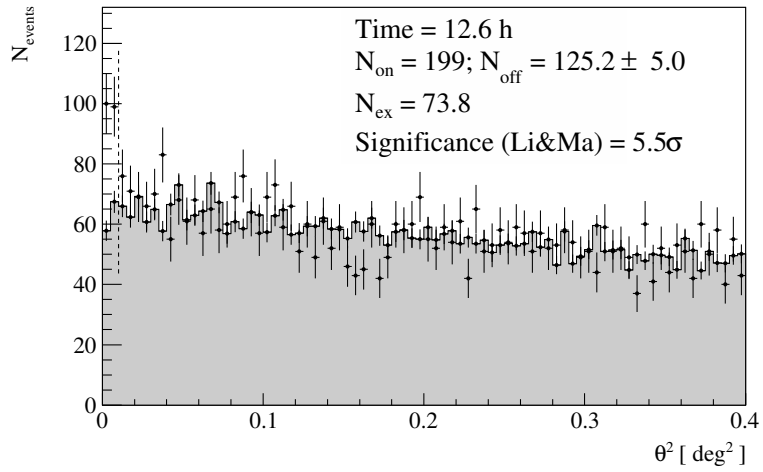

(a) Significance distribution

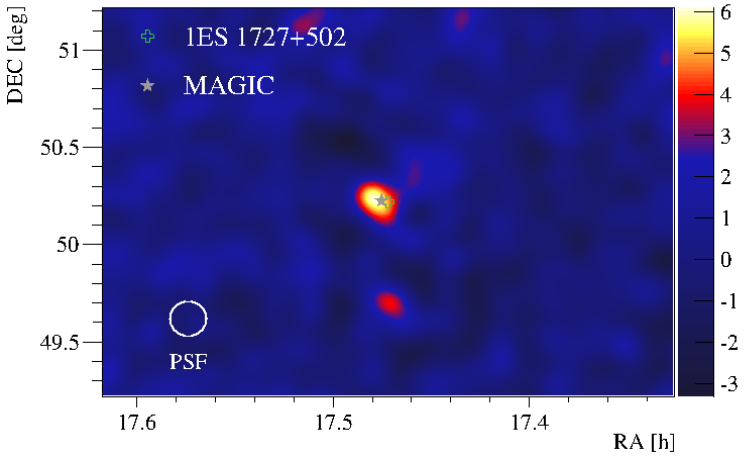

(b) Sky map

Figure 4.3: (a) Distribution of the squared angular distance ϑ^2 between the catalogue position of the source and the reconstructed γ-ray direction for ON-source events (black points) and OFF-source events (grey area). An excess at ϑ^2 values below 0.01 has been found, which corresponds to a statistical significance of $5.5\,\sigma$ (for more details see Tab. A.2) [31]. (b) The sky map of 1ES 1727+502: the source is point-like and the position of the excess (grey star) is consistent with the catalogue coordinates (green cross).

of the signal significance. The fitted position of the excess is consistent with the catalogue coordinates within $(0.032 \pm 0.015_{stat} \pm 0.025_{sys})^\circ$. By comparing the extension of the excess with the point spread function of MAGIC ($\sim 0.1^\circ$ [32]), we conclude that 1ES 1727+502 is a point-like source. Additional checks were performed using a generalized likelihood ratio test [125] to determine the significance of the *hot spot* present in the sky map below the source which was found not to be significant.

The spectrum was computed using 12 energy bins from 6.3 GeV to 400 TeV. The cuts were determined requiring a ϑ^2 efficiency of 90% and a *hadronness* efficiency of 75%, with allowed values $\vartheta^2 > 0.01$ and *hadronness* > 0.07. An additional cut on *size* > 50 photo-electrons has been applied. The spectrum was then unfolded using the forward-unfolding algorithm (see Section 2.2.2) and corrected for the absorption due to the interaction with EBL [81]. The obtained differential flux is described by a power law function $dF/dE = f_0(E/300\,\mathrm{GeV})^{-\Gamma}$, with flux normalisation $f_0 = (9.6 \pm 2.5) \times 10^{-12}\ \mathrm{cm^{-2}s^{-1}TeV^{-1}}$ and spectral index $\Gamma = (2.7 \pm 0.4)$.

The emission at VHE was constant during the entire period. The light curve shows a steady flux [31], and the absence of a significant detection during single nights (Tab. A.2) excludes variability on a daily-time scale.

4.1.2 Multiwavelength behaviour

Simultaneously with MAGIC observations, 1ES 1727+502 was monitored in the optical band and at high energies with the *Fermi*-LAT.

The source was in a low activity state in the **optical** band. In this energy range, it has been in a quiescent state for the last 10 years, showing only a single flaring episode during spring 2010[1], after which it returned to its low activity state in September 2010.

In the ***Fermi*-LAT band**, a flux higher than the average was measured: $(7.2 \pm 1.9) \times 10^{-9}\ \mathrm{photons\,cm^{-2}s^{-1}}$, the average flux of the first three years of observations being $(3.5 \pm 0.5) \times 10^{-9}\ \mathrm{photons\,cm^{-2}s^{-1}}$. No flare was identified and analysis of the light curve reveals that the emission is compatible with a constant flux [31].

Simultaneous optical and *Fermi*-LAT data were combined with MAGIC measurements together with archival *Swift* data in the **optical-UV** and **X-ray** band. The resulting multiwavelength spectral energy distribution (Fig. 4.4) has been fitted with a one-zone leptonic model [134]. The emission region is a blob with size R and magnetic field B propagating along the jet with Doppler factor δ filled with a population of relativistic electrons whose spectrum is described by a power-law function $N(\gamma) = K\gamma^{-n_1}(1 + \gamma/\gamma_{break})^{n_1 - n_2}$. In this scenario, the low energy peak is produced

[1]The high activity state in the optical band triggered MAGIC follow-up observations (the triggering criteria being an increase by 50% of the long-term average flux) but the data were discarded after quality selection.

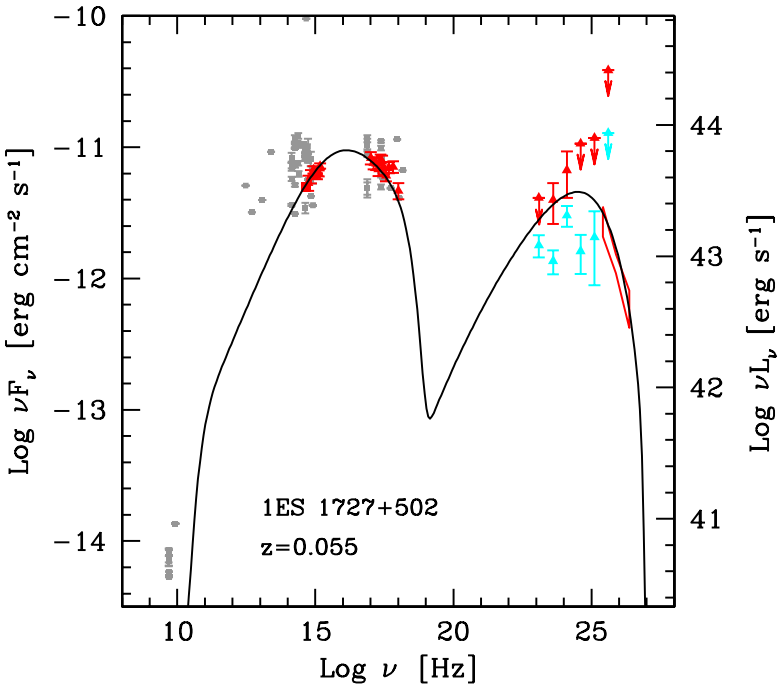

Figure 4.4: The multiwavelength spectral energy distribution of 1ES 1727+502 fitted with a one-zone synchrotron self Compton model [31]. The data used for the fit are shown in red: *R*-band optical data from KVA, archival UV-optical data from *Swift*-UVOT, archival X-ray data from *Swift*-XRT, *Fermi*-LAT data for three months of observations centred around MAGIC observations and MAGIC spectrum corrected for EBL absorption ([81], bow-tie). *Fermi*-LAT data for three years (from August 2008 to August 2011, cyan) and archival data (grey) from the ASI/ASDC archive (`http://tools.asdc.asi.it`) are also shown.

γ_{min}	γ_{break}	γ_{max}	n_1	n_2	$K\,[\mathrm{cm}]^{-3}$	$B\,[\mathrm{G}]$	$R\,[\mathrm{cm}]$	Γ
100	3×10^4	6×10^5	2	3.5	$8 \times 10^3\,\mathrm{cm}^{-3}$	0.1 G	$7 \times 10^{15}\,\mathrm{cm}$	15

Table 4.1: The parameters obtained fitting the multiwavelength spectral energy distribution of 1ES 1727+502 (Fig. 4.4) using a leptonic synchrotron self-Compton model [31]. From column one to column six the parameters describing the electron population are reported: the minimum, break and maximum Lorentz factors, the spectral indexes before and after the break and the electron density. In column seven to nine the properties of the emission region are listed: magnetic field, radius and Doppler factor.

by synchrotron radiation of the relativistic electrons and the high energy peak is the result of the inverse Compton scattering between electrons and synchrotron photons. The parameters obtained fitting the spectral energy distribution are summarised in Tab. 4.1. They are compatible with the ones obtained by other sources of this class (e.g., with the sample analysed in [181]).

4.1.3 Results of 2011 observations

The multiwavelength spectral energy distribution obtained with observations in 2011 confirms that 1ES 1727+502 is a typical representative of the subclass of high synchrotron-peaked sources (defined in terms of the frequency of the synchrotron peak: $\nu_s^{peak} > 10^{15}\,\mathrm{Hz}$). Indeed it has a dominance of the low energy/synchrotron peak and hard spectra at high energies. A one-zone synchrotron self-Compton model matches multiwavelength observations and the parameters obtained fitting the spectral energy distribution are compatible with the ones obtained by other sources of this class.

The discovery of 1ES 1727+502 demonstrates the importance of adopting various criteria for selecting the candidates for observations. Follow-up observations of high activity states at lower energy bands, mainly in the optical and high energy range, are a well-established strategy which often leads to discovery or detection of high activity states (e.g. optical triggers for 3C 279 [29, 37], high energy triggers for PKS 1222+216 and PKS 1510-089 [34, 35]). On the other hand, adopting a criterion independent of the activity states of other bands allows us to perform observations of quiescent states, fundamental for a study of BL Lac objects unbiased by the selection. Other sources discovered by the MAGIC telescopes, selected as promising VHE candidates from X-ray catalogues [69, 82], are: 1ES 1218+30.4 [23], PG 1553+113 [21], 1ES 1741+196 [53] and 1ES 0033+595 [137].

4.2 3C 279

The source 3C 279 was the first FSRQ to be discovered as a VHE γ-ray emitter [29]. With the redshift $z = 0.536$ [128] is one of the most distant VHE sources detected so far (Fig. 4.5).

The first γ-ray satellite that detected 3C 279 was EGRET [101], during a flaring episode in 1991. In the following nine years of EGRET operations, it was observed several times and detected every time, even during low activity and quiescent states. Current γ-ray experiments on board the satellites AGILE and *Fermi*-LAT have also observed and detected 3C 279. In this energy band, the source has the following properties:

- flux variability over two orders of magnitude, ranging from $\sim 10^{-7}$ photon $\mathrm{cm}^{-2}\mathrm{s}^{-1}$ during low activity states, to $\sim 10^{-5}$ photons $\mathrm{cm}^{-2}\mathrm{s}^{-1}$ during flaring episodes [135, 193];

- extremely fast variability, with a flux increase factor 2.6 in about 8 hours [193];

- spectrum with curvature, represented by a broken power-law function $dN/dE \propto E^{-\Gamma_1}$ for $E < E_{break}, dN/dE \propto E^{-\Gamma_2}$ for $E \geq E_{break}$, with a break energy

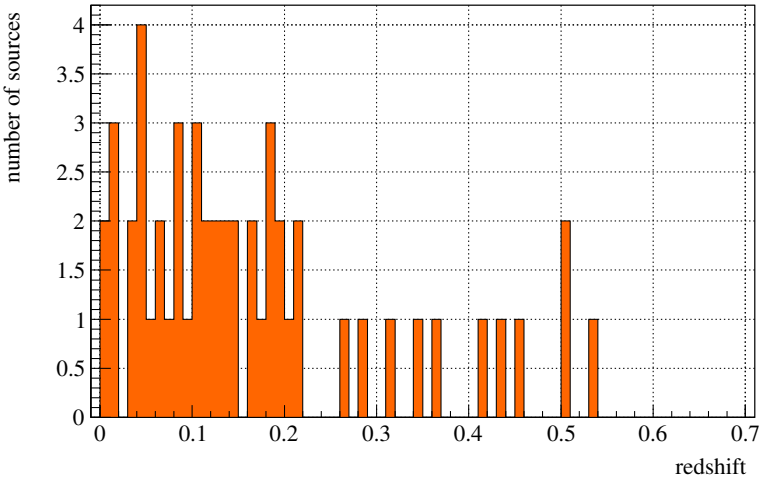

Figure 4.5: The distribution of the redshift of VHE active galactic nuclei (`http://tevcat.uchicago.edu/`) as of June 2014. Redshift measurements are available for 52 out of the 56 objects known at the moment. For three sources, not included in the plot, only limits are available: $z > 0.11$ for MAGIC J2001+435, $0.33 < z < 0.41$ for 3C 66A, and $z > 0.603$ for PKS 1424+240, the most distant one.

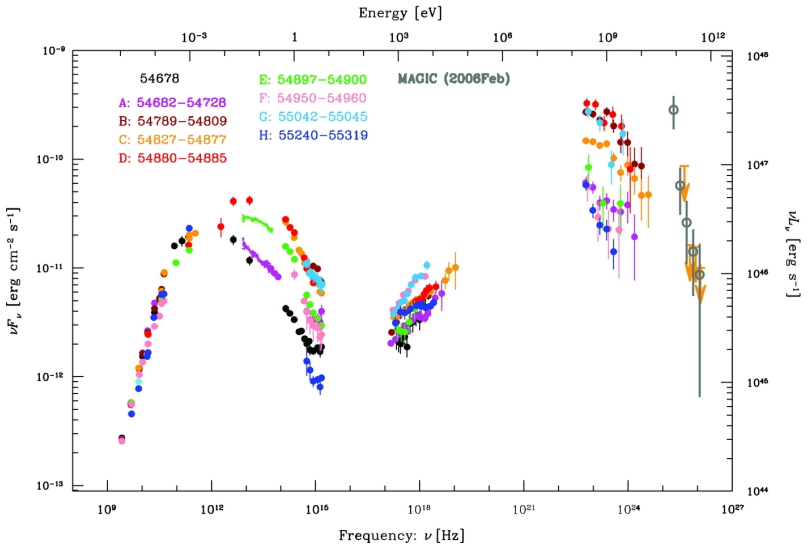

Figure 4.6: The spectral energy distribution of 3C 279 from radio band to γ rays obtained from August 2008 to August 2010 [107]. The two-year observations are divided according to the activity states of the source and are indicated with different colours. MAGIC observations that led to the discovery of the source at VHE γ rays are also shown (grey open circles). The double-peaked structure is evident, with the high energy peak dominating over the low energy one during high activity states.

E_{break} at a few GeV independent of the flux level and a spectral index varying from 1.8 to 3.5 [107].

The **X-ray** luminosity of 3C 279 is low, like for other FSRQs. The source 3C 279 showed flaring episodes, both isolated and correlated with variability at other wavelengths. Pronounced variations have been recorded, with a 20% intensity change in the energy range from 2 to 10 keV in less than an hour [129].

In low activity states, the emission in the **UV** and **optical** bands is dominated by the host galaxy and by the thermal radiation of the disk, while during high activity states synchrotron radiation prevails. Large amplitude variations have been measured in the optical band, with fluxes in the R band varying over up to two orders of magnitudes ($R \sim 12.5 - 17.5$), on time scales that range from years to hours.

Radio observations show a compact radio core with one-sided jet in which bright components, or knots, are ejected [119] and exhibit apparent superluminal motion [185, 196]. The ejection of new radio components from the core is correlated with flaring activity [192].

The radio and optical fluxes are partially **polarised**, as expected if the emission in these energy bands is synchrotron radiation. Radio polarimetry measurements indicate that the electric field vector is generally well aligned with the jet direction on parsec to kilo-parsec scales, implying a magnetic field predominantly perpendicular to the jet on those length scales. Several flaring episodes have been accompanied by an increase in the percentage of polarised flux and smooth rotations of the electric vector position angle, of both optical and radio or in a single band. This behaviour has been interpreted as an indication of a bend in the jet [1, 36].

The multiwavelength spectral energy distribution has the typical features of FSRQs (Fig. 4.6): two broad peaks, one extending from radio to UV frequencies and the other one from X-rays to γ-rays, peaking at a few GeV. During flaring states, the γ-ray emission dominates upon the emission at lower energies by a factor of 10.

The detection of VHE γ rays with ground-based telescopes from 3C 279 was unexpected: firstly, significant fluxes at VHE were disfavoured because the high energy peak of the spectral energy distribution is located at a few GeV; secondly, a strong absorption of VHE radiation by the EBL was expected due to the large redshift.

4.2.1 MAGIC observations

3C 279 was discovered at VHE by the MAGIC telescopes in 2006, during follow-up observations after high optical activity was measured[1] [29]. Successively, it was detected in 2007, again during observations triggered by an optical flare. It was observed later, from December 2008 to April 2009, after a high activity state had been reported by the *Fermi*-LAT, but no significant detection was found [37]. Despite 3C 279 being visible to all existing Cherenkov telescopes (Fig. 4.1), it has been detected only with MAGIC: due to the source large distance and its steep spectrum, the flux in the VHE band is low, requiring a good sensitivity in the lower part of this energy range ($\lesssim 200\,\mathrm{GeV}$).

2011 observations and data analysis

In 2011, 3C 279 was observed with the MAGIC telescopes as part of two different campaigns: from 8 February to 11 April (*Period-1*) for regular monitoring, and from 1 to 6 June (*Period-2*) after alerts of high activity states in the optical and *Fermi*-LAT energy ranges[2]. During *Period-1*, a total of 20 hours during 14 nights have been collected, and in *Period-2* 10 hours over 7 nights. After the quality

[1] Observations were triggered because the source had a flux in the optical band that exceeded the long-term baseline flux by a factor two.

[2] The triggering criteria in both energy ranges were fulfilled: in the optical R-band magnitude < 14.8 and *Fermi*-LAT flux $> 10^{-6}\,\mathrm{photons\,cm^{-2}s^{-1}}$.

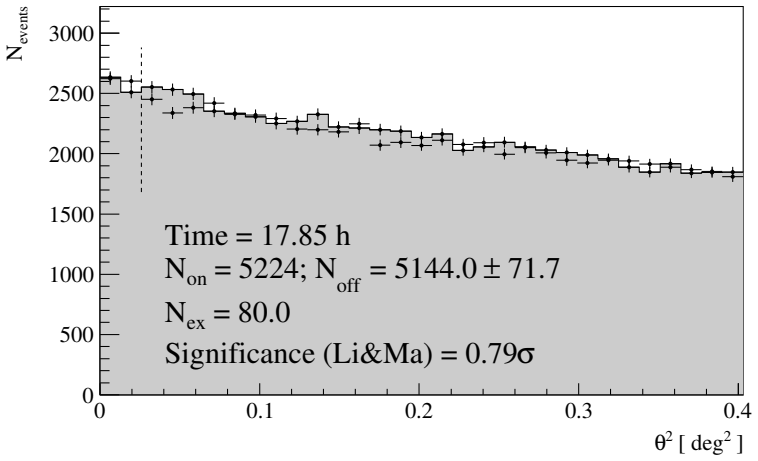

Figure 4.7: The significance distribution for 2011 observations of 3C 279. The distribution of the ϑ^2 parameter for ON-source events (black points) and OFF-source events (grey area) and the *signal* cut (dashed line) is shown. No significant detection was found. For more details see Tab. A.3

selection, 20.6 hours of data were left, corresponding to an effective time (corrected for readout dead-time) of 17.8 hours. The source was observed in wobble mode, with the standard settings (using two positions at 0.4° offset from the source and with a rotation angle of 180°). The zenith angle had medium-high values ranging from 35° to 45°. The analysis energy threshold is 125 GeV, higher than in previous analyses, not only because of the range of zenith angles but also because part of the observations were performed during moderate moonlight and twilight conditions.

For the signal search, an analysis optimised for low energies was performed, with the following cuts: $\vartheta^2 < 0.026$, *hadronness* < 0.28 and *size* > 55 photo-electrons. The resulting significance distributions for the two different periods and for the combined data set are shown in Fig. 4.7 and Fig. 4.8. In Tab. A.3, the number of excess events and significances for each night and for the different periods are reported.

Since no significant detection was found in any of the periods, upper limits on the flux were computed. Cuts for the flux calculation were determined requiring efficiencies of 70% and 90% for ϑ^2 and *hadronness* respectively, with minimum values $\vartheta^2 = 0.02$, *hadronness* $= 0.2$, and additional cuts *leakage* < 0.2, *number of islands* < 2 and *size* > 50 photo-electrons. Two energy bins were selected: $125-250$ GeV and $250-500$ GeV. The lower value is the energy threshold of this analysis, while energies higher than 500 GeV can be neglected because of EBL absorption (optical depth $\tau > 1$ for a source located at redshift $z \sim 0.5$ at 500 GeV [81]). The differential upper

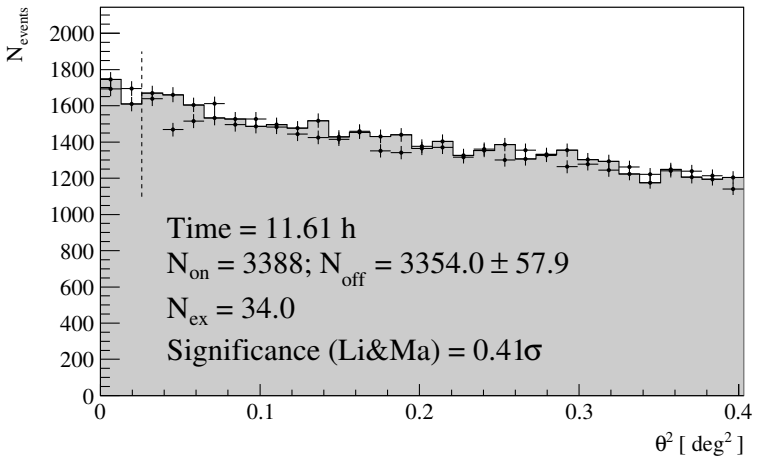

(a) *Period-1.*

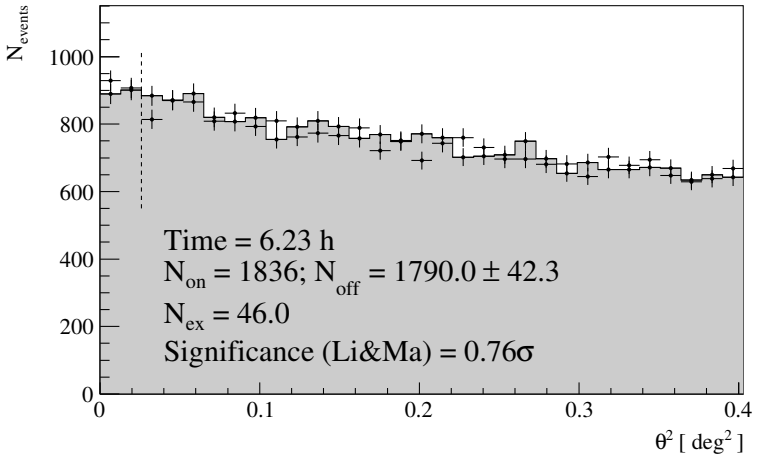

(b) *Period-2.*

Figure 4.8: The significance distributions for the two periods of 2011 observations of 3C 279. The distribution of the ϑ^2 parameter for ON-source events (black points) and OFF-source events (grey area) and the *signal* cut (dashed line) is shown. In none of the two periods a significant detection was found. For more details see Tab. A.3.

Period (effective time [h])	Energy threshold [GeV]	Integral Flux [10^{-11} cm^{-2}s^{-1}]
Period-1 (11.6)	125	<1.3
	150	<0.6
Period-2 (6.2)	125	<3.7
	150	<1.9
2009 (11.9)	150	<6.3

Table 4.2: MAGIC 2011 upper limits on the integral flux at Earth (without correction for EBL absorption) calculated above 125 GeV (energy threshold of the analysis) and above 150 GeV for comparison with 2009 upper limits [37].

limits on the flux were computed using the *Rolke* method, assuming a systematic error of 30% and a power law with a spectral index 3.5 (see Section 2.2.2).

The spectral index in Eq. 2.9 is not known a priori. In the literature, only one upper limit calculation for this source is available, where the index 4 was used [37]. During MAGIC detections of 3C 279, the values 4.1 (2006) and 3.1 (2007) were obtained. *Fermi*-LAT measured an average spectral index ~ 2.4 in the energy range $0.1 - 100$ GeV [107]. By extrapolating *Fermi*-LAT spectra to higher energies and considering the correction for EBL absorption, the value ~ 4.5 is obtained. Three values were tested in the calculation of the upper limits: 2.5, 3.5 and 4.5. Since the outcomes do not differ appreciably (Tab. A.5), the average value 3.5 was chosen.

The results are summarised and compared with historical observations of MAGIC in Tab. 4.2, Fig. 4.9 and Tab. A.4. Upper limits derived in this work are for the first time below the flux previously measured, confirming that previous detections caught the source during high activity states. 3C 279 is a highly variable source at VHE, and since its signal was detected during single nights only, the absence of a detection in 2011 does not exclude the possibility of a short flare taking place while we were not observing.

4.2.2 Multiwavelength behaviour in 2011

MAGIC observations were complemented with multiwavelength data in the energy range from *Fermi-LAT* γ rays to radio, and with polarisation measurements in the optical band [36], all reported in Fig. 4.10. In general, in *Period-1*, the source was in a low activity state in all measured wavebands, while a higher flux level was found in *Period-2*. Flux levels were still one order of magnitude smaller than the historical maxima. In the following, the behaviour in different bands will be described in detail.

In ***Fermi*-LAT band** the source was in a low activity state during *Period-1*, while later there were two flares. The maximum flux was $\sim 13 \times 10^{-7}$ cm^{-2} s^{-1}, roughly half the flux level of the outburst measured in February 2009 [107], which triggered MAGIC observations but did not yield a VHE detection [37]. The *Fermi*-LAT collaboration provided two spectra, simultaneous with MAGIC data. *Period-1* spectrum shows curvature, while the spectrum of *Period-2* is consistent with a power law function. When considering only the 2011 observations, no break has been found in the *Fermi*-LAT data, contrary to what was obtained by analysing the first two years of *Fermi*-LAT data (from August 2008 to August 2010). This is probably due to the short observation time available.

It is also interesting to compare the *Fermi*-LAT measurements with the upper limits obtained with MAGIC (Fig. 4.11). No features are found in the combined spectrum of *Period-1*, while in the one from *Period-2* there is a hint of a break between the energy ranges of the two experiments. This characteristic can be interpreted as the result of absorption of the most energetic photons by low energy radiation of the disk or of the broad line region. In this scenario, the emission of *Fermi*-LAT and MAGIC bands is generated in the same zone of the blazar, located in a region internal to the torus where low energy photons are found.

The **X-ray** light curve shows a trend similar to the one observed by *Fermi*-LAT: two subsequent flares, the first one being the most intense. The similarity of

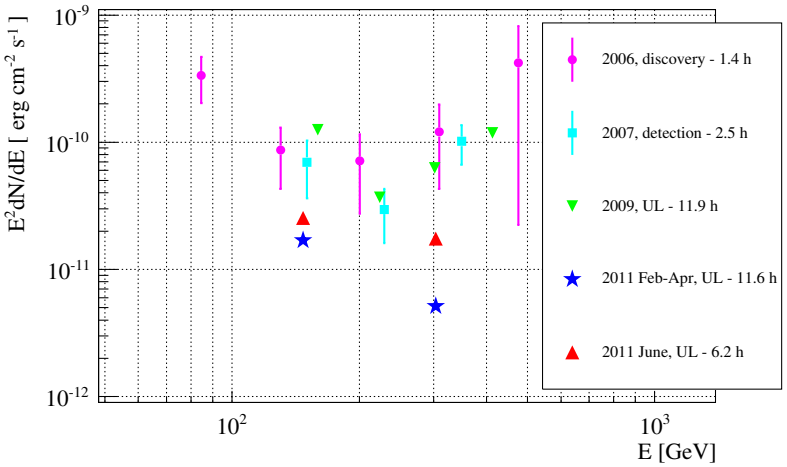

Figure 4.9: MAGIC upper limits (UL) calculated from two periods in 2011 (blue stars for *Period-1* upper limits, red up-going triangles for *Period-2* upper limits, [36]). Previous MAGIC-I results are also shown [37]: the 2006 discovery (cyan circles), 2007 detection (magenta squares) and the 2009 upper limits (green down-going triangles). All data are corrected for EBL absorption [81].

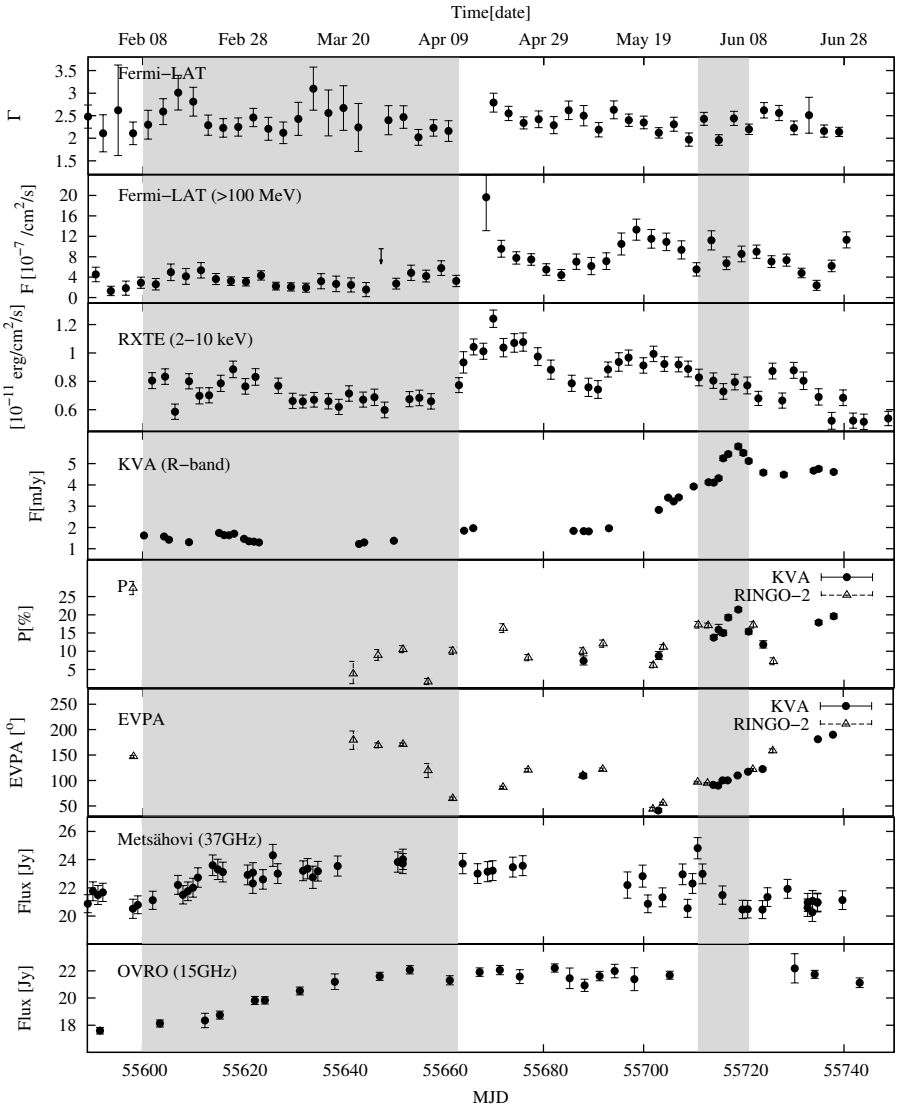

Figure 4.10: The multiwavelength light curve of 3C 279 measured in 2011 [36]. Starting from the upper panel: the *Fermi*-LAT spectral index and flux above 100 MeV, the X-ray flux measured by *RXTE*-PCA, the optical *R*-band by KVA telescope, the percentage of polarised flux (P) and the electron vector position angle (EVPA) in the optical band as measured by KVA (full circles) and RINGO-2 (empty triangles), the radio light curves of the Metshähovi and OVRO telescopes. The shaded areas indicate the two periods of MAGIC observations.

these two light curves suggests a common origin for the emission in these two energy ranges. The source was in a low activity state during spring 2011 with respect to the long-term X-ray behaviour of 3C 279 from 1996 to 2007 [67], but it has a maximum flux similar to the outburst happened during the 2009 *Fermi*-LAT flare [1].

In the **optical** band there was enhanced activity. A flare started at the end of April, reaching a maximum flux of ~ 6 mJy (magnitude $R \sim 14.3$) at the beginning of *Period-2*, during the descending phase of *Fermi*-LAT flare. The optical outburst is the third brightest one registered since the beginning of the KVA monitoring program in 2004. The two brightest optical flares took place in 2006 and 2007 in coincidence with the detections in VHE γ rays [37]. Simultaneously with the 2011 optical flare, the degree of polarisation was variable and a smooth rotation of the polarisation angle of $\sim 140^\circ$ took place.

At **radio** frequencies, there was no pronounced variability. However, the light curves at 37 GHz and 15 GHz have intervals where no data are available during flares at higher energies. VLBA observations[1] at 43 GHz, from January to December 2011, show that no new components were ejected from the radio core, and, contrarily to previous flaring episodes, neither an increase in the polarised flux nor a rotation of the polarisation angle appeared simultaneously with the optical outburst [36].

The main features of the multiwavelength behaviour during 2011 MAGIC observation and their possible interpretation are:

- in *Period-1* the source was in a low activity state in all studied energy ranges: no constraints on the location of the emission region;

- the combined *Fermi*-LAT and MAGIC spectrum for *Period-2* suggests the presence of a break caused by internal absorption: the emission at these energies is generated in a region of the blazar internal to the torus;

- the similarity of *Fermi*-LAT and X-ray light curves indicates that the emission in these two energy ranges is co-spatial;

- optical flare taking place during the descending phase of the *Fermi*-LAT flare: optical emission is not generated in the same region as the high energy emission (from VHE to X-rays);

- increase of polarised flux and rotation of polarisation vector in the optical band with no counterpart at radio frequencies: variability originates in a region external to the torus and the component responsible for the optical emission follows a trajectory with a bend of $\Psi \sim 10^\circ$ located at ~ 3 pc from the central engine [36];

[1] http://www.bu.edu/blazars/VLBAproject.html

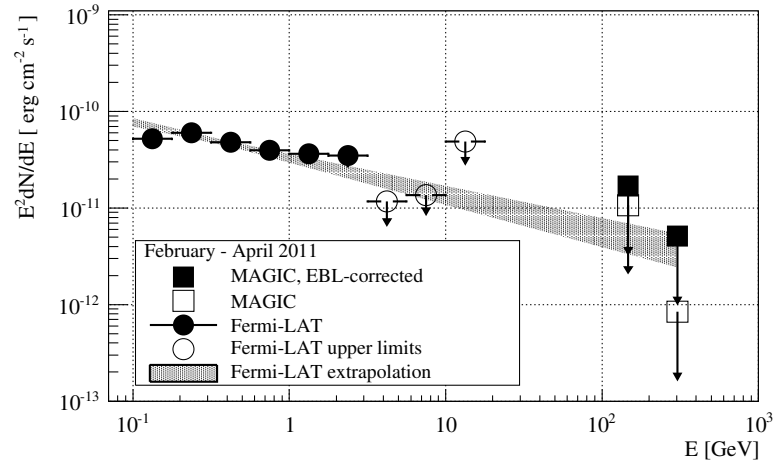

(a) *Period-1.*

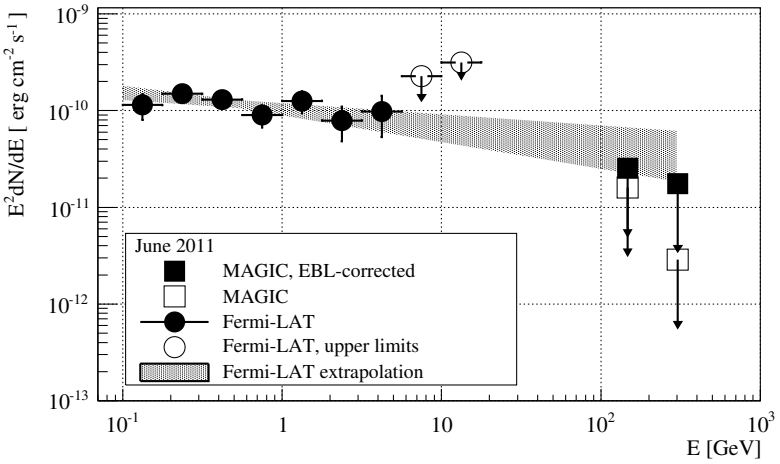

(b) *Period-2.*

Figure 4.11: MAGIC upper limits and *Fermi*-LAT spectra obtained for the two observation periods in 2011 [36]. The filled area represents the spectral energy distribution plot with a 1σ confidence region of the best-fit power-law model extended up to 300 GeV for *Fermi*-LAT observations (full circles, empty circles represent upper limits). The VHE data (empty squares) are corrected for EBL absorption (full squares, [81]).

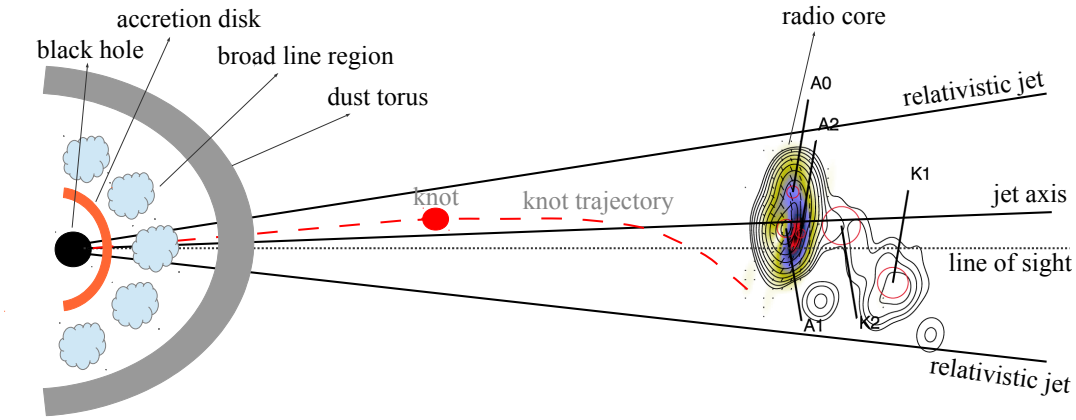

Figure 4.12: A sketch illustrating the structure of 3C 279. The black hole is surrounded by an accretion disk, gas clouds of the broad line region and a cold torus of dust and molecules. The radio core is located further down the relativistic jet. Here a VLBA image at 43 GHz from January 2012 has been inserted in the sketch [36]. In the model proposed for *Period-2* data [36], the X-ray to VHE emission originates in a region located within the broad line region and the optical emission far outside the torus. The emission knot follows a trajectory which suffers a bend at ~ 3 pc from the central engine.

- modest activity in the radio band with no ejection of new components: no connection between radio emission and activity in the optical band.

Given the different activity states shown during *Period-1* and *Period-2*, the two data sets need a different interpretation. The properties outlined above are shown in the sketch of the structure of 3C 279 (Fig. 4.12).

The multiwavelength spectral energy distributions of both periods have been fitted with leptonic models (see Section 3.3). The low energy peak is caused by synchrotron radiation from a population of relativistic electrons and the high energy peak is produced by inverse Compton scattering, the target being the synchrotron photons (SSC - synchrotron self-Compton) or ambient radiation (from broad line region or infra-red torus).

The low activity state of *Period-1* (Fig. 4.13) has been modelled using two different scenarios [36]:

1. the high energy emission is originating from a region located inside the broad line region (low energy photons of the broad line region are targets for inverse Compton scattering - Fig. 4.13a);

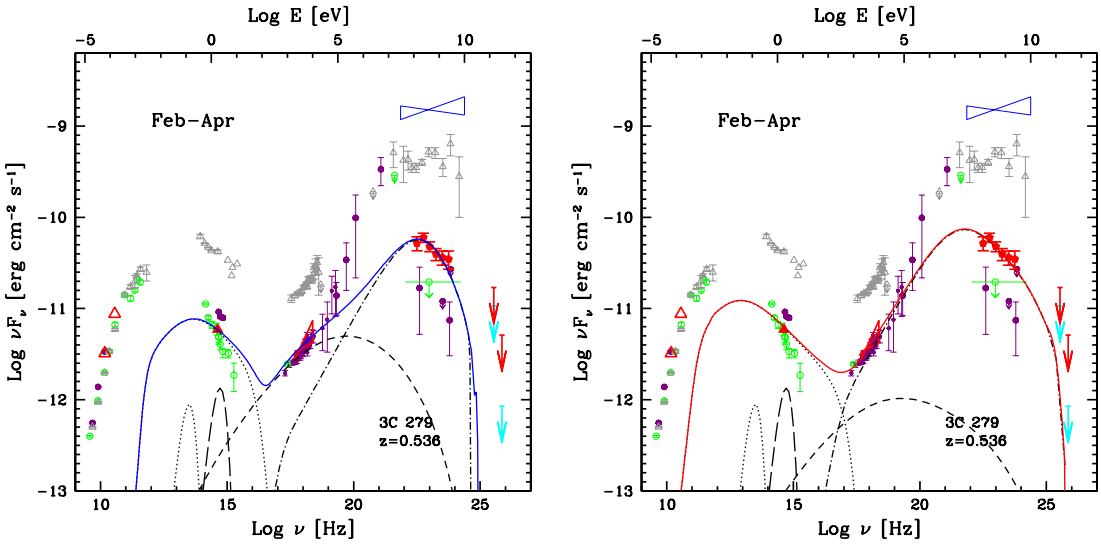

(a) Internal emission region. **(b)** External emission region.

Figure 4.13: Multiwavelength spectral energy distribution of 3C 279 for *Period-1* [36]: MAGIC (red arrows: EBL corrected, cyan arrows: observed points), γ rays from *Fermi*-LAT (red circles), X-ray from RXTE (red bow-tie), optical from KVA (red full triangles), and radio from Metsähovi and OVRO (red open triangles). Historical data are also shown [37]: the high activity state from 1991 (grey open triangles, [103]), the low activity state from 1993 (green open circles, [50, 135]), the high activity state from 1996 (blue bow-tie, [193]) and the low activity state from end of 1996 - beginning of 1997 (violet, [102]). Only points marked in red are considered for the spectral energy distribution fit.
Period-1 spectral energy distribution is fitted using two different one-zone leptonic models: (a) the high energy emission is originating from a region located inside the broad line region and low energy photons of the broad line region are targets for inverse Compton scattering (b) the high energy emission is coming from a region located outside the broad line region, considering as targets for inverse Compton scattering only photons from the infra-red torus. The individual components (synchrotron: dotted, synchrotron self-Compton: dashed, external Compton: dot-dashed) and the blackbody radiation from the broad line region (dashed) and from the infra-red torus (dotted) are also shown. The parameters are summarised in Tab. 4.3.

		γ_{min}	γ_b	γ_{max}	n_1	n_2	K [cm^{-3}]	B [G]	R [cm]	δ	Γ
Period-1	(a)	1	610	1.1×10^4	2	3.7	5.9×10^5	2.4	4.7×10^{15}	12.7	10
	(b)	2.5	600	8×10^4	2	3.6	3.2×10^3	0.3	1×10^{17}	15	12
Period-2 (two zones)	internal region	25	610	3×10^4	2	3.6	3.1×10^5	1.45	1.1×10^{16}	10	10
	external region	35	610	3×10^4	2	3.35	1.05×10^3	0.8	1.5×10^{17}	10	10

Table 4.3: Model parameters used for fitting the spectral energy distribution with different leptonic scenarios (Fig. 4.13 and Fig. 4.14) [36]. The accretion disk and the torus are characterised by $L_{disc} = 3 \times 10^{45}$ erg s^{-1}, $R_{BLR} = 1.7 \times 10^{17}$ cm, $L_{torus} = 2 \times 10^{45}$ erg s^{-1} and $R_{torus} = 2 \times 10^{18}$ cm. In columns three to seven the parameters describing the electron population are reported: the minimum, the break and the maximum Lorentz factors, the spectral indexes before and after the break and the electron density. In columns eight to twelve the properties of the emission region are listed: magnetic field, radius, Doppler factor and Lorentz factor.

2. the high energy emission is coming from a region located outside the broad line region (in this case target for inverse Compton scattering are photons from the infra-red torus - Fig. 4.13b).

In both scenarios the low energy peak is originated by synchrotron radiation, and radio spectral points are not used in the fit but are treated as upper limits, as the radio emission originates further out along the jet. The maximum size of a region to be synchrotron self-absorbed (see Section 1.4.2) at radio wavelengths [1] is:

$$5 \times 10^{16} \left(\frac{\nu F_\nu}{2 \times 10^{-11}\,\mathrm{erg\,cm^{-2}\,s^{-2}}} \right)^{1/2} \left(\frac{B}{0.3\,\mathrm{G}} \right)^{1/4} \left(\frac{\nu}{10^{11.5}\,\mathrm{Hz}} \right)^{-7/4} \left(\frac{\Gamma}{15} \right)^{-1/4} \mathrm{cm} \tag{4.1}$$

using magnetic field $B > 0.5\,\mathrm{G}$, Lorentz factor $\Gamma = 10$ [37] and the flux at the frequency $\nu = 15\,\mathrm{GHz}$ $F_\nu = 22\,Jy$ (this frequency was selected because is the smallest one in which no variability has been measured), we need R to be smaller than 10^{18} cm for the region to be optically thick at 15 GHz. The parameters obtained in the two different cases (Tab. 4.3) have values typical for this source, and with the information we have it is not possible to discriminate between the two scenarios.

Considering the constraints obtained from the multiwavelength analysis, a two-zone leptonic model has been applied to *Period-2* data (Fig. 4.14): the high energy emission is generated in a region inside the broad line region, while the low energy emission is synchrotron radiation coming from a region far outside the broad line region and the infra-red torus. Like for *Period-1* spectral energy distribution, the observed radio emission is coming from a region located further out along the jet. This model offers a satisfactory fit to the data with reasonable fit parameters (Tab. 4.3) for this source, and is in agreement with the bent-jet scenario (Fig. 4.12).

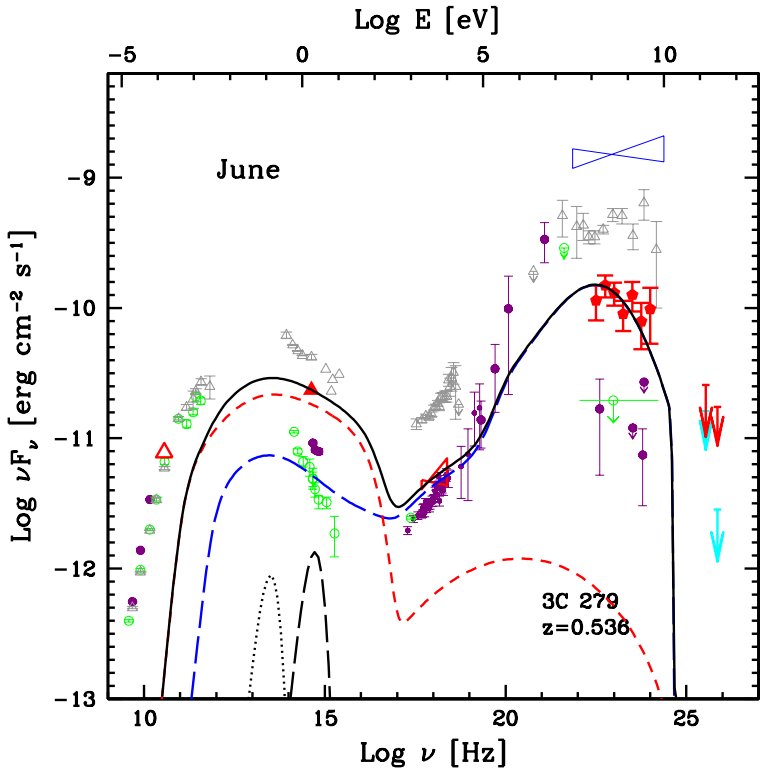

Figure 4.14: Multiwavelength spectral energy distribution of 3C 279 for *Period-2* [36]. See Fig. 4.13 for a description of the observations. A two-zone leptonic model has been applied to the data: the high energy emission is dominated by the region inside the broad line region (blue long-dashed line) while the low energy peak is synchrotron radiation from an external region (red short-dashed line), far outside the broad line region and the infra-red torus. The blackbody radiation from the broad line region (dashed) and from the infra-red torus (dotted) are also shown. The parameters are summarised in Tab. 4.3.

4.2.3 Results of 2011 observations

The results of MAGIC observations of 3C 279 in 2011 were presented: no significant detection was found, and the derived flux upper limits are below the flux measured during previous observations, confirming that 3C 279 is a highly variable source and all previous detections took place during its enhanced activity states.

Simultaneous data at lower energies were presented. The source was found in two different states: in *Period-1* it was in a quiescent state and the absence of activity in any of the observed wavebands does not allow us to constrain the location of the

emission region. The data of this period have been satisfactorily modelled with two different leptonic emission scenarios, but it was not possible to discriminate between them. Later, 3C 279 showed enhanced activity: similar flares in the *Fermi*-LAT and in the X-ray band, a flare in the optical band starting during the descending phase of a *Fermi*-LAT flare accompanied by a rotation of the optical polarisation angle and an increase in the percentage of optical polarised flux. These flares have been interpreted with a leptonic emission model in which the high energy emission is generated in a region inside the broad line region. The optical emission comes from a component located far outside the torus which follows a bent trajectory, supporting the hypothesis of the existence of a bend in the jet of 3C 279 [1, 150].

In Chapter 5 the behaviour and the interpretation outlined above are compared with previous studies of the source, focusing in particular on the absence of correlation between optical and high energy γ-ray emission and the lack of a VHE flare.

4.3 PKS 1510-089

The source PKS 1510-089 is a FSRQ located in the Libra constellation (RA: 228.2° DEC: −9.1°, see Fig. 4.1), at redshift $z = 0.361$ [64]. The broadband spectral energy distribution shows two peaks, the first one located between millimetre wavelengths and the infra-red band, and the second one ranging from soft X-rays to GeV γ rays and is more pronounced than the low energy one [109]. PKS 1510-089 has a curved radio jet[1], in which knots show apparent superluminal motion, reaching speeds as high as 46 c, the highest ever observed in blazars [113, 119]. The flux in the optical and radio bands is highly polarised [176]. Pronounced emission lines and an UV excess, due to the thermal emission from the accretion disk, have been observed [130, 177]. These are all typical features of FSRQs but, differently from other FSRQs, the UV excess is clearly visible also during high optical states. Other peculiar properties of PKS 1510-089 are the low power emitted and the low mass of black hole $5.4 \times 10^8\, M_\odot$ (black holes in other FSRQs have masses of $\sim 10^9\, M_\odot$). A possible explanation for these particular features is that PKS 1510-089 is an aged FSRQ [2].

The FSRQ PKS 1510-089 was discovered to emit high energy γ rays by the EGRET experiment, which measured a constant flux, without detecting any variability [104, 174, 184]. Recently, both the *Fermi*-LAT and AGILE experiments observed several flares and rapid outbursts, with time scales ranging from months to hours [2, 71–73, 153, 165]. These high activity states were accompanied by flares and

[1]Misalignment between the milliarcsecond and arcsecond scale has been observed, indicating that the jet is curved. The intrinsic bending of $12° - 14°$ is amplified through relativistic effects to the observed bending of 177° [114].

enhanced activity in various energy ranges, but with different behaviours each time. High energy γ rays are generally correlated with optical emission, but also γ-ray flares with no optical counterpart were observed and vice-versa. In a few cases, high energy γ rays flares were related to radio flares and emission of new radio components. During one of these high energy γ-ray flares PKS 1510-089 was discovered at VHE by the H.E.S.S. telescopes [109]. In detail, in March 2009 the source was in a high activity state showing pronounced variability both at high energies and in the optical band. The H.E.S.S. collaboration measured a flux above 150 GeV of $\sim 3\%$ of the Crab Nebula flux and a soft spectrum with index $\Gamma = (5.4 \pm 0.7_{stat} \pm 0.3_{sys})$. No variability was found, differently from the two other FSRQs known to emit at VHE, 3C 279 and PKS 1222+216, which have been detected only during single nights [29, 34, 37]. Enhanced activity states at high energies have been measured in February 2012 and March 2013, which both triggered MAGIC follow-up observations which resulted in significant detections of the source.

4.3.1 MAGIC observations

2012 observations

The source PKS 1510-089 was observed with the MAGIC telescopes from February to March 2012[1], after high activity states were measured by AGILE and *Fermi*-LAT experiments[2]. The source was observed during 28 nights, for a total of ∼25 hours of data which, after quality selection, correspond to an effective time of ~ 21.5 hours. The zenith angle ranges between 37° and 49°, and the observations were performed in wobble mode, using four positions at 0.4° from the source.

The analysis presented in this section was performed as a *cross-check analysis*: settings and cuts are different but the results are in agreement with the *main analysis* (for more details see Section 2.2). The plots reported in the following of this chapter, including multiwavelength light curves and spectral energy distribution, show the results of this *cross-check analysis*.

For the signal search, an analysis optimized for low energies was used with the following cuts (see Section 2.2.2): *image size* > 45 photo-electrons, *hadronness* < 0.5, $\vartheta^2 < 0.026$ and *number of islands* < 1.5. As shown in Fig. 4.15 and Tab. 4.4 the source is significantly detected only combining several nights of observations. A detection with a statistical significance of $5.8\,\sigma$ is found considering the entire data sample and of $5.3\,\sigma$ in *Period-A* (from 2 February to 6 March 2012), but neither during *Period-B* (from 15 March to 3 April 2012) nor during single nights significant

[1] During this observation campaign, the MAGIC telescopes were already equipped with the new readout system but the cameras of the two telescopes were different, since the camera of MAGIC-1 was replaced during summer 2012 (see section 2.2).

[2] Triggering criteria: flux at high energies $> 2 \times 10^{-6}$ photons cm^{-2}s^{-1}.

Date	Time [h]	N_{on} [counts]	N_{off} [counts]	N_{ex} [counts]	σ
all	21.46	8630	8017.3 ± 51.7	612.7 ± 106.3	5.83
Period-A	11.07	4055	3675.7 ± 35.0	379.3 ± 72.7	5.31
Period-B	10.40	4575	4341.7 ± 38.0	233.3 ±77.6	3.03

Table 4.4: Results of 2012 MAGIC observations of PKS 1510-089. Observation time, number of ON-events N_{on}, number of OFF-events N_{off}, number of excess-events N_{ex} and the statistical significance [126] are reported for the entire data sample and for the two observation periods. A significant detection was found in the entire data set and in *Period-A* data (from 2 February to 6 March 2012). In *Period-B* (from 15 March to 3 April 2012) no signal was found (for more details and single night significances see Tab. A.6).

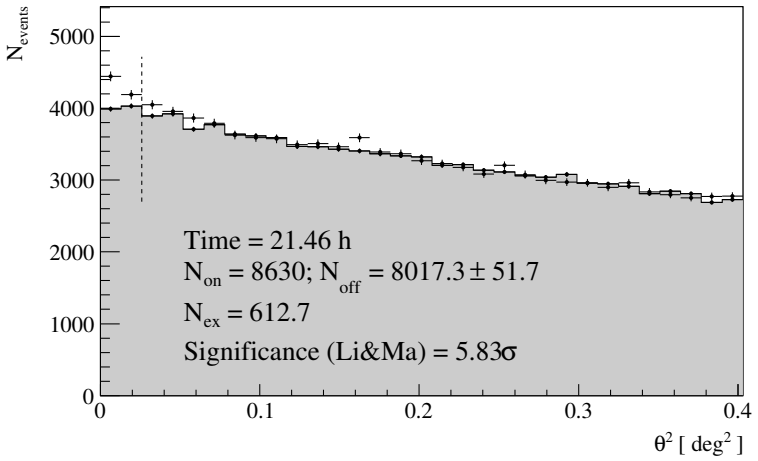

Figure 4.15: The significance distributions for 2012 observations of PKS 1510-089. The distribution of ϑ^2 parameter for ON-source events (black points) and OFF-source events (grey area) is shown. A detection with a statistical significance of $5.8\,\sigma$ was found (for more details see Tab. 4.4 and Tab. A.6).

signal was found (for more details see Tab. A.6).

Flux and light curve were obtained using 12 bins in azimuth, *size* > 50 photo-electrons, *leakage* < 0.2 and *number of islands* < 2. The cuts on *signal* and *hadronness* were determined requiring efficiencies of 70% and 95% respectively, with $\vartheta^2 > 0.02$ and *hadronness* > 0.25. The light curve was calculated in the energy range above 200 GeV, applying a cut $\vartheta^2 < 0.02$, using both weekly and nightly binning: no variability was detected in any of the time scales examined (Fig. 4.16). The

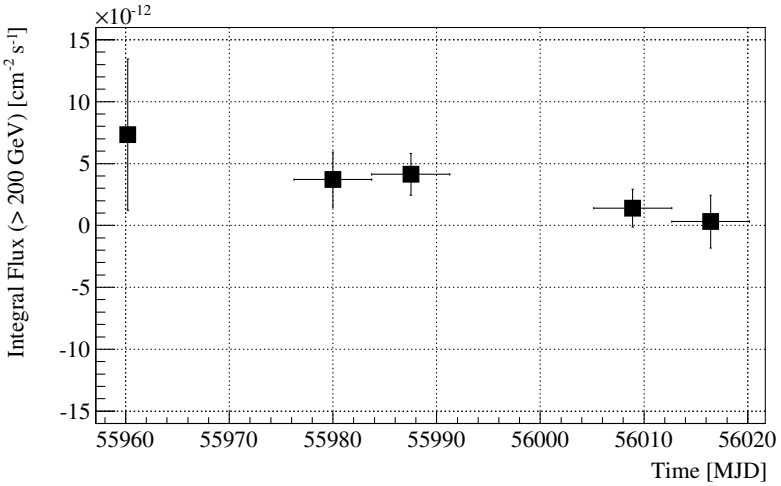

(a) Weekly binning.

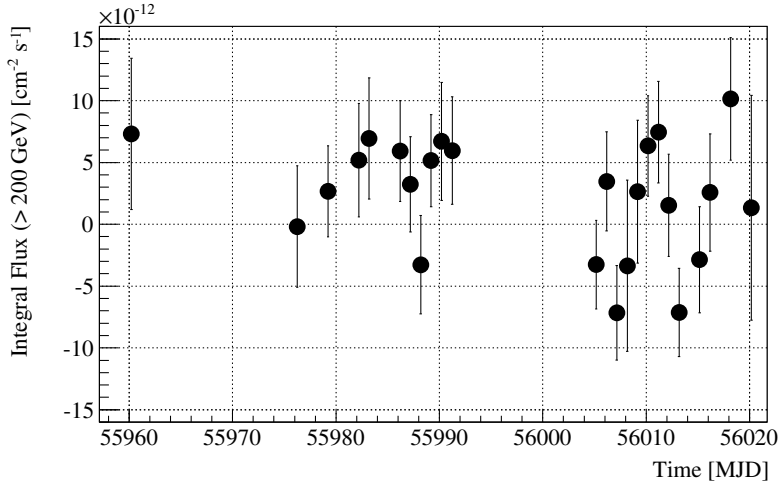

(b) Nightly binning.

Figure 4.16: PKS 1510-089 light curve obtained for 2012 observations, with (a) weekly and (b) nightly binning. No variability was found at any of the two time scales analysed.

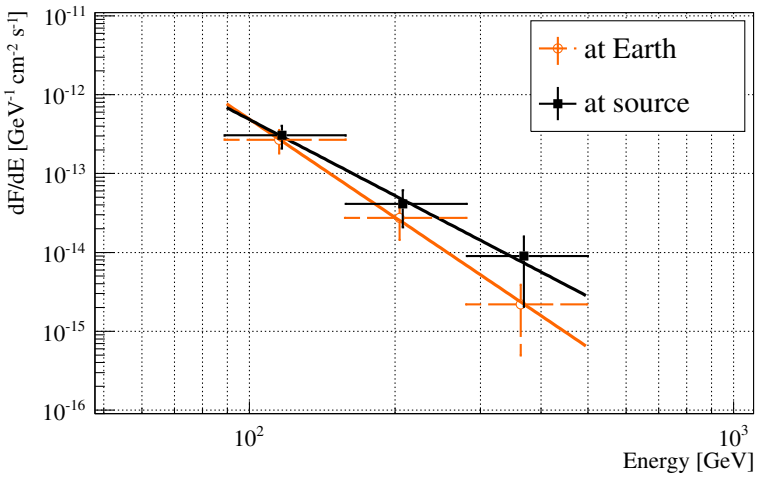

Figure 4.17: PKS 1510-089 spectra obtained from 2012 observations, observed (orange open circles) and intrinsic, corrected for the EBL absorption (black full squares, [81]). Both spectra are fitted with a power law function $dF/dE = F_0(E/200\,GeV)^{-\Gamma}$ whose parameters are $\Gamma = 4.1 \pm 0.7$, $F_0 = (2.8 \pm 0.7) \times 10^{-14}\,\mathrm{GeV^{-1}cm^{-2}s^{-1}}$ for the observed one and $\Gamma = 3.2 \pm 0.8$, $F_0 = (5.2 \pm 1.6) \times 10^{-14}\,\mathrm{GeV^{-1}cm^{-2}s^{-1}}$ for the intrinsic one.

spectrum was unfolded and corrected for EBL absorption (Fig. 4.17 and Tab. A.7). The spectra are fitted with a power law function, with reference energy 200 GeV and soft spectral indexes: 4.1 ± 0.7 (observed) and 3.2 ± 0.8 (intrinsic).

2013 observations

In March 2013, the MAGIC telescopes performed follow-up observations of a high activity state detected by *Fermi*-LAT[1]. PKS 1510-089 was observed during 30 nights, between 15 March and 5 June for an effective time of good quality data of ~ 17.4 hours. As for 2012 observations, four wobble positions were used and the source was observed at medium-high zenith angles (from $\sim 35°$ to $50°$). A difference between the two observation campaigns is that the MAGIC telescopes were in different configurations: 2012 observations took place in an intermediate phase of the upgrade (new readout only), while 2013 observations were performed once the upgrade was completed (new camera for MAGIC-1 installed). Due to the different hardware configurations, different analysis settings were applied in the two data sets (different Monte Carlo simulations and image cleaning were used; for details see Section 2.2).

The significance distribution shown in Fig. 4.18 was obtained applying a low

[1]The trigger criteria was that the flux above 100 MeV should exceed 10^{-6} photons $\mathrm{cm^{-2}s^{-1}}$.

Date	Time [h]	N_{on} [counts]	N_{off} [counts]	N_{ex} [counts]	σ
all	17.35	4492	4086.0 ± 36.9	406.0 ± 76.5	5.39
Period-A	6.04	1484	1389.0 ± 21.5	95.0 ± 44.1	2.18
Period-B	7.18	1927	1713.3 ± 23.9	213.7 ± 50.0	4.36
Period-C	4.13	1081	983.7 ± 18.1	97.3 ± 37.5	2.63

Table 4.5: Results of 2013 MAGIC observations of PKS 1510-089. Observation time, number of ON-events N_{on}, number of OFF-events N_{off}, number of excess-events N_{ex} and the statistical significance [126] are reported for the entire data sample and for the three observation periods: *Period-A* (from 15 to 25 March), *Period-B* (from 2 to 5 May) and *Period-C* (from 28 May to 4 June) which correspond to three different observation periods. A significant detection was found only considering the entire data sample (see Tab. A.8 for more details).

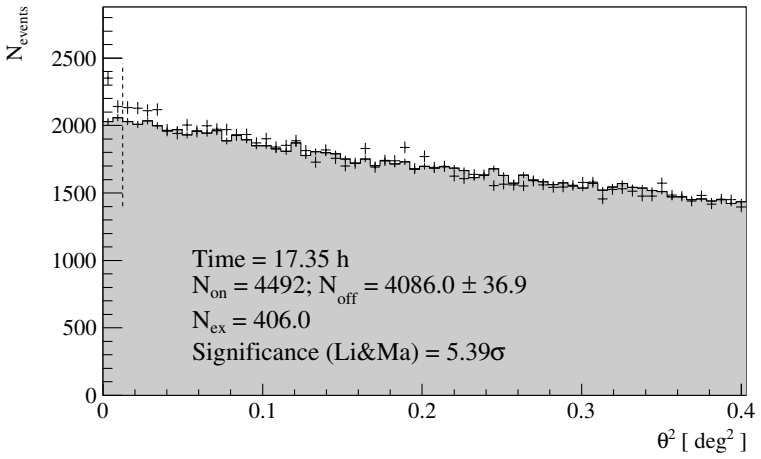

Figure 4.18: The significance distribution obtained from 2013 observations of PKS 1510-089. The distribution of ϑ^2 parameter for ON-source events (black points) and OFF-source events (grey area) is shown. An excess of 406.0 ± 76.5 events was found, corresponding to a detection of the source with a statistical significance of $5.4\,\sigma$ (see Tab. A.8 for more details).

energy analysis with cuts *hadronness* < 0.45, *image size* > 55 photo-electrons and *signal* < 0.0124 (the default *signal* cut for a low energy analysis is 0.02). A detection with statistical significance of $5.4\,\sigma$ was found, but neither during single nights nor considering the three different observation periods separately significant signal was found (Tab. 4.5, Tab. A.8).

The spectrum and light curve were computed using 28 bins in estimated energy in the range 5 GeV - 50 TeV, 12 bins in azimuth and *size* > 50 photo-electrons. Cuts on ϑ^2 and *hadronness* were determined setting efficiencies of 90% and 80% respectively, with $0.01 < \vartheta^2 < 0.2$ and $0.15 <$ *hadronness* < 0.95. The light curve was calculated for energies above 200 GeV, using two different time binnings: nightly binning and period-wise binning, with a bin for each observation period (*Period-A, Period-B, Period-C*), but no variability was detected at any time scale (Fig. 4.19). The spectrum, unfolded and corrected for EBL-absorption [81], is shown in Fig. 4.20. The spectral index is soft: observed $\Gamma = 4.2 \pm 0.7$, intrinsic $\Gamma = 3.3 \pm 0.7$. In Tab. A.9 the results obtained with different unfolding algorithms are compared.

The results obtained from MAGIC observations of PKS 1510-089 in the years 2012 and 2013 are in agreement with each other and with the results previously obtained by the H.E.S..S. telescopes in 2009 [109]: the source has a soft spectra and does not show variability at any studied time scale. The spectral energy distributions obtained during these three observation campaigns are compared in Fig. 4.21. In the following section, multiwavelength observations of 2012 will be presented.

4.3.2 Multiwavelength behaviour

MAGIC observation of PKS 1510-089 during 2012 were complemented with simultaneous multiwavelength data [35] in the following energy ranges: high energy γ rays, X-ray, optical polarimetric and polarised flux and radio. The light curves are shown in Fig. 4.22 and the multiwavelength spectral energy distribution in Fig. 4.24[1]. Between February and March, during the MAGIC observation period, three distinct high energy flares took place (marked with 1,2,3 in the third panel of Fig. 4.22), all characterized by different behaviour at lower energies. Simultaneously to the first high energy flare (1), there was a rotation of more than 180° of the optical polarisation angle, the ejection of a new radio knot and a radio flare. The second high energy flare (2) was accompanied by an optical flare and a rotation of more than 180° of the optical polarisation angle but in the opposite direction with respect to the previous one, and a radio flare. The third high energy flare (3) had instead only a counterpart in the optical polarisation angle: there was a rotation of more than 180° in the concordant direction of the first rotation. During the entire period, only

[1]The plots here reported show the results of the *cross-check analysis* and are in agreement with the published results [35].

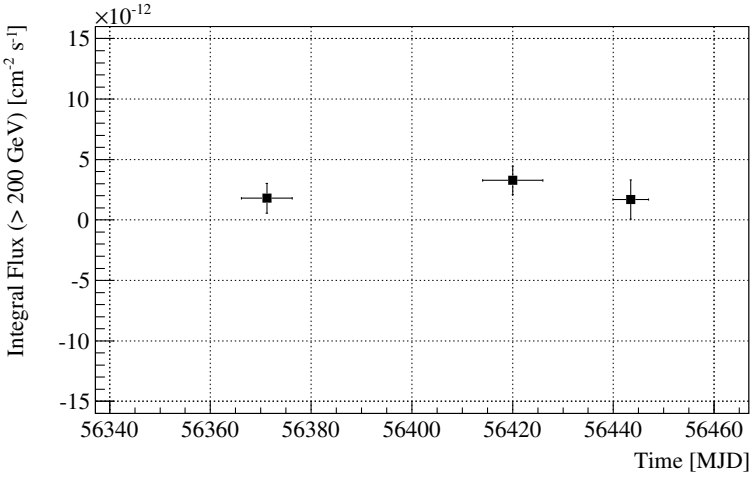

(a) Period-wise binning.

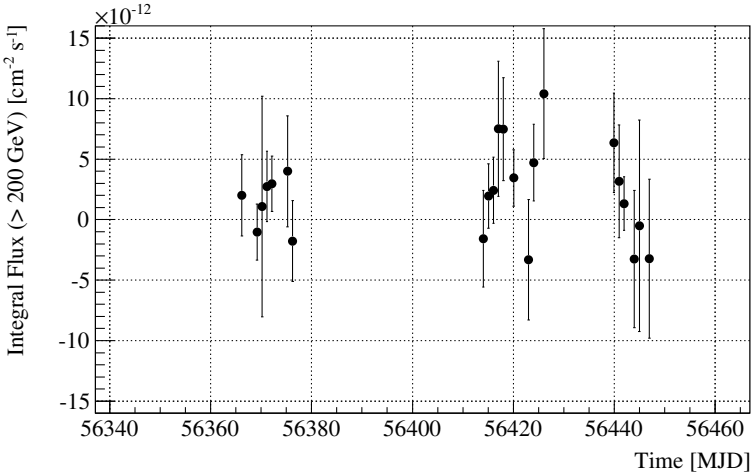

(b) Nightly binning.

Figure 4.19: The light curve obtained for 2013 observations of PKS 1510-089, with a (a) period-wise binning (a bin for each observation period) and (b) nightly binning. As for 2012 observations, no variability was found.

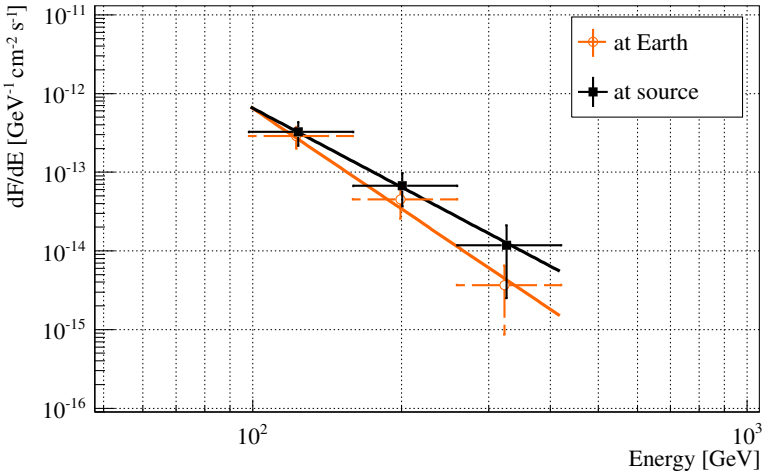

Figure 4.20: PKS 1510-089 spectra obtained from 2013 observations, observed (orange open circles) and intrinsic, corrected for the EBL absorption (black full squares, [81]). Both spectra are fitted with a power law function $dF/dE = F_0(E/200\,GeV)^{-\Gamma}$ whose parameters are $\Gamma = 4.2 \pm 0.7$, $F_0 = (3.4 \pm 1.1) \times 10^{-14}\,\mathrm{GeV}^{-1}\mathrm{cm}^{-2}\mathrm{s}^{-1}$ for the observed one and $\Gamma = 3.3 \pm 0.7$, $F_0 = (6.5 \pm 2.1) \times 10^{-14}\,\mathrm{GeV}^{-1}\mathrm{cm}^{-2}\mathrm{s}^{-1}$ for the intrinsic one.

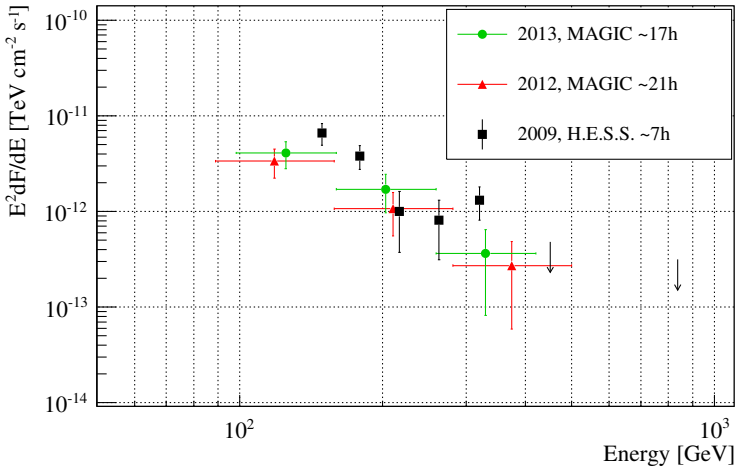

Figure 4.21: The spectral energy distribution for PKS 1510-089 measured by MAGIC in 2013 (green circles) and 2012 (red triangles - this analysis) and by H.E.S.S. telescopes (black squares [109]), at Earth. The three different measurements are in agreement with each other.

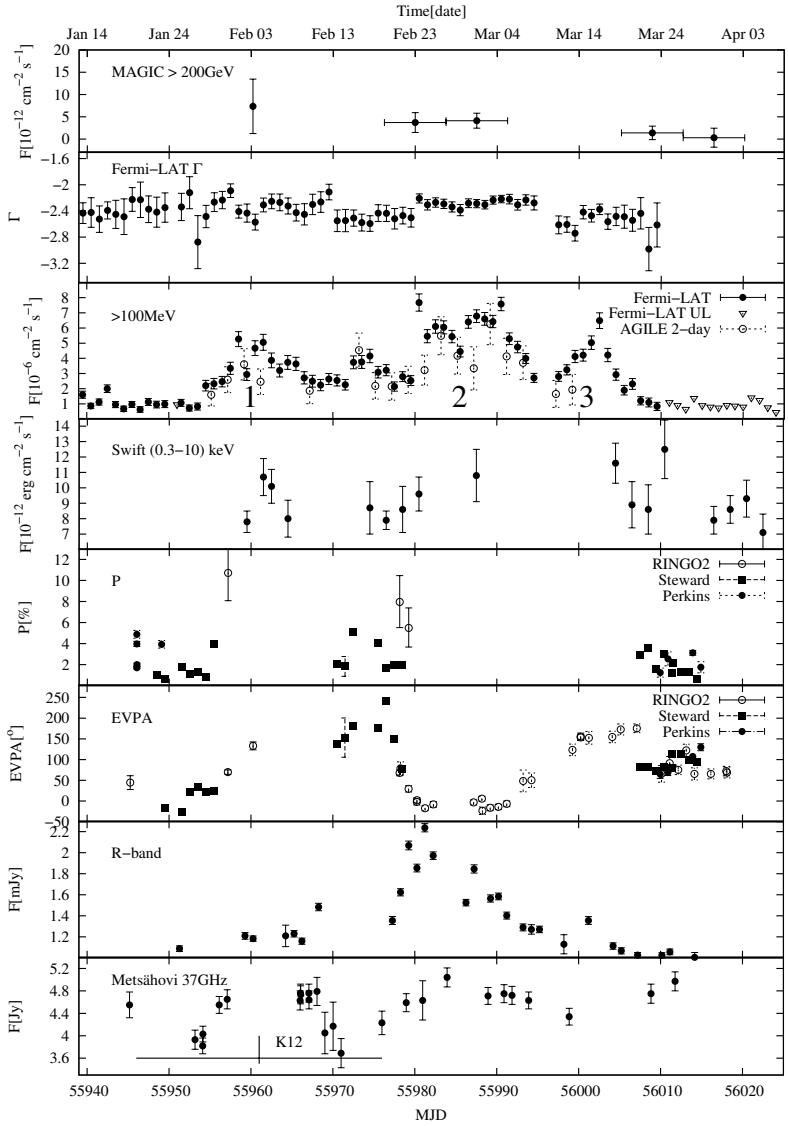

Figure 4.22: The multiwavelength light curve of PKS 1510-089 measured in 2012 [35]. Starting from above, are shown: MAGIC observations above 200 GeV (this analysis), spectral index measured by *Fermi*-LAT, high energy observations above 100 MeV by *Fermi*-LAT and AGILE experiments, X-ray flux from *Swift*. Panels five to seven relate to the optical emission: percentage of polarised flux (P), polarisation angle (EVPA) and photometric flux in the *R* band measured by the KVA telescope. The lowermost panel shows the radio flux at 37 GHz as measured by Metsähovi and the ejection of a new radio component observed by VLBA is marked (K12). In the third panel, the three high energy flares are marked (1, 2, 3).

	γ_{min}	γ_{break}	γ_{max}	n_1	n_2	$K\,[\mathrm{cm}]^{-3}$	$B\,[\mathrm{G}]$	$R\,[\mathrm{cm}]$	Γ
infra-red torus	3	9×10^2	6.5×10^4	1.9	3.85	20	0.12	3×10^{17}	20
sheat	8×10^2	7×10^3	5×10^4	2	3.4	18	1.3×10^{-2}	6×10^{18}	2.2
spine	8×10^2	2.6×10^3	8×10^4	2	3.7	2.5	6.5×10^{-3}	5.1×10^{18}	20

Table 4.6: Model parameters used for fitting the spectral energy distribution with different leptonic scenarios: "infra-red torus" refers to the scenario in which the emission region is located in an inner region of the blazar and target low energy photons are provided by the infra-red torus (Fig. 4.24a). "Sheat" and "spine" refer to the emission region located at the radio core where low energy photons are coming from a slow outer layer of the jet, called sheat, which surrounds the emission region, called spine (Fig. 4.24b). In columns two to seven the parameters describing the electron population are reported: the minimum, the break and the maximum Lorentz factors, the spectral indexes before and after the break and the electron density. In columns eight to ten the properties of the emission region are listed: magnetic field, radius and Lorentz factor.

moderate activity in the X-ray band was measured.

The high and very high energy spectra connect smoothly indicating [35]:

- a common origin of their emission;
- a negligible amount of internal absorption, suggesting that the emission region responsible for the high energy and very high energy radiation has a low density of low energy photons, condition met in the regions of the blazar external to the torus (see Fig. 4.23).

The simultaneity of the first flare at high energies, flaring activity in the radio and emission of a new radio knot suggest that the emission of these two energy bands took place in the same region, located at the radio core, and that the flare is caused by the emission feature passing through the core. A possible interpretation of the three different flares observed at high energies is the scenario already proposed for an earlier flaring episode of the source PKS 1510-089 [139]: a knot is propagating along the jet and when it crosses the radio core the first flare occurs. The second flare is caused by a sudden energization of the electrons in the knot and the third flare by an increase in the local seed photon field.

The spectral energy has been fitted with two different leptonic scenarios (Fig. 4.24, Tab. 4.6):

- the emission zone is located in an inner region of the blazar, and the low energy photons target for the inverse Compton scattering are coming from the infra-red torus (Fig. 4.24a);

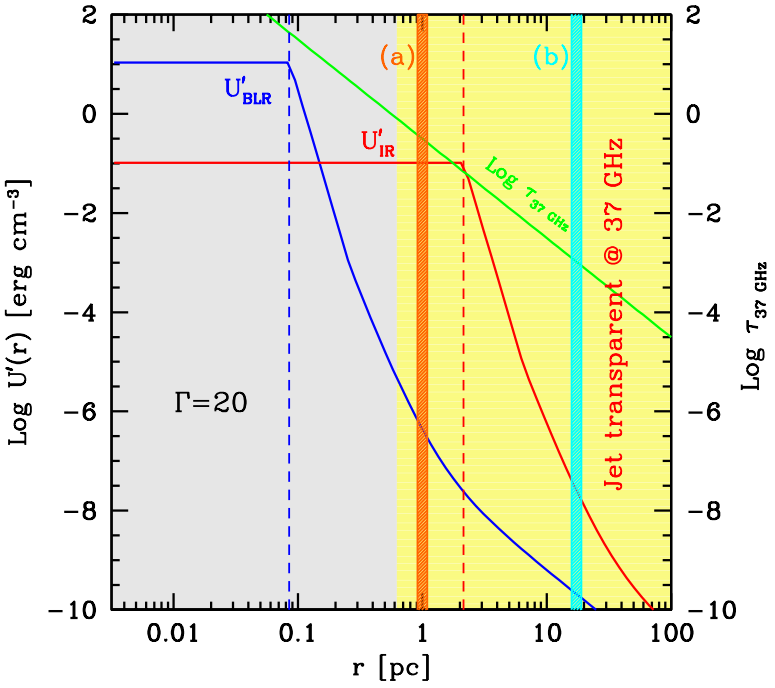

Figure 4.23: Energy density of the photon field as function of the distance from the central engine. The blue lines refer to the broad line region and the red lines to infra-red torus, whose size is indicated with the dashed lines. The yellow zone indicates the area at which the jet is transparent at the radio frequency 37 GHz. The thick vertical lines indicate the regions selected for the modelling of the spectral energy distribution. The orange line corresponds to an emission region in an inner part of the blazar and the low energy photons target for the inverse Compton scattering are coming from the infra-red torus (Fig. 4.24a). The cyan thick line indicates an emission zone located close to the radio core. Here the energy density of photons is too low for being a relevant target field for inverse Compton process and the low energy photons are assumed to come from a slow layer, called sheat, surrounding the jet (Fig. 4.24b). [35]

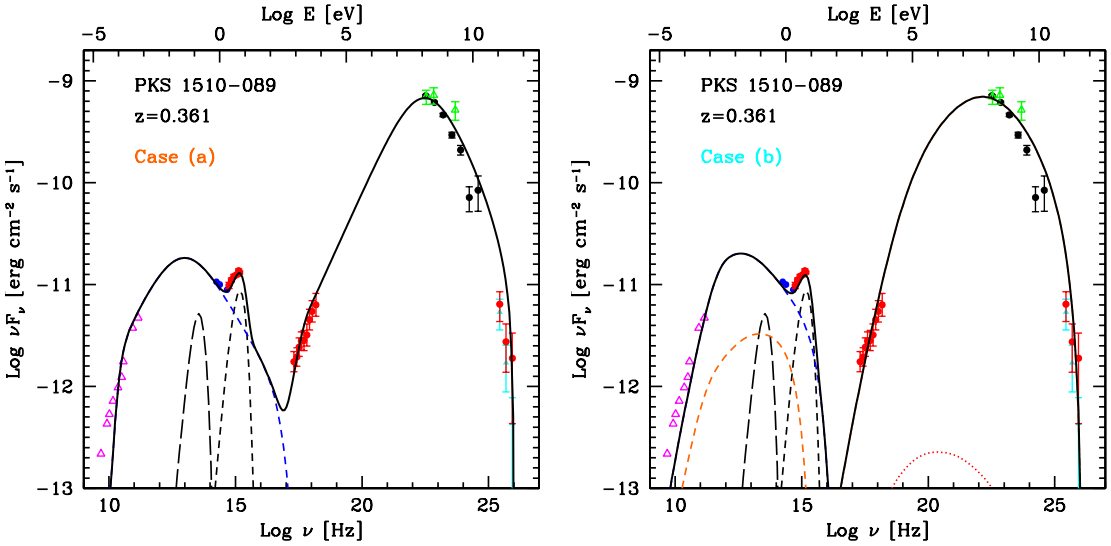

(a) Low energy photons: torus.

(b) Low energy photons: slow sheat.

Figure 4.24: The multiwavelength spectral energy distribution of PKS 1510-089 measured in 2012 [35]: radio from F-GAMMA and Metsähovi (magenta triangles), infra-red from GASP-WEBT (blue filled circles), optical-UV from *Swift*-UVOT and X-ray from *Swift*-XRT (red filled circles), high energy from AGILE-GRID (green open triangles) and from *Fermi*-LAT (black filled circles), MAGIC (this analysis) observed (cyan filled triangles) and corrected for EBL absorption (red filled dots, [81]). The model used to fit the data is a one-zone leptonic model, considering two different locations for the emission region. In (a) the emission region is located in an inner region of the blazar and the low energy photons target for the inverse Compton scarring are coming from the infra-red torus (long dashed line). In (b) the emission zone is located close to the radio core and the low energy photons are coming from a slow sheat surrounding the jet (orange dashed line). The synchrotron self-Compton emission is also shown (red dotted line). In both scenarios, the broad line region emission (black short dashed line) and the infra-red torus emission (black long dashed line) are shown. The parameters are summarised in Tab. 4.6.

- the emission originates in a region located further down the jet, at the radio core. At such a distance from the central engine, the energy density of photons is too low to be a relevant target for the inverse Compton scattering (Fig. 4.23). Low energy photons are coming from a slow outer layer of the jet, called sheat, which surrounds the emission region, called spine (Fig. 4.24b).

Both scenarios fit the spectral energy distribution, the second one being also consistent with the interpretation suggested by the multiwavelength light curve and the points mentioned above.

4.3.3 Summary of results of 2012 and 2013 observations

The results obtained during different observation campaigns at VHE on PKS 1510-089 show that the source has a soft spectrum and a constant flux. The other two FSRQs known at VHE, 3C 279 and PKS 1222+216, showed pronounced variability within single nights, with flux doubling time of $\sim$ 10 minutes in the case of PKS 1222+216 [34, 37]. For this reason, a VHE constant flux is an unusual characteristic for a FSRQ. The absence of variability at VHE can be simply caused by experimental reasons: short flares took place without being detected because of poor sensitivity or due to unlucky observations timing. However, in the case of PKS 1510-089, no variability was detected in any of the three observations campaigns at VHE suggesting that it is an intrinsic property of the source.

The multiwavelength behaviour observed in 2012 has been interpreted with a one zone leptonic model, considering two different populations of low energy photons. In one case, the emission region is located in an inner region of the blazar and target photons for the inverse Compton process are the infra-red photons of the dusty torus. In the other case, the emission region is located at the radio core and low energy photons are coming from a sheat surrounding the jet. Both models fit reasonably well the spectral energy distribution, but the latter model is favoured because it takes into account the constraints obtained from the light curve and in particular the co-spatiality of radio and γ ray emission. However, two-zones leptonic models were proposed to explain the data collected during other observation campaigns of PKS 1510-089 [51, 62, 151]. Since distinct models are able to reproduce different observations, it is very likely that several regions contribute to the overall emission of the source and that flaring episodes can be caused by activity in various zones of the blazar, eventually with one or more regions dominating over the other ones.

4.4 Conclusions

In this chapter the results of MAGIC observations of three blazars, 1ES 1727+502, 3C 279 and PKS 1510-089 have been presented. MAGIC observations and mul-

tiwavelength data of 1ES 1727+502, 3C 279 and PKS 1510-089 during 2012 are presented in dedicated papers [31, 35, 36], while the collection of multiwavelength data and the interpretation of 2013 observations of PKS 1510-089 is currently ongoing. I contributed to these studies analysing the data of the MAGIC telescopes; the multiwavelength data and the spectral energy distribution were provided by collaborators.

The BL Lac 1ES 1727+502 was selected for MAGIC observations from an X-ray catalogue [69] and was detected for the first time at VHE. The MAGIC observations were complemented with multiwavelength data, confirming that 1ES 1727+502 is a typical representative of the subclass of high synchrotron-peaked sources.

Different is the case of the two FSRQs 3C 279 and PKS 1510-089. They are both known VHE emitters, but they show a behaviour which is different not only from other sources of this class but also during distinct flaring episodes of the same source. The source 3C 279 was not significantly detected at VHE, despite the multiwavelength behaviour during MAGIC observations of 2011 was similar to the one observed during the two previous detections of the source. PKS 1510-089 was significantly detected during both observation periods, but without showing any variability, in contrast to what observed in the other two sources belonging to this class, 3C 279 and PKS 1222+216.

The data presented in this chapter indicate that FSRQs are complex objects and the origin of their VHE emission is still an open question. In order to shed some light on this issue, a combined experimental-theoretical effort is necessary. On the one side more observations of FSRQs (known and new sources) would help to precisely identify the properties of these objects and establish correlations among different energy ranges with greater detail. On the other side, models which reproduce not only the spectral energy distribution but also the temporal evolution of the emission would indicate strategies for new observations and questions to be answered by current and future experiments.

5

Summary

5.1 BL Lacertae objects

Sources of BL Lac type are easy targets for observations with imaging Cherenkov telescopes, mainly because of their hard spectra measured in *Fermi*-LAT band. Indeed, BL Lacs are the vast majority of extragalactic objects known at VHE.

The object 1ES 1727+502 is a newly discovered VHE emitter. It is a typical representative of the BL Lac class of blazar: the low energy peak dominates the spectral energy distribution and at high energies it has a hard spectrum. Its multiwavelength behaviour is reproduced with a one-zone synchrotron self-Compton model with values of the fit parameters typical for this class of sources [181].

The BL Lac 1ES 1727+502 was selected for observations from an X-ray catalogue and its discovery shows the importance of combining various criteria for selecting targets for VHE observations. With observations performed independently from the activity states of other bands it is possible to observe quiescent states. These results, complemented with the ones obtained from follow-up observations of flaring states, provide us valuable information for understanding more deeply this class of objects.

5.2 Flat spectrum radio quasars

Completely different is the case of FSRQs. Objects belonging to this class are not easy to detect with currently operational Cherenkov telescopes mainly for two reasons:

- they have lower fluxes than BL Lacs: the second peak of the spectral energy distribution is located at lower energies, they have a soft spectrum with cut-off between $1 - 10$ GeV as shown by *Fermi*-LAT observations;

- they are located at large redshift.

Indeed, we count only three representatives of this class at VHE: 3C 279, PKS 1510-089 and PKS 1222+216. As indicated by the analysis presented in Chapter 4, these objects are very interesting because they show a rich and complex behaviour, with enormous flux variations and short term variability, difficult to be explained with current emission models.

5.2.1 The case of 3C 279

The FSRQ 3C 279 showed a complex behaviour since it was first observed in γ rays with the EGRET experiment. Simple synchrotron self-Compton model could not reproduce the observed emission, but an additional component resulting from inverse Compton of external low energy photons was required [102] (external Compton models). The situation became even more problematic when VHE γ-ray data became available. MAGIC observed 3C 279 over several years, detecting it only twice [29, 36, 37]. Different emission models have been taken into account: diverse scenarios have been proposed not only for distinct flaring episodes but also for the same observation campaign. In detail, the multiwavelength properties measured at the time of MAGIC observations together with the proposed interpretations are summarised below.

- **2006**:

  - **observations**: 3C 279 was discovered as a VHE emitter (significant signal was measured during one night). MAGIC observations were triggered by a high activity state in the optical band; the source was in a high state also at X-rays while in the radio band there was only modest variability and no radio knot was emitted;

  - **interpretation:** One zone leptonic models considering synchrotron self-Compton and inverse Compton on the radiation field of the broad line region and the infra-red torus have been proposed [37]. Because of the reduced efficiency of the inverse Compton scattering at higher energies (caused by the Klein-Nishina suppression and photon-photon internal absorption), large flux levels in the band 100 MeV to 100 GeV (at the time of this campaign the *Fermi*-LAT was not operational) are required to reproduce the observed VHE emission.

The interpretation with an external Compton model has been criticised because there is no equipartition between the radiation and magnetic field energy densities[1] and more complicated scenarios have been proposed [59]. In detail, a leptonic multi-zone scenario, where the emission from the X-ray band to VHE γ rays and the optical emission are originated into two different regions of the blazar, could reproduce the observed behaviour. Also two different hadronic scenarios have been taken into consideration: a pure synchrotron-proton blazar model [147, 148], and a scenario considering also external photons as targets for photo-meson interactions. They both fit the spectral energy distribution, but the scenario with external photons is preferred because it can reproduce also short term variability, while in the pure proton-synchrotron model the cooling times are of the order of years.

- **2007**:
  - **observations**: 3C 279 was detected by MAGIC, once again only during a single night. High activity was reported in the optical, X-ray and radio bands, a new knot emerged in the radio band and rotations of both the optical and radio polarisation angles were measured.
  - **interpretation**: a two-zone leptonic model and a hadronic scenario have been proposed [37]. In the leptonic case, since the activity at VHE γ rays followed the one in the optical band, it is assumed that the optical, X-ray and high energy ($< 100\,\mathrm{GeV}$) emission comes from a region located within the broad line region, while the VHE emission is generated outside the broad line region (but within the infra-red torus). In this scenario, since the photons from the torus have lower energies with respect to the ones of the broad line region, the effects of Klein-Nishina and photon-photon absorption are minimised. A hadronic model, with synchrotron radiation emitted by protons, photo-meson interactions and further cascading, has been proposed, even being not in equipartition regime (see previous note on equipartition).
- **2009**:
  - **observations**: 3C 279 was observed with the MAGIC telescope, but no significant signal was measured. The observations were triggered by an alert of high activity state by *Fermi*-LAT, but at the time of MAGIC

[1] It is not clear if equipartition between the radiation and magnetic field energy densities is always required. Flares can result from rapid and abrupt changes in which there could be no time for reaching an equilibrium as in the case of equipartition.

observations the *Fermi*-LAT flux was already decreased. In the optical band the source was in an enhanced state but with no flares and a rotation of the polarisation angle was measured. The X-ray flux was low.

- **interpretation:** a leptonic model with synchrotron self-Compton and inverse Compton on photons of the broad line region reproduces the multiwavelength spectral energy distribution [37].

- **2011**, *Period-1* (February - April):
  - **observations**: monitoring observations at VHE in which no significant detection was found; the source was quiescent in all observed wavelengths;
  - **interpretation**: the low state is described with a single zone leptonic model with external Compton radiation. Two different scenarios are considered, both reproducing the spectral energy distribution. In one case the low energy photons target for inverse Compton scattering are the broad line region photons while in the other case they are coming from the infra-red torus [36].

- **2011**, *Period-2* (June):
  - **observations**: no detection at VHE, observations triggered by high activity states in *Fermi*-LAT energy range and optical band, rotation of the optical polarisation angle, modest flux variability in the radio band. Neither a new knot was emitted, nor a change in the radio polarised flux was measured.
  - **interpretation**: a two zone leptonic model can reproduce the observations [36]. The emission from X-ray to VHE γ rays is generated in a region internal to the broad line region while the optical emission comes from a zone located at the radio core.

From this description it is evident that interpretation of VHE flares of 3C 279 is challenging. It is possible that the baseline emission of 3C 279 has a leptonic origin[1] while for reproducing high activity states more complicated scenarios are required, as multi-zone leptonic models and hadronic models. Flares can be generated by perturbations of various nature originating in different regions of the blazar. It has been shown that in leptonic scenario perturbations in the magnetic field, fluctuations in the injection of particles or changes in the acceleration time scale (assuming Fermi II mechanism) cause different variability patterns [79]. Hadronic models predict a rich temporal behaviour as well. Two different populations of particles are present:

[1]Hadronic models fail in representing the long term average state of this FSRQ because they do not reproduce the spectral break measured by *Fermi*-LAT [60].

electrons and protons. They not only undergo different cooling processes with diverse loss time scales, but also have different acceleration time scales. Therefore, it is possible that electrons and protons burst in different periods. In addition, small perturbations can lead to regimes with very different properties [80].

The need for a time dependent model in which both hadronic and leptonic processes are taken into consideration is evident. If on the one hand more data are required to determine unambiguously correlations and relations among different wavelengths and constrain models, on the other hand models are needed for elaborating a successful strategy for observations maximising the chances of catching flaring states. For example, the relation between optical and VHE emission should be further investigated. Correlation between the optical band and γ rays is a general characteristic of FSRQs [2, 5] and it has been observed in several cases in 3C 279 (more recently by [107]). However, EGRET observations already revealed a complex behaviour for 3C 279, with appearing and disappearing correlations between these two energy ranges [100], trend confirmed by the long-term behaviour of the source [67]. Moving to higher energies, all VHE γ-ray observations which led to the detection of 3C 279 were triggered by high activity states in the optical band, indicating a connection between the optical and the VHE emission. Despite the optical triggers, models in which the optical and VHE emission is not related or is originated in two different regions of the blazar have been proposed (multi-zone leptonic models and hadronic models). Moreover, the source has been observed by the MAGIC telescopes without being detected when it was in high activity states both in the optical and in the *Fermi*-LAT band (2011 observations). It should be further investigated if follow-up observations from optical triggers are a good strategy for catching flaring states of the source or if this criterion should be combined with others. An answer to this question is possible only with a study using an emission model which reproduces also the temporal evolution.

5.2.2 The case of PKS 1510-089

The FSRQ PKS 1510-089 was observed at VHE by the H.E.S.S. and MAGIC telescopes which reported similar properties: soft spectrum and no variability. The first property is a general feature of FSRQs, while the absence of short term variability is a peculiar characteristic of this source (the two other FSRQs known at VHE γ rays, 3C 279 and PKS 1222+216, have been detected only during single nights). Different emission models have been proposed for the two multiwavelength campaigns:

- **H.E.S.S., 2009**: a two-zone leptonic model reproduces the observations. The emission up to GeV energies is external Compton with photons of the broad line region while VHE emission is external Compton from photons of the infrared torus [51];

- **MAGIC, 2012**: two different leptonic scenarios have been proposed, both with a single emission zone [35]. In one case the emission region is generated in an internal zone of the blazar. In this scenario target photons for external Compton are infra-red torus photons. In the other one, the emission region is located close to the radio core and low energy seed photons are coming from a slow sheat surrounding the jet. Both scenarios can fit the spectral energy distribution, but the latter is preferred because it takes into account constraints obtained from the multiwavelength light curve.

The necessity for two emission regions has been pointed out also by a study of the low state emission [151] and by properties measured by *Fermi*-LAT [62].

An interesting characteristic of PKS 1510-089 is the correlation between radio and γ-ray emission. According to the standard interpretation of FSRQs, high energy γ rays are produced in an inner region of the blazar, within the broad line region and the infra-red torus. This interpretation is supported by the presence of a break in *Fermi*-LAT spectrum [157]. However, correlations between γ-ray and radio emission have been observed, and in some cases new radio knots emerged simultaneously with γ-ray flares. Consequently, models located the γ ray emission region at the radio core [35, 138, 139].

In conclusion, the fact that distinct models are able to reproduce different observations suggests that also for PKS 1510-089 several regions contribute to the overall emission. Flaring episodes can be caused by activity in various zones of the blazar indeed, eventually with one or more regions dominating over the other ones.

From the analysis presented above and in Chapter 4 it emerges that for a deeper understanding of the phenomena taking place in FSRQs a combined effort from the experimental and theoretical point of view is required.

Conclusions

In this PhD thesis the very high energy emission from blazars using MAGIC telescope observations has been studied.

Three different objects have been examined: the newly discovered 1ES 1727+502 and the two FSRQs 3C 279 and PKS 1510-089. MAGIC data have been analysed and combined with multiwavelength observations at lower energies. The broadband spectral energy distributions and multiwavelength light curves have been examined and possible interpretations have been discussed. The results obtained have been compared with the expected behaviour of other sources of the same type and with historical observations. Some of the still open questions have been examined and issues to be addressed with future studies have been identified.

The BL Lac object **1ES 1727+502** is a newly discovered very high energy emitter. Its behaviour has been interpreted adopting the standard scenario of BL Lac objects, with a single zone leptonic model, considering the synchrotron self-Compton mechanism. The values of the parameters obtained by fitting the spectral energy distribution are in agreement with the ones of sources belonging to the same class. A peculiar aspect of these observations is that the source was not observed as follow-up of flaring states taking place at lower energies. Instead, 1ES 1727+502 was selected both from an X-ray catalogue and because of the properties reported by *Fermi*-LAT. The discovery of 1ES 1727+502 proves the importance of selecting targets of observations using different strategies.

Even if the two FSRQs 3C 279 and PKS 1510-089 are known very high energy γ-ray emitters, the origin of their emission is matter of debate. Going into details, **3C 279** was observed during the year 2011 as part of two different campaigns: at first during regular monitoring and then after high activity states were registered in the *Fermi*-LAT and optical bands. In none of the periods a significant detection was found and upper limits have been computed. The upper limits are below the flux levels measured during previous detections of the source, confirming that 3C 279 was in a low activity state at very high energy γ rays. MAGIC upper limits have been complemented with multiwavelength observations. The resulting light curves and spectral energy distributions have been examined. Leptonic emission models were applied. For monitoring observations, leptonic models with inverse Compton radia-

tion from low energy photons external to the jet reproduce the observed behaviour (two different scenarios have been considered: low energy photons from the broad line region in one case, and from the infra-red torus in the other one). At the time of MAGIC follow-up observations enhanced activity states have been observed at lower energies. The spectral energy distribution was fitted with a two-zone leptonic model in which the emission from X-ray to γ rays is generated in a zone internal to the broad line region, while the optical emission comes from a region located close to the radio core. The features observed in the optical polarised flux have been interpreted as a signature of a bending in the jet of 3C 279.

The FSRQ **PKS 1510-089** was observed by the MAGIC telescopes during 2012 and 2013. Both data sets have been analysed here. The source showed similar very high energy properties in the two different years: a soft spectrum and no variability. The absence of variability at very high energies is an unusual property for a FSRQ, since the two other FSRQs known in this band showed pronounced single night variability. MAGIC observations of 2012 were complemented with multiwavelength data. The spectral energy distribution has been fitted using two different leptonic models. In one case, the emission region is located within the infra-red torus which provides low energy photons target for the inverse Compton process. In the other one, the emission region is located further down the jet, close to the radio core. Here low energy photons are coming from a slow sheat surrounding the jet. The latter interpretation is favoured because it takes into account the constraints obtained from the multiwavelength light curve, in particular the co-spatiality of the radio and high energy emission.

The observations here presented confirm that these two sources, 3C 279 and PKS 1510-089, have a rich behaviour, which requires the development of models able to predict the temporal evolution of the emission.

In addition to the observations of the three blazars 1ES 1727+502, 3C 279 and PKS 1510-089, the results of follow-up observations of a neutrino trigger sent by the IceCube detector for the source **RGB 0505+612** are presented. This source, currently non detected at very high energy γ rays, is classified as an active galactic nucleus of unknown type. In the data here analysed no significant signal was found and an upper limit on the integral flux was derived. These results show that the neutrino follow-up program is in operation so that in the future a multimessenger approach, combining multiwavelength and neutrino observations, can be adopted to test and constrain emission models.

I performed this work as a member of the MAGIC collaboration. My contribution consisted in the analysis of MAGIC data. Multiwavelength observations as well as modelling of the spectral energy distributions have been provided by collaborators. The results shown in Chapter 4 have been published in dedicated papers [31, 35, 36], to which I contributed not only analysing MAGIC data but also participating

in the discussions for the interpretation.

Appendix A

In this Appendix, additional material on the analysis of MAGIC data of the blazars 1ES 1727+502, 3C 279 and PKS 1510-089 presented in Chapter 4 is provided. In detail, the results of the signal search for every single night of observations of all four campaigns are presented (Tab. A.2 for 1ES 1727+502, Tab. A.3 for 3C 279 and Tab. A.6 and Tab. A.8 for PKS 1510-089 observations).

For 1ES 1727+502, earlier VHE observations are compared in Tab. A.1.

For 3C 279 the numerical values of the differential upper limits and the integral upper limits obtained assuming different spectral slopes are reported in Tab. A.4 and Tab. A.5 respectively.

Finally, for PKS 1510-089 the results obtained with different unfolding algorithms are shown in Tab. A.7 and Tab. A.9.

Period	exposure time [h]	σ	flux % Crab Nebula	experiment
March - April 1995	2.31	-1.27	<8.6% ($E > 300\,\mathrm{GeV}$)	Whipple [115]
April - May 1996	2.32	0.61	< 15% ($E > 300\,\mathrm{GeV}$)	Whipple [115]
May 2006 - May 2007	6.1	1.5	< 11.8% ($E > 140\,\mathrm{GeV}$)	MAGIC-1 [33]
June 2010	5.6	data	discarded	MAGIC
May - June 2011	12.6	5.5	(2.1±0.4)% ($E > 150\,\mathrm{GeV}$)	MAGIC this work and [31]

Table A.1: Very high energy observations of 1ES 1727+502. In the first column the period of observations is reported, in column two to five the exposure time in hours, the statistical significance, the flux or upper limits expressed as percentage of the Crab Nebula flux and the experiment which performed the observations.

Date	Time [h]	N_{on} [counts]	N_{off} [counts]	N_{ex} [counts]	SBR [%]	σ	γ-rate [min^{-1}]	background rate [min^{-1}]
all	12.59	199	125.2±5.0	73.8±15.0	58.9±12.9	5.47	0.10±0.02	0.17±0.01
09.05.2011	0.56	10	6.1±1	3.9±3.3	64.2±59.7	1.30	0.12±0.1	0.18±0.03
10.05.2011	1.08	13	9.6±1.4	3.4±3.9	35.4±42.3	0.94	0.05±0.06	0.15±0.02
11.05.2011	1.60	19	17±1.8	2.0±4.7	11.8±28.4	0.43	0.02±0.05	0.18±0.02
12.05.2011	0.58	8	3±0.8	5.0±2.9	166.7±116.7	2.10	0.14±0.08	0.09±0.02
24.05.2011	0.96	10	7.2±1.2	2.8±3.4	38.9±49.6	0.89	0.05±0.06	0.13±0.02
30.05.2011	0.92	23	11.6±1.5	11.4±5.0	98.8±48.9	2.64	0.21±0.09	0.21±0.03
31.05.2011	1.31	32	19.8±2.0	12.2±6.0	61.7±32.8	2.27	0.16±0.08	0.25±0.03
05.06.2011	0.68	9	7.2±1.2	1.8±3.2	25.0±46.6	0.59	0.04±0.08	0.18±0.03
06.06.2011	0.55	12	6.3±1.1	5.7±3.6	91.7±65.5	1.81	0.17±0.11	0.19±0.03
08.06.2011	2.06	40	20.9±2.0	19.1±6.6	91.7±35.5	3.33	0.15±0.05	0.17±0.02
09.06.2011	1.70	22	16.1±1.8	5.9±5.0	36.3±32.6	1.25	0.06±0.05	0.16±0.02

Table A.2: Results of 2011 MAGIC observations of 1ES 1727+502. Observation time, number of ON-events N_{on}, number of OFF-events N_{off}, number of excess-events N_{ex}, the sky night background rate SBR, the statistical significance [126], the rate of γ and the background rate are reported for every observation night.

Date	Time [h]	N_{on} [counts]	N_{off} [counts]	N_{ex} [counts]	SBR [%]	σ	γ-rate [min^{-1}]	background rate [min^{-1}]
all	17.85	5224	5144.0 ± 71.7	80.0 ± 101.8	1.6 ± 2.0	0.79	0.07 ± 0.10	4.80 ± 0.07
Period-1	11.61	3388	3354.0 ± 57.9;	34.0 ± 82.1	1.0 ± 2.5	0.41	0.05 ± 0.12	4.81 ± 0.08
Period-2	6.23	1836	1790.0 ± 42.3	46.0 ± 60.2	2.6 ± 3.4	0.76	0.12 ± 0.16	4.78 ± 0.11
08.02.2011	1.51	453	449.0 ± 21.2	4.0 ± 30.0	0.9 ± 6.7	0.13	0.04 ± 0.33	4.95 ± 0.23
11.02.2011	2.22	676	643.0 ± 25.4	33.0 ± 36.3	5.1 ± 5.8	0.91	0.25 ± 0.27	4.83 ± 0.19
12.02.2011	0.85	219	240.0 ± 15.5	-21.0 ± 21.4	-8.7 ± 8.5	-0.98	-0.41 ± 0.42	4.73 ± 0.31
13.02.2011	1.14	351	327.0 ± 18.1	24.0 ± 26.0	7.3 ± 8.2	0.92	0.35 ± 0.38	4.77 ± 0.26
14.02.2011	0.58	154	165.0 ± 12.8	-11.0 ± 17.9	-6.7 ± 10.5	-0.62	-0.32 ± 0.52	4.77 ± 0.37
27.02.2011	0.79	270	241.0 ± 15.5	29.0 ± 22.6	12.0 ± 9.9	1.28	0.61 ± 0.47	5.06 ± 0.33
28.02.2011	1.18	304	277.0 ± 16.6	27.0 ± 24.1	9.7 ± 9.1	1.12	0.38 ± 0.34	3.92 ± 0.24
01.03.2011	0.88	301	280.0 ± 16.7	21.0 ± 24.1	7.5 ± 8.9	0.87	0.40 ± 0.46	5.32 ± 0.32
03.03.2011	0.34	65	78.0 ± 8.8	-13.0 ± 12.0	-16.7 ± 14.0	-1.09	-0.63 ± 0.58	3.79 ± 0.43
28.03.2011	0.59	150	200.0 ± 14.1	-50.0 ± 18.7	-25.0 ± 8.1	-2.68	-1.41 ± 0.53	5.66 ± 0.40
30.03.2011	0.80	226	248.0 ± 15.7	-22.0 ± 21.8	-8.9 ± 8.4	-1.01	-0.46 ± 0.45	5.18 ± 0.33
11.04.2011	0.74	219	206.0 ± 14.4	13.0 ± 20.6	6.3 ± 10.3	0.63	0.29 ± 0.47	4.66 ± 0.32
01.06.2011	1.30	393	370.0 ± 19.2	23.0 ± 27.6	6.2 ± 7.7	0.83	0.29 ± 0.35	4.73 ± 0.25
02.06.2011	0.94	312	280.0 ± 16.7	32.0 ± 24.3	11.4 ± 9.2	1.32	0.57 ± 0.43	4.95 ± 0.30
03.06.2011	1.17	357	358.0 ± 18.9	-1.0 ± 26.7	-0.3 ± 7.5	-0.04	-0.01 ± 0.38	5.12 ± 0.27
04.06.2011	0.43	125	123.0 ± 11.1	2.0 ± 15.7	1.6 ± 12.9	0.13	0.08 ± 0.61	4.73 ± 0.43
05.06.2011	1.13	336	343.0 ± 18.5	-7.0 ± 26.1	-2.0 ± 7.5	-0.27	-0.10 ± 0.38	5.05 ± 0.27
06.06.2011	1.26	313	316.0 ± 17.8	-3.0 ± 25.1	-0.9 ± 7.9	-0.12	-0.04 ± 0.33	4.20 ± 0.24

Table A.3: Results of 2011 MAGIC observations of 3C 279. Observation time, number of ON-events N_{on}, number of OFF-events N_{off}, number of excess-events N_{ex}, the sky night background rate SBR, the statistical significance [126], the rate of γ and the background rate are reported for the entire data sample, for *Period-1* (8 February - 11 April), *Period-2* (1-6 June) and for every single night.

Energy	Upper Limit [10^{-12} erg cm^{-2}s^{-1}]		
[GeV]	*Period-1*	*Period-2*	all 2011 data
147.1	10.7	16.0	10.9
303.6	0.8	2.9	0.8

Table A.4: MAGIC 2011 differential upper limits at Earth (without correction for EBL absorption). In the first column the energy is listed. In columns two to four, the differential upper limits for the individual periods and the overall data sample are reported.

Period	slope	Upper Limit $> 125\,\mathrm{GeV}$ [10^{-11} cm^{-2}s^{-1}]	difference
	3.5	1.3	
Period-1	2.5	1.2	$\sim 10\%$
	4.5	1.4	$\sim 5\%$
	3.5	3.7	
Period-2	2.5	3.3	$\sim 10\%$
	4.5	3.1	$\sim 15\%$

Table A.5: Upper limits on the integral flux calculated assuming different slopes (without correction for EBL absorption).

Date	Time [h]	N_{on} [counts]	N_{off} [counts]	N_{ex} [counts]	SBR [%]	σ	γ-rate [min^{-1}]	background rate [min^{-1}]
all	21.46	8630	8017.3 ± 51.7	612.7 ± 106.3	7.6 ± 1.4	5.83	0.48 ± 0.08	6.23 ± 0.04
Period-A	11.07	4055	3675.7 ± 35.0	379.3 ± 72.7	10.3 ± 2.0	5.31	0.57 ± 0.11	5.54 ± 0.05
Period-B	10.40	4575	4341.7 ± 38.0	233.3 ±77.6	5.4±1.8	3.03	0.37 ± 0.12	6.96 ± 0.06
03.02.2012	0.69	234	182.3 ± 7.8	51.7 ± 17.2	28.3 ± 10.0	3.14	1.25 ± 0.41	4.40 ± 0.19
19.02.2012	0.70	251	236.8 ± 8.9	14.2 ± 18.2	6.0 ± 7.8	0.79	0.34 ± 0.43	5.64 ± 0.21
22.02.2012	1.36	499	466.0 ± 12.5	33.0 ± 25.6	7.1 ± 5.6	1.30	0.40 ± 0.31	5.71 ± 0.15
25.02.2012	0.82	248	230.0 ± 8.7	18.0 ± 18.0	7.8 ± 8.0	1.01	0.36 ± 0.36	4.65 ± 0.18
26.02.2012	0.90	310	320.7 ± 10.5	-10.7 ± 20.5	-3.3 ± 6.3	-0.52	-0.20 ± 0.38	5.94 ± 0.19
29.02.2012	1.11	435	388.3 ± 11.4	46.7 ± 23.8	12.0 ± 6.3	2.00	0.70 ± 0.36	5.85 ± 0.17
01.03.2012	1.15	404	367.0 ± 11.1	37.0 ± 22.9	10.1 ± 6.4	1.64	0.54 ± 0.33	5.34 ± 0.16
02.03.2012	0.92	254	261.7 ± 9.3	-7.7 ± 18.5	-2.9 ± 7.0	-0.41	-0.14 ± 0.34	4.75 ± 0.17
03.03.2012	1.30	506	440.7 ± 12.1	65.3 ± 25.6	14.8 ± 6.0	2.62	0.84 ± 0.33	5.63 ± 0.15
04.03.2012	0.94	384	342.0 ± 10.7	42.0 ± 22.3	12.3 ± 6.7	1.92	0.75 ± 0.40	6.10 ± 0.19
05.03.2012	1.18	530	447.5 ± 12.2	82.5 ± 26.0	18.4 ± 6.1	3.26	1.17 ± 0.37	6.32 ± 0.17
16.03.2012	0.33	95	75.0 ± 5.0	20.0 ± 11.0	26.7 ± 15.5	1.90	1.02 ± 0.56	3.82 ± 0.25
19.03.2012	0.88	302	282.6 ± 9.6	19.4 ± 19.8	6.9 ± 7.1	0.99	0.37 ± 0.38	5.35 ± 0.18
20.03.2012	0.90	414	386.2 ± 11.5	27.8 ± 23.4	7.2 ± 6.2	1.20	0.51 ± 0.43	7.15 ± 0.21
21.03.2012	0.91	378	356.0 ± 10.9	22.0 ± 22.3	6.2 ± 6.4	1.00	0.40 ± 0.41	6.51 ± 0.20
22.03.2012	0.26	104	128.2 ± 6.7	-24.2 ± 12.2	-18.9 ± 9.0	-1.91	-1.53 ± 0.78	8.14 ± 0.43
23.03.2012	0.42	141	151.3 ± 7.1	-10.3 ± 13.8	-6.8 ± 9.0	-0.74	-0.41 ± 0.54	5.94 ± 0.28
24.03.2012	0.90	461	445.9 ± 12.3	15.1 ± 24.7	3.4 ± 5.6	0.62	0.28 ± 0.46	8.21 ± 0.23
25.03.2012	0.88	398	385.7 ± 11.3	12.3 ± 22.9	3.2 ± 6.0	0.54	0.23 ± 0.44	7.34 ± 0.22
26.03.2012	0.90	423	408.0 ± 11.7	15.0 ± 23.6	3.7 ± 5.8	0.64	0.28 ± 0.44	7.56 ± 0.22
27.03.2012	0.97	374	361.4 ± 10.9	12.6 ± 22.2	3.5 ± 6.2	0.57	0.22 ± 0.38	6.24 ± 0.19
29.03.2012	0.84	410	388.8 ± 11.3	21.2 ± 23.2	5.4 ± 6.0	0.92	0.42 ± 0.46	7.73 ± 0.23
30.03.2012	1.01	541	487.0 ± 12.8	54.0 ± 26.6	11.1 ± 5.6	2.07	0.89 ± 0.44	8.00 ± 0.21
01.04.2012	0.83	383	351.1 ± 10.8	31.9 ± 22.3	9.1 ± 6.5	1.45	0.64 ± 0.45	7.04 ± 0.22
03.04.2012	0.36	151	149.2 ± 7.2	1.8 ± 14.2	1.2 ± 9.6	0.13	0.08 ± 0.65	6.86 ± 0.33

Table A.6: Results of 2012 MAGIC observations of PKS 1510-089. Observation time, number of ON-events N_{on}, number of OFF-events N_{off}, number of excess-events N_{ex}, the sky night background rate SBR, the statistical significance [126], the rate of γ and the background rate are reported for the entire data sample, for the two observation periods and for every single night (if ≥ 2 symmetric wobble positions are available).

method	F_0 $[\times 10^{-14}\mathrm{GeV}^{-1}\mathrm{cm}^{-2}\mathrm{s}^{-1}]$	Γ	$F_{0,EBL}$ $[\times 10^{-14}\mathrm{GeV}^{-1}\mathrm{cm}^{-2}\mathrm{s}^{-1}]$	Γ_{EBL}
Forward unfolding	2.9 ± 0.9	4.2 ± 0.6	5.1 ± 1.9	3.5 ± 0.7
Schmelling (minimization by Gauss-Newton method)	2.8 ± 0.3	4.3 ± 0.3	5.1 ± 0.7	3.5 ± 0.3
Tikhonov (minimization by MINUIT)	2.8± 0.7	4.1 ± 0.7	5.2 ± 1.6	3.2 ± 0.8
Bertero (under-constrained case)	3.0± 0.8	3.8 ± 0.4	5.3 ± 1.3	3.2 ± 0.4

Table A.7: PKS 1510-089, flux obtained from 2012 observations. The flux has been fitted with a power law function $dF/dE = F_0(E/200\,GeV)^{-\Gamma}$ in the unfolding procedure and the resulting parameters, obtained using different unfolding methods, for both observed and EBL-corrected flux [81], are shown. The results obtained with the algorithm "Tikhonov" are shown in Section 4.3.

Date	Time [h]	N_{on} [counts]	N_{off} [counts]	N_{ex} [counts]	SBR [%]	σ	γ-rate [min^{-1}]	background rate [min^{-1}]
all	17.35	4492	4086.0 ± 36.9	406.0 ± 76.5	9.9 ± 1.9	5.39	0.39 ± 0.07	3.93 ± 0.04
Period-A	6.04	1484	1389.0 ± 21.5	95.0 ± 44.1	6.8 ± 3.2	2.18	0.26 ± 0.12	3.83 ± 0.06
Period-B	7.18	1927	1713.3 ± 23.9	213.7 ± 50.0	12.5 ± 3.0	4.36	0.50 ± 0.12	3.98 ± 0.06
Period-C	4.13	1081	983.7 ± 18.1	97.3 ± 37.5	9.9 ± 3.9	2.63	0.39 ± 0.15	3.97 ± 0.07
15.03.2013 ⋆	0.63	174	174.0 ± 13.2	0.0 ± 18.7	0.0 ± 10.7	0.00	0.00 ± 0.50	4.62 ± 0.35
18.03.2013	1.29	310	281.3 ± 9.7	28.7 ± 20.1	10.2 ± 7.3	1.45	0.37 ± 0.26	3.63 ± 0.13
20.03.2013	1.38	369	352.0 ± 10.8	17.0 ± 22.1	4.8 ± 6.3	0.78	0.21 ± 0.27	4.26 ± 0.13
21.03.2013	1.66	477	428.7 ± 12.0	48.3 ± 24.9	11.3 ± 6.0	1.98	0.48 ± 0.25	4.30 ± 0.12
24.03.2013 ⋆	0.57	131	110.0 ± 10.5	21.0 ± 15.5	19.1 ± 15.4	1.35	0.62 ± 0.46	3.24 ± 0.31
25.03.2013 ⋆⋆	0.29	12	14.0 ± 3.7	-2.0 ± 5.1	-14.3 ± 33.7	-0.39	-0.11 ± 0.29	0.79 ± 0.21
02.05.2013 ⋆	0.64	211	177.0 ± 13.3	34.0 ± 19.7	19.2 ± 12.2	1.73	0.89 ± 0.51	4.62 ± 0.35
03.05.2013	1.49	417	396.0 ± 11.5	21.0 ± 23.4	5.3 ± 6.0	0.90	0.23 ± 0.26	4.42 ± 0.13
04.05.2013	1.30	382	338.0 ± 10.6	44.0 ± 22.2	13.0 ± 6.8	2.02	0.56 ± 0.29	4.34 ± 0.14
05.05.2013 ⋆	0.41	142	117.0 ± 10.8	25.0 ± 16.1	21.4 ± 15.2	1.55	1.01 ± 0.65	4.73 ± 0.44
06.05.2013 ⋆	0.64	217	197.0 ± 14.0	20.0 ± 20.3	10.2 ± 10.8	0.98	0.52 ± 0.53	5.13 ± 0.37
08.05.2013	1.04	216	176.3 ± 7.7	39.7 ± 16.6	22.5 ± 9.9	2.48	0.63 ± 0.26	2.82 ± 0.12
12.05.2013 ⋆	0.38	77	60.0 ± 7.7	17.0 ± 11.7	28.3 ± 22.1	1.45	0.75 ± 0.51	2.64 ± 0.34
28.05.2013 ⋆	0.61	143	126.0 ± 11.2	17.0 ± 16.4	13.5 ± 13.9	1.04	0.46 ± 0.44	3.42 ± 0.30
29.05.2013 ⋆	0.71	203	189.0 ± 13.7	14.0 ± 19.8	7.4 ± 10.9	0.71	0.33 ± 0.46	4.42 ± 0.32
30.05.2013	1.79	469	408.7 ± 11.7	60.3 ± 24.6	14.8 ± 6.2	2.51	0.56 ± 0.23	3.81 ± 0.11
01.06.2013 ⋆	0.49	160	186.0 ± 13.6	-26.0 ± 18.6	-14.0 ± 9.3	-1.40	-0.88 ± 0.63	6.31 ± 0.46

Table A.8: Results of 2013 MAGIC observations of PKS 1510-089. Observation time, number of ON-events N_{on}, number of OFF-events N_{off}, number of excess-events N_{ex}, the sky night background rate SBR, the statistical significance [126], the rate of γ and the background rate are reported for the entire data sample, for the three observation periods and for every single night. If 4 wobble positions were available, the same analysis options of the larger data samples were applied (*signal cut* 0.0124, three off regions for background estimation), otherwise (nights with ⋆) a *signal cut* 0.0143 (0.0187 for ⋆⋆) was applied and one off region was used for background estimation.

method	F_0 $[\times 10^{-14}\mathrm{GeV}^{-1}\mathrm{cm}^{-2}\mathrm{s}^{-1}]$	Γ	$F_{0,EBL}$ $[\times 10^{-14}\mathrm{GeV}^{-1}\mathrm{cm}^{-2}\mathrm{s}^{-1}]$	Γ_{EBL}
Forward unfolding	3.9 ± 1.1	4.5 ± 0.5	7.2 ± 2.3	3.8 ± 0.6
Schmelling (minimization by Gauss-Newton method)	3.2 ± 0.7	4.9 ± 0.5	6.1 ± 1.3	4.0 ± 0.5
Tikhonov (minimization by MINUIT)	3.4 ± 1.1	4.2 ± 0.7	6.5 ± 2.1	3.3 ± 0.7

Table A.9: PKS 1510-089, flux obtained from 2013 observations. The flux has been fitted with a power law function $dF/dE = F_0(E/200\,GeV)^{-\Gamma}$ in the unfolding procedure and the resulting parameters, obtained using different unfolding methods, for both observed and EBL-corrected flux [81], are shown. The results obtained with the algorithm "Tikhonov" are shown in Section 4.3.

Appendix B

B.1 Follow-up observations of neutrino triggers

In this thesis the results of observations triggered by high activity states in the optical and high energy γ-ray band have been presented. Beside these follow-up observations, a multimessenger approach is possible. MAGIC indeed takes part into the "high energy γ-ray follow-up program using neutrino triggers from IceCube" [116]. A list of pre-selected sources which are promising hadron accelerators based on the information contained in the second Fermi-*LAT* catalogue [152] is monitored by the IceCube detector. If an excess of neutrinos is found in the online analysis, an alert is sent to the MAGIC telescopes and follow-up observations are performed as soon as possible (the IceCube detector is continuously monitoring the sky while MAGIC observations take place during night and are limited by atmospheric conditions and the moon). Typically one hour of data is collected and, in case a significant signal is found by the fast analysis performed off-line the following day, observations continue also during successive nights.

B.2 RGB 0505+612

An IceCube alert was triggered by the object RGB 0505+612, a source visible in radio, X-rays and high energy γ rays[1] and classified as an active galactic nucleus of unknown type in the Fermi-*LAT* catalogue [13]. The IceCube alert was sent on 13 September 2013 and MAGIC performed follow-up observations in the night of 14 September 2013. One hour of good quality data was taken, corresponding to an effective time of 0.90 hours, at medium zenith angles $35° - 40°$.

The data have been analysed with both a full range and a low energy analysis. The sky maps do not show any detection (Fig. B.1). The significances have been computed for three different cases (see Section 2.2.2):

I : full range analysis with *signal* cut 0.0124;

[1] `http://simbad.u-strasbg.fr/`

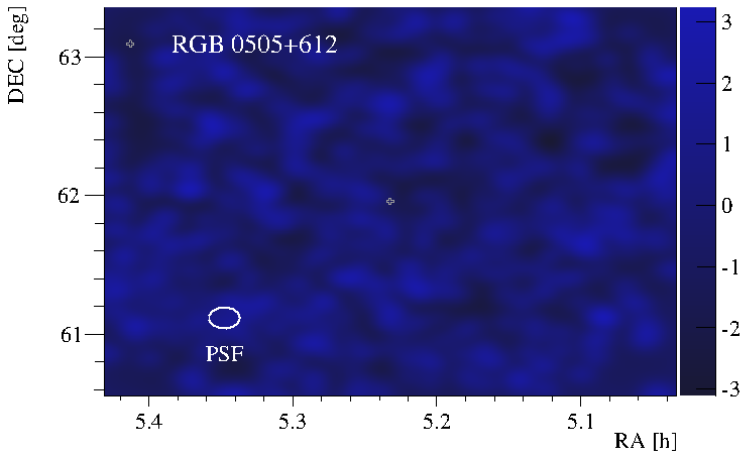

(a) Full range analysis;

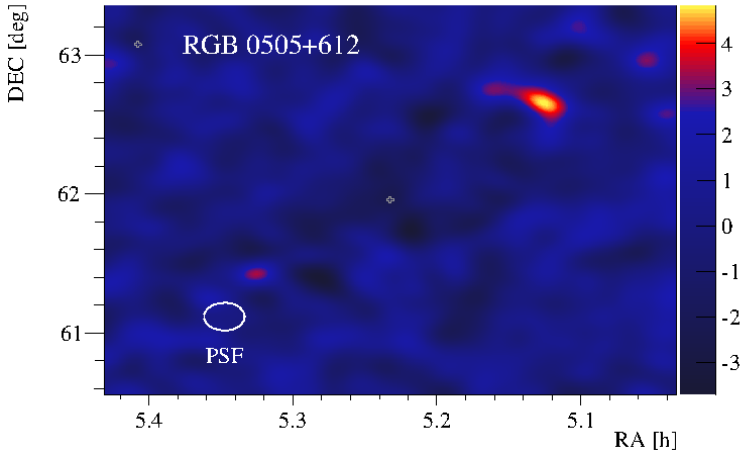

(b) low energy analysis.

Figure B.1: The sky maps obtained from MAGIC follow-up observations of RGB 0505+612 for the full range and low energy analysis. The colour scale indicates the "test statistics" based on [126]. No significant signal is found at the pointed position (grey cross). The *hot spot* visible in the low energy sky map has found to be non-significant (see Tab.B.1).

analysis	N_{on} [counts]	N_{off} [counts]	N_{ex} [counts]	SBR [%]	σ	γ-rate [min^{-1}]	background rate [min^{-1}]
I	12	14.0 ± 3.7	-2.0 ± 5.1	-14.3 ± 33.7	-0.39	-0.04 ± 0.09	0.26 ± 0.07
II	176	191.0 ± 13.8	-15.0 ± 19.2	-7.9 ± 9.6	-0.78	-0.28 ± 0.36	3.54 ± 0.26
III	122	94.0 ± 9.7	28.0 ± 14.7	29.8 ± 17.8	1.91	0.52 ± 0.27	1.74 ± 0.18

Table B.1: Results of MAGIC follow-up observations of RGB 0505+612. Observation time, number of ON-events N_{on}, number of OFF-events N_{off}, number of excess-events N_{ex}, the sky night background rate SBR, the statistical significance [126], the rate of γ and the background rate obtained applying three different analysis settings are reported: (I) full range analysis with *signal* cut 0.0124, (II) low energy analysis with *signal* cut 0.0124, (III) low energy analysis with *signal* cut 0.0153 centred at coordinates RA 5.1277,h, DEC62.55° (the *hot spot* of Fig. B.1b). In none of the cases a significant detection was found.

II : low energy analysis with *signal* cut 0.0143;

III : low energy analysis with *signal* cut 0.0153 at coordinates RA 5.1277 h, DEC 62.55° which correspond to the position of the *hot spot* visible in the low energy sky map (Fig. B.1).

The results are shown in Tab. B.1: no significant signal was found.

An upper limit on the flux has been computed assuming a power law function with spectral index $\Gamma = 2.6$. Since there are no measurements of the flux of this source at VHE γ rays, the value of the spectral index is unknown. The value $\Gamma = 2.6$ is the spectral index which is usually found at VHE for sources having a spectrum with similar properties. In detail, in the second *Fermi*-LAT catalogue RGB 0505+612 is classified as a high synchrotron peaked active galactic nucleus (the low energy peak of the spectral energy distribution is located at frequencies $> 10^{15}$ Hz) and the *Fermi*-LAT flux computed from data is represented by a power law function with spectral index $\Gamma = 1.8$ [13]. VHE emitter which have these two properties have spectral indices above 100 GeV with values ~ 2.6 (e.g. Mrk 421 [4, 10], Mrk 501 [45], 1ES 1959+650 [26]).

For the calculation of the upper limit a cut on the *image size* > 50 photo-electrons was applied and the cuts on the parameters ϑ^2 and *hadroness* have been determined requiring Monte-Carlo efficiencies of 90% and 80% respectively (see Section 2.2.2). The integral upper limit on the flux for energies larger than 200 GeV is $9.52 \cdot 10^{-12}\,\mathrm{cm}^{-2}\mathrm{s}^{-1}$.

B.3 Conclusions

The MAGIC telescopes perform follow-up observations triggered not only by alerts from telescopes observing in other wavebands of the electromagnetic spectrum, but also from a neutrino telescope, the IceCube detector. In this Appendix the results of follow-up observations for the source RGB 0505+612 are presented. MAGIC observations took place one day after the alert, and one hour of data were collected. No significant signal was found, confirming the results obtained with the fast analysis performed the day after observations. These results show that the program of follow-up of neutrino triggers between IceCube and MAGIC telescopes is in operation. In the future, a multimessenger approach can be adopted combining information from telescopes observing in different energy bands of the electromagnetic spectrum and from neutrino observatories. Such strategy is a very powerful tool because it can lead not only to the discovery of new sources but can also test and constrain emission models, in particular hadronic scenarios.

List of Figures

List of Tables

Bibliography

[1] A. A. Abdo et al. "A change in the optical polarization associated with a γ-ray flare in the blazar 3C279". In: *Nature* 463 (Feb. 2010), pp. 919–923. DOI: 10.1038/nature08841. arXiv:1004.3828 [astro-ph.CO].

[2] A. A. Abdo et al. "Fermi Large Area Telescope and Multi-wavelength Observations of the Flaring Activity of PKS 1510-089 between 2008 September and 2009 June". In: *Astrophysical Journal* 721 (Oct. 2010), pp. 1425–1447. DOI: 10.1088/0004-637X/721/2/1425. arXiv:1007.1237 [astro-ph.CO].

[3] A. A. Abdo et al. "Fermi Large Area Telescope First Source Catalog". In: *Astrophysical Journal, Supplement* 188 (June 2010), pp. 405–436. DOI: 10.1088/0067-0049/188/2/405. arXiv:1002.2280 [astro-ph.HE].

[4] A. A. Abdo et al. "Fermi Large Area Telescope Observations of Markarian 421: The Missing Piece of its Spectral Energy Distribution". In: *Astrophysical Journal* 736, 131 (Aug. 2011), p. 131. DOI: 10.1088/0004-637X/736/2/131. arXiv:1106.1348 [astro-ph.HE].

[5] A. A. Abdo et al. "Spectral Properties of Bright Fermi-Detected Blazars in the Gamma-Ray Band". In: *Astrophysical Journal* 710 (Feb. 2010), pp. 1271–1285. DOI: 10.1088/0004-637X/710/2/1271. arXiv:1001.4097 [astro-ph.HE].

[6] A. A. Abdo et al. "The First Catalog of Active Galactic Nuclei Detected by the Fermi Large Area Telescope". In: *Astrophysical Journal* 715 (May 2010), pp. 429–457. DOI: 10.1088/0004-637X/715/1/429. arXiv:1002.0150 [astro-ph.HE].

[7] A. A. Abdo et al. "The Spectral Energy Distribution of Fermi Bright Blazars". In: *Astrophysical Journal* 716 (June 2010), pp. 30–70. DOI: 10.1088/0004-637X/716/1/30. arXiv:0912.2040 [astro-ph.CO].

[8] A. Abramowski et al. "Discovery of extended VHE γ-ray emission from the vicinity of the young massive stellar cluster Westerlund 1". In: *Astronomy and Astrophysics* 537, A114 (Jan. 2012), A114. DOI: 10.1051/0004-6361/201117928. arXiv:1111.2043 [astro-ph.HE].

[9] V. A. Acciari et al. "Discovery of TeV Gamma-ray Emission from Tycho's Supernova Remnant". In: *Astrophysical Journal, Letters* 730, L20 (Apr. 2011), p. L20. DOI: 10.1088/2041-8205/730/2/L20. arXiv:1102.3871 [astro-ph.HE].

[10] V. A. Acciari et al. "Observation of Markarian 421 in TeV gamma rays over a 14-year time span". In: *Astroparticle Physics* 54 (Feb. 2014), pp. 1–10. DOI: 10.1016/j.astropartphys.2013.10.004. arXiv:1310.8150 [astro-ph.HE].

[11] F. Acero et al. "Detection of Gamma Rays from a Starburst Galaxy". In: *Science* 326 (Nov. 2009), pp. 1080–. DOI: 10.1126/science.1178826. arXiv:0909.4651 [astro-ph.HE].

[12] M. Ackermann et al. "The Imprint of the Extragalactic Background Light in the Gamma-Ray Spectra of Blazars". In: *Science* 338 (Nov. 2012), pp. 1190–. DOI: 10.1126/science.1227160. arXiv:1211.1671 [astro-ph.CO].

[13] M. Ackermann et al. "The Second Catalog of Active Galactic Nuclei Detected by the Fermi Large Area Telescope". In: *Astrophysical Journal* 743, 171 (Dec. 2011), p. 171. DOI: 10.1088/0004-637X/743/2/171. arXiv:1108.1420 [astro-ph.HE].

[14] F. Aharonian et al. "A low level of extragalactic background light as revealed by γ-rays from blazars". In: *Nature* 440 (Apr. 2006), pp. 1018–1021. DOI: 10.1038/nature04680. eprint: astro-ph/0508073.

[15] F. Aharonian et al. "Detection of extended very-high-energy γ-ray emission towards the young stellar cluster Westerlund 2". In: *Astronomy and Astrophysics* 467 (June 2007), pp. 1075–1080. DOI: 10.1051/0004-6361:20066950. eprint: astro-ph/0703427.

[16] F. Aharonian et al. "Evidence for TeV gamma ray emission from Cassiopeia A". In: *Astronomy and Astrophysics* 370 (Apr. 2001), pp. 112–120. DOI: 10.1051/0004-6361:20010243. eprint: astro-ph/0102391.

[17] F. Aharonian et al. "Is the giant radio galaxy M 87 a TeV gamma-ray emitter?" In: *Astronomy and Astrophysics* 403 (May 2003), pp. L1–L5. DOI: 10.1051/0004-6361:20030372. eprint: astro-ph/0302155.

[18] F. Aharonian et al. "The unidentified TeV source (TeV J2032+4130) and surrounding field: Final HEGRA IACT-System results". In: *Astronomy and Astrophysics* 431 (Feb. 2005), pp. 197–202. DOI: 10.1051/0004-6361:20041552.

[19] F. A. Aharonian. "TeV gamma rays from BL Lac objects due to synchrotron radiation of extremely high energy protons". In: *New Astronomy* 5 (Nov. 2000), pp. 377–395. DOI: 10.1016/S1384-1076(00)00039-7. eprint: astro-ph/0003159.

[20] F. A. Aharonian et al. "High-energy particle acceleration in the shell of a supernova remnant". In: *Nature* 432 (Nov. 2004), pp. 75–77. DOI: 10.1038/nature02960. eprint: astro-ph/0411533.

[21] J. Albert et al. "Detection of Very High Energy Radiation from the BL Lacertae Object PG 1553+113 with the MAGIC Telescope". In: *Astrophysical Journal, Letters* 654 (Jan. 2007), pp. L119–L122. DOI: 10.1086/511384. eprint: arXiv:astro-ph/0606161.

[22] J. Albert et al. "Discovery of Very High Energy Gamma Radiation from IC 443 with the MAGIC Telescope". In: *Astrophysical Journal, Letters* 664 (Aug. 2007), pp. L87–L90. DOI: 10.1086/520957. arXiv:0705.3119.

[23] J. Albert et al. "Discovery of Very High Energy Gamma Rays from 1ES 1218+30.4". In: *Astrophysical Journal, Letters* 642 (May 2006), pp. L119–L122. DOI: 10.1086/504845. eprint: arXiv:astro-ph/0603529.

[24] J. Albert et al. "Implementation of the Random Forest method for the Imaging Atmospheric Cherenkov Telescope MAGIC". In: *Nuclear Instruments and Methods in Physics Research A* 588 (Apr. 2008), pp. 424–432. DOI: 10.1016/j.nima.2007.11.068. arXiv:0709.3719.

[25] J. Albert et al. "MAGIC Upper Limits on the Very High Energy Emission from Gamma-Ray Bursts". In: *Astrophysical Journal* 667 (Sept. 2007), pp. 358–366. DOI: 10.1086/520761. eprint: astro-ph/0612548.

[26] J. Albert et al. "Observation of Very High Energy Gamma-Ray Emission from the Active Galactic Nucleus 1ES 1959+650 Using the MAGIC Telescope". In: *Astrophysical Journal* 639 (Mar. 2006), pp. 761–765. DOI: 10.1086/499421. eprint: astro-ph/0508543.

[27] J. Albert et al. "Unfolding of differential energy spectra in the MAGIC experiment". In: *Nuclear Instruments and Methods in Physics Research A* 583 (Dec. 2007), pp. 494–506. DOI: 10.1016/j.nima.2007.09.048. arXiv:0707.2453.

[28] J. Albert et al. "Variable Very-High-Energy Gamma-Ray Emission from the Microquasar LS I +61 303". In: *Science* 312 (June 2006), pp. 1771–1773. DOI: 10.1126/science.1128177. eprint: astro-ph/0605549.

[29] J. Albert et al. "Very-High-Energy gamma rays from a Distant Quasar: How Transparent Is the Universe?" In: *Science* 320 (June 2008), pp. 1752–. DOI: 10.1126/science.1157087. arXiv:0807.2822.

[30] J. Aleksić et al. "Detection of bridge emission above 50 GeV from the Crab pulsar with the MAGIC telescopes". In: *ArXiv e-prints* (Feb. 2014). arXiv : 1402.4219 (astro-ph.HE).

[31] J. Aleksić et al. "Discovery of very high energy gamma-ray emission from the blazar 1ES 1727+502 with the MAGIC Telescopes". In: *Astronomy and Astrophysics* 563, A90 (Mar. 2014), A90. DOI: 10.1051/0004-6361/201321360. arXiv:1302.6140 [astro-ph.HE].

[32] J. Aleksić et al. "Discovery of VHE γ-rays from the blazar 1ES 1215+303 with the MAGIC telescopes and simultaneous multi-wavelength observations". In: *Astronomy and Astrophysics* 544, A142 (Aug. 2012), A142. DOI: 10.1051/0004-6361/201219133. arXiv:1203.0490 [astro-ph.HE].

[33] J. Aleksić et al. "Gamma-ray Excess from a Stacked Sample of High- and Intermediate-frequency Peaked Blazars Observed with the MAGIC Telescope". In: *Astrophysical Journal* 729, 115 (Mar. 2011), p. 115. DOI: 10.1088/0004-637X/729/2/115. arXiv:1002.2951 [astro-ph.HE].

[34] J. Aleksić et al. "MAGIC Discovery of Very High Energy Emission from the FSRQ PKS 1222+21". In: *Astrophysical Journal, Letters* 730, L8 (Mar. 2011), p. L8. DOI: 10.1088/2041-8205/730/1/L8. arXiv:1101.4645 [astro-ph.HE].

[35] J. Aleksić et al. "MAGIC gamma-ray and multi-frequency observations of flat spectrum radio quasar PKS 1510-089 in early 2012". In: *Astronomy and Astrophysics* 569, A46 (Sept. 2014), A46. DOI: 10.1051/0004-6361/201423484.

[36] J. Aleksić et al. "MAGIC observations and multifrequency properties of the flat spectrum radio quasar 3C 279 in 2011". In: *Astronomy and Astrophysics* 567, A41 (July 2014), A41. DOI: 10.1051/0004-6361/201323036. arXiv:1311.2833 [astro-ph.HE].

[37] J. Aleksić et al. "MAGIC Observations and multiwavelength properties of the quasar 3C 279 in 2007 and 2009". In: *Astronomy and Astrophysics* 530, A4 (June 2011), A4. DOI: 10.1051/0004-6361/201116497. arXiv:1101.2522 [astro-ph.CO].

[38] J. Aleksić et al. "Observations of the Crab Pulsar between 25 and 100 GeV with the MAGIC I Telescope". In: *Astrophysical Journal* 742, 43 (Nov. 2011), p. 43. DOI: 10.1088/0004-637X/742/1/43. arXiv:1108.5391 [astro-ph.HE].

[39] J. Aleksić et al. "Performance of the MAGIC stereo system obtained with Crab Nebula data". In: *Astroparticle Physics* 35 (Feb. 2012), pp. 435–448. DOI: 10.1016/j.astropartphys.2011.11.007. arXiv:1108.1477 [astro-ph.IM].

[40] J. Aleksić et al. "Phase-resolved energy spectra of the Crab pulsar in the range of 50-400 GeV measured with the MAGIC telescopes". In: *Astronomy and Astrophysics* 540, A69 (Apr. 2012), A69. DOI: 10.1051/0004-6361/201118166. arXiv:1109.6124 [astro-ph.HE].

[41] J. Aleksic et al. "The major upgrade of the MAGIC telescopes, Part I: The hardware improvements and the commissioning of the system". In: *ArXiv e-prints* (Sept. 2014). arXiv:1409.6073 [astro-ph.IM].

[42] J. Aleksic et al. "The major upgrade of the MAGIC telescopes, Part II: The achieved physics performance using the Crab Nebula observations". In: *ArXiv e-prints* (Sept. 2014). arXiv:1409.5594 [astro-ph.IM].

[43] E. Aliu et al. "Improving the performance of the single-dish Cherenkov telescope MAGIC through the use of signal timing". In: *Astroparticle Physics* 30 (Jan. 2009), pp. 293–305. DOI: 10.1016/j.astropartphys.2008.10.003. arXiv:0810.3568.

[44] E. Aliu et al. "Observation of Pulsed γ-Rays Above 25 GeV from the Crab Pulsar with MAGIC". In: *Science* 322 (Nov. 2008), pp. 1221–. DOI: 10.1126/science.1164718. arXiv:0809.2998.

[45] H. Anderhub et al. "Simultaneous Multiwavelength Observation of Mkn 501 in a Low State in 2006". In: *Astrophysical Journal* 705 (Nov. 2009), pp. 1624–1631. DOI: 10.1088/0004-637X/705/2/1624. arXiv:0910.2093 [astro-ph.HE].

[46] E. Angelakis et al. "Monitoring the radio spectra of selected blazars in the Fermi-GST era . The Effelsberg 100-m telescope covering the cm band". In: *Mem. Societa Astronomica Italiana* 79 (2008), p. 1042. arXiv:0809.3912.

[47] J. Arons. "Magnetars in the Metagalaxy: An Origin for Ultra-High-Energy Cosmic Rays in the Nearby Universe". In: *Astrophysical Journal* 589 (June 2003), pp. 871–892. DOI: 10.1086/374776. eprint: astro-ph/0208444.

[48] A. M. Atoyan and C. D. Dermer. "Neutral Beams from Blazar Jets". In: *Astrophysical Journal* 586 (Mar. 2003), pp. 79–96. DOI: 10.1086/346261. eprint: arXiv:astro-ph/0209231.

[49] W. B. Atwood et al. "The Large Area Telescope on the Fermi Gamma-Ray Space Telescope Mission". In: *Astrophysical Journal* 697 (June 2009), pp. 1071–1102. DOI: 10.1088/0004-637X/697/2/1071. arXiv:0902.1089 [astro-ph.IM].

[50] L. Ballo et al. "Spectral Energy Distributions of 3C 279 Revisited: BeppoSAX Observations and Variability Models". In: *Astrophysical Journal* 567 (Mar. 2002), pp. 50–57. DOI: 10.1086/338387. eprint: astro-ph/0111499.

[51] A. Barnacka et al. "PKS 1510-089: a rare example of a flat spectrum radio quasar with a very high-energy emission". In: *ArXiv e-prints* (July 2013). arXiv:1307.1779 [astro-ph.HE].

[52] W. Bednarek and R. J. Protheroe. "Gamma-ray and neutrino flares produced by protons accelerated on an accretion disc surface in active galactic nuclei". In: *Monthly Notices of the RAS* 302 (Jan. 1999), pp. 373–380. DOI: 10.1046/j.1365-8711.1999.02132.x. eprint: astro-ph/9802288.

[53] K. Berger. "Overview of the results from extra-galactic observations with the MAGIC telescopes". In: *International Cosmic Ray Conference*. Vol. 8. International Cosmic Ray Conference. 2011, p. 167. arXiv:1109.5860 [astro-ph.HE].

[54] J. Beringer et al. "The Review of Particle Physics". In: *Phys. Rev.* (2012).

[55] S. D. Bloom and A. P. Marscher. "An Analysis of the Synchrotron Self-Compton Model for the Multi–Wave Band Spectra of Blazars". In: *Astrophysical Journal* 461 (Apr. 1996), p. 657. DOI: 10.1086/177092.

[56] G. R. Blumenthal and R. J. Gould. "Bremsstrahlung, Synchrotron Radiation, and Compton Scattering of High-Energy Electrons Traversing Dilute Gases". In: *Reviews of Modern Physics* 42 (1970), pp. 237–271. DOI: 10.1103/RevModPhys.42.237.

[57] R. K. Bock et al. "Methods for multidimensional event classification: a case study using images from a Cherenkov gamma-ray telescope". In: *Nuclear Instruments and Methods in Physics Research A* 516 (Jan. 2004), pp. 511–528. DOI: 10.1016/j.nima.2003.08.157.

[58] M. Boettcher, D. E. Harris, and H. Krawczynski. *Relativistic Jets from Active Galactic Nuclei*. Jan. 2012.

[59] M. Böttcher, A. Reimer, and A. P. Marscher. "Implications of the very High Energy Gamma-Ray Detection of the Quasar 3C279". In: *Astrophysical Journal* 703 (Sept. 2009), pp. 1168–1175. DOI: 10.1088/0004-637X/703/1/1168.

[60] M. Böttcher et al. "Leptonic and Hadronic Modeling of Fermi-detected Blazars". In: *Astrophysical Journal* 768, 54 (May 2013), p. 54. DOI: 10.1088/0004-637X/768/1/54. arXiv:1304.0605 [astro-ph.HE].

[61] C. L. Brogan et al. "Discovery of a Radio Supernova Remnant and Nonthermal X-Rays Coincident with the TeV Source HESS J1813-178". In: *Astrophysical Journal, Letters* 629 (Aug. 2005), pp. L105–L108. DOI: 10.1086/491471. eprint: astro-ph/0505145.

[62] A. M. Brown. "Locating the γ-ray emission region of the flat spectrum radio quasar PKS 1510-089". In: *Monthly Notices of the RAS* 431 (May 2013), pp. 824–835. DOI: 10.1093/mnras/stt218. arXiv:1301.7677 [astro-ph.HE].

[63] R. Buehler et al. "Gamma-Ray Activity in the Crab Nebula: The Exceptional Flare of 2011 April". In: *Astrophysical Journal* 749, 26 (Apr. 2012), p. 26. DOI: 10.1088/0004-637X/749/1/26. arXiv:1112.1979 [astro-ph.HE].

[64] E. M. Burbidge and T. D. Kinman. "Redshifts of Fourteen Quasi-Stellar Radio Sources". In: *Astrophysical Journal* 145 (Aug. 1966), p. 654. DOI: 10.1086/148808.

[65] B. F. Burke and F. Graham-Smith. *An introduction to radio astronomy*. 1997.

[66] A. Celotti and G. Ghisellini. "The power of blazar jets". In: *Monthly Notices of the RAS* 385 (Mar. 2008), pp. 283–300. DOI: 10.1111/j.1365-2966.2007.12758.x. arXiv:0711.4112.

[67] R. Chatterjee et al. "Correlated Multi-Wave Band Variability in the Blazar 3C 279 from 1996 to 2007". In: *Astrophysical Journal* 689 (Dec. 2008), pp. 79–94. DOI: 10.1086/592598. arXiv:0808.2194.

[68] P. A. Cherenkov. "Visible Emission of Clean Liquids by Action of Radiation". In: *C. R. Acad. Sci. U.S.S.R. - Doklady Akad. Nauk SSSR* 8 (1934), p. 451.

[69] L. Costamante and G. Ghisellini. "TeV candidate BL Lac objects". In: *Astronomy and Astrophysics* 384 (Mar. 2002), pp. 56–71. DOI: 10.1051/0004-6361:20011749. eprint: arXiv:astro-ph/0112201.

[70] B. Czerny et al. "Structure and Formation of Accretion Disk Corona for Active Galactic Nuclei and Galactic Black Holes". In: *High Energy Processes in Accreting Black Holes*. Ed. by J. Poutanen and R. Svensson. Vol. 161. Astronomical Society of the Pacific Conference Series. 1999, p. 331.

[71] F. D'Ammando et al. "AGILE detection of a gamma-ray source coincident with Blazar PKS 1510-08". In: *The Astronomer's Telegram* 1436 (Mar. 2008), p. 1.

[72] F. D'Ammando et al. "AGILE detection of a rapid γ-ray flare from the blazar PKS 1510-089 during the GASP-WEBT monitoring". In: *Astronomy and Astrophysics* 508 (Dec. 2009), pp. 181–189. DOI: 10.1051/0004-6361/200912560. arXiv:0909.3484 [astro-ph.HE].

[73] F. D'Ammando et al. "AGILE detection of extreme γ-ray activity from the blazar PKS 1510-089 during March 2009. Multifrequency analysis". In: *Astronomy and Astrophysics* 529, A145 (May 2011), A145. DOI: 10.1051/0004-6361/201016128. arXiv:1103.3647 [astro-ph.HE].

[74] B. R. Dawson et al. "The energy spectrum of cosmic rays at the highest energies". In: *European Physical Journal Web of Conferences*. Vol. 53. European Physical Journal Web of Conferences. June 2013, p. 1005. DOI: 10.1051/epjconf/20135301005. arXiv:1306.6138 [astro-ph.HE].

[75] A. de Angelis, O. Mansutti, and M. Persic. "Very-high energy gamma astrophysics". In: *Nuovo Cimento Rivista Serie* 31 (Apr. 2008), pp. 187–246. DOI: 10.1393/ncr/i2008-10032-2. arXiv:0712.0315.

[76] G. de Vaucouleurs et al. *Third Reference Catalogue of Bright Galaxies. Volume I: Explanations and references. Volume II: Data for galaxies between 0^h and 12^h. Volume III: Data for galaxies between 12^h and 24^h*. 1991.

[77] C. D. Dermer and G. Menon. *High Energy Radiation from Black Holes: Gamma Rays, Cosmic Rays, and Neutrinos*. 2009.

[78] C. D. Dermer, R. Schlickeiser, and A. Mastichiadis. "High-energy gamma radiation from extragalactic radio sources". In: *Astronomy and Astrophysics* 256 (Mar. 1992), pp. L27–L30.

[79] C. Diltz and M. Böttcher. "Time dependent leptonic modeling of Fermi II processes in the jets of flat spectrum radio quasars". In: *Journal of High Energy Astrophysics* 1 (May 2014), pp. 63–70. DOI: 10.1016/j.jheap.2014.04.001. arXiv:1404.4725 [astro-ph.HE].

[80] S. Dimitrakoudis et al. "The time-dependent one-zone hadronic model. First principles". In: *Astronomy and Astrophysics* 546, A120 (Oct. 2012), A120. DOI: 10.1051/0004-6361/201219770. arXiv:1209.0413 [astro-ph.HE].

[81] A. Domínguez et al. "Extragalactic background light inferred from AEGIS galaxy-SED-type fractions". In: *Monthly Notices of the RAS* 410 (Feb. 2011), pp. 2556–2578. DOI: 10.1111/j.1365-2966.2010.17631.x. arXiv:1007.1459 [astro-ph.CO].

[82] D. Donato et al. "Hard X-ray properties of blazars". In: *Astronomy and Astrophysics* 375 (Sept. 2001), pp. 739–751. DOI: 10.1051/0004-6361:20010675. eprint: arXiv:astro-ph/0105203.

[83] R. J. H. Dunn, A. C. Fabian, and A. Celotti. "Using radio bubbles to constrain the matter content of AGN jets". In: *Monthly Notices of the RAS* 372 (Nov. 2006), pp. 1741–1748. DOI: 10.1111/j.1365-2966.2006.10986.x. eprint: arXiv:astro-ph/0608466.

[84] E. Dwek and F. Krennrich. "The extragalactic background light and the gamma-ray opacity of the universe". In: *Astroparticle Physics* 43 (Mar. 2013), pp. 112–133. DOI: 10.1016/j.astropartphys.2012.09.003. arXiv:1209.4661 [astro-ph.CO].

[85] K. Egberts et al. "Diffuse TeV Gamma-Ray Emission in the H.E.S.S. Galactic Plane Survey". In: *ArXiv e-prints* (Aug. 2013). arXiv:1308.0161 [astro-ph.HE].

[86] E. Fermi. "On the Origin of the Cosmic Radiation". In: *Physical Review* 75 (Apr. 1949), pp. 1169–1174. DOI: 10.1103/PhysRev.75.1169.

[87] V. P. Fomin et al. "New methods of atmospheric Cherenkov imaging for gamma-ray astronomy. I. The false source method". In: *Astroparticle Physics* 2 (May 1994), pp. 137–150. DOI: 10.1016/0927-6505(94)90036-1.

[88] G. Fossati et al. "A unifying view of the spectral energy distributions of blazars". In: *Monthly Notices of the RAS* 299 (Sept. 1998), pp. 433–448. DOI: 10.1046/j.1365-8711.1998.01828.x. eprint: arXiv:astro-ph/9804103.

[89] A. Franceschini, G. Rodighiero, and M. Vaccari. "Extragalactic optical-infrared background radiation, its time evolution and the cosmic photon-photon opacity". In: *Astronomy and Astrophysics* 487 (Sept. 2008), pp. 837–852. DOI: 10.1051/0004-6361:200809691. arXiv:0805.1841.

[90] L. Fuhrmann et al. "Simultaneous Radio to (Sub-) mm-Monitoring of Variability and Spectral Shape Evolution of potential GLAST Blazars". In: *The First GLAST Symposium*. Ed. by S. Ritz, P. Michelson, and C. A. Meegan. Vol. 921. American Institute of Physics Conference Series. July 2007, pp. 249–251. DOI: 10.1063/1.2757314. arXiv:0704.3944.

[91] H. Gast et al. "Exploring the Galaxy at TeV energies: Latest results from the H.E.S.S. Galactic Plane Survey". In: *International Cosmic Ray Conference*. Vol. 7. International Cosmic Ray Conference. 2011. arXiv:1204.5860 [astro-ph.HE].

[92] G. Ghisellini, ed. *Radiative Processes in High Energy Astrophysics*. Vol. 873. Lecture Notes in Physics, Berlin Springer Verlag. 2013. DOI: 10.1007/978-3-319-00612-3. arXiv:1202.5949 [astro-ph.HE].

[93] G. Ghisellini and F. Tavecchio. "Canonical high-power blazars". In: *Monthly Notices of the RAS* 397 (Aug. 2009), pp. 985–1002. DOI: 10.1111/j.1365-2966.2009.15007.x. arXiv:0902.0793 [astro-ph.CO].

[94] G. Ghisellini and F. Tavecchio. "The blazar sequence: a new perspective". In: *Monthly Notices of the RAS* 387 (July 2008), pp. 1669–1680. DOI: 10.1111/j.1365-2966.2008.13360.x. arXiv:0802.1918.

[95] G. Ghisellini, F. Tavecchio, and M. Chiaberge. "Structured jets in TeV BL Lac objects and radiogalaxies. Implications for the observed properties". In: *Astronomy and Astrophysics* 432 (Mar. 2005), pp. 401–410. DOI: 10.1051/0004-6361:20041404. eprint: astro-ph/0406093.

[96] P. Giommi et al. "A simplified view of blazars: clearing the fog around long-standing selection effects". In: *Monthly Notices of the RAS* 420 (Mar. 2012), pp. 2899–2911. DOI: 10.1111/j.1365-2966.2011.20044.x. arXiv:1110.4706 [astro-ph.CO].

[97] P. Giommi et al. "Simultaneous Planck, Swift, and Fermi observations of X-ray and γ-ray selected blazars". In: *Astronomy and Astrophysics* 541, A160 (May 2012), A160. DOI: 10.1051/0004-6361/201117825. arXiv:1108.1114 [astro-ph.CO].

[98] F. Goebel et al. "Upgrade of the MAGIC Telescope with a Multiplexed Fiber-Optic 2GSamples/s FADC Data Acquisition System system". In: *International Cosmic Ray Conference* 3 (2008), pp. 1481–1484.

[99] K. Greisen. "End to the Cosmic-Ray Spectrum?" In: *Phys. Rev. Lett.* 16 (17 Apr. 1966), pp. 748–750. DOI: 10.1103/PhysRevLett.16.748. URL: http://link.aps.org/doi/10.1103/PhysRevLett.16.748.

[100] R. C. Hartman et al. "Day-Scale Variability of 3C 279 and Searches for Correlations in Gamma-Ray, X-Ray, and Optical Bands". In: *Astrophysical Journal* 558 (Sept. 2001), pp. 583–589. DOI: 10.1086/322462. eprint: astro-ph/0105247.

[101] R. C. Hartman et al. "Detection of high-energy gamma radiation from quasar 3C 279 by the EGRET telescope on the Compton Gamma Ray Observatory". In: *Astrophysical Journal, Letters* 385 (Jan. 1992), pp. L1–L4. DOI: 10.1086/186263.

[102] R. C. Hartman et al. "Multiepoch Multiwavelength Spectra and Models for Blazar 3C 279". In: *Astrophysical Journal* 553 (June 2001), pp. 683–694. DOI: 10.1086/320970. eprint: arXiv:astro-ph/0102127.

[103] R. C. Hartman et al. "Simultaneous Multiwavelength Spectrum and Variability of 3C 279 from 10 9 to 10 24 Hz". In: *Astrophysical Journal* 461 (Apr. 1996), p. 698. DOI: 10.1086/177095.

[104] R. C. Hartman et al. "The Third EGRET Catalog of High-Energy Gamma-Ray Sources". In: *Astrophysical Journal, Supplement* 123 (July 1999), pp. 79–202. DOI: 10.1086/313231.

[105] M. G. Hauser and E. Dwek. "The Cosmic Infrared Background: Measurements and Implications". In: *Annual Review of Astron and Astrophys* 39 (2001), pp. 249–307. DOI: 10.1146/annurev.astro.39.1.249. eprint: astro-ph/0105539.

[106] M. G. Hauser et al. "The COBE Diffuse Infrared Background Experiment Search for the Cosmic Infrared Background. I. Limits and Detections". In: *Astrophysical Journal* 508 (Nov. 1998), pp. 25–43. DOI: 10.1086/306379. eprint: astro-ph/9806167.

[107] M. Hayashida et al. "The Structure and Emission Model of the Relativistic Jet in the Quasar 3C 279 Inferred from Radio to High-energy γ-Ray Observations in 2008-2010". In: *Astrophysical Journal* 754, 114 (Aug. 2012), p. 114. DOI: 10.1088/0004-637X/754/2/114. arXiv:1206.0745 [astro-ph.HE].

[108] W. Heitler. *The Quantum Theory of Radiation*. 1960.

[109] H.E.S.S. Collaboration et al. "H.E.S.S. discovery of VHE γ-rays from the quasar PKS 1510-089". In: *Astronomy and Astrophysics* 554, A107 (June 2013), A107. DOI: 10.1051/0004-6361/201321135. arXiv:1304.8071 [astro-ph.HE].

[110] J. W. T. Hessels et al. "PSR J1856+0245: Arecibo Discovery of a Young, Energetic Pulsar Coincident with the TeV γ-Ray Source HESS J1857+026". In: *Astrophysical Journal, Letters* 682 (July 2008), pp. L41–L44. DOI: 10.1086/590908. arXiv:0806.1200.

[111] A. M. Hillas. "Evolution of ground-based gamma-ray astronomy from the early days to the Cherenkov Telescope Arrays". In: *Astroparticle Physics* 43 (Mar. 2013), pp. 19–43. DOI: 10.1016/j.astropartphys.2012.06.002.

[112] J. A. Hinton and W. Hofmann. "Teraelectronvolt Astronomy". In: *Annual Review of Astron and Astrophys* 47 (Sept. 2009), pp. 523–565. DOI: 10.1146/annurev-astro-082708-101816. arXiv:1006.5210 [astro-ph.HE].

[113] D. C. Homan et al. "Parsec-Scale Blazar Monitoring: Proper Motions". In: *Astrophysical Journal* 549 (Mar. 2001), pp. 840–861. DOI: 10.1086/319466. eprint: astro-ph/0009301.

[114] D. C. Homan et al. "PKS 1510-089: A Head-on View of a Relativistic Jet". In: *Astrophysical Journal* 580 (Dec. 2002), pp. 742–748. DOI: 10.1086/343894. eprint: astro-ph/0208065.

[115] D. Horan et al. "Constraints on the Very High Energy Emission from BL Lacertae Objects". In: *Astrophysical Journal* 603 (Mar. 2004), pp. 51–61. DOI: 10.1086/381430. eprint: astro-ph/0311397.

[116] IceCube Collaboration et al. "The IceCube Neutrino Observatory Part I: Point Source Searches". In: *ArXiv e-prints* (Sept. 2013). arXiv:1309.6979 [astro-ph.HE].

[117] S. Inoue and F. Takahara. "Electron Acceleration and Gamma-Ray Emission from Blazars". In: *Astrophysical Journal* 463 (June 1996), p. 555. DOI: 10.1086/177270.

[118] H. L. Johnson. "Interstellar Extinction in the Galaxy." In: *Astrophysical Journal* 141 (Apr. 1965), p. 923. DOI: 10.1086/148186.

[119] S. G. Jorstad et al. "Polarimetric Observations of 15 Active Galactic Nuclei at High Frequencies: Jet Kinematics from Bimonthly Monitoring with the Very Long Baseline Array". In: *Astronomical Journal* 130 (Oct. 2005), pp. 1418–1465. DOI: 10.1086/444593. eprint: arXiv:astro-ph/0502501.

[120] K.-H. Kampert and P. Tinyakov. "Cosmic rays from the ankle to the cutoff". In: *Comptes Rendus Physique* 15 (Apr. 2014), pp. 318–328. DOI: 10.1016/j.crhy.2014.04.006. arXiv:1405.0575 [astro-ph.HE].

[121] K. Katarzyński, H. Sol, and A. Kus. "The multifrequency emission of Mrk 501. From radio to TeV gamma-rays". In: *Astronomy and Astrophysics* 367 (Mar. 2001), pp. 809–825. DOI: 10.1051/0004-6361:20000538.

[122] E. Kido, O. E. Kalashev, and for the Telescope Array Collaboration. "Constraining UHECR source models by the TA SD energy spectrum". In: *ArXiv e-prints* (Oct. 2013). arXiv:1310.6093 [astro-ph.HE].

[123] M. Kino and N. Kawakatu. "Estimate of the total kinetic power and age of an extragalactic jet by its cocoon dynamics: the case of Cygnus A". In: *Monthly Notices of the RAS* 364 (Dec. 2005), pp. 659–664. DOI: 10.1111/j.1365-2966.2005.09580.x. eprint: arXiv:astro-ph/0506626.

[124] M. Kino, F. Takahara, and M. Kusunose. "Energetics of TeV Blazars and Physical Constraints on Their Emission Regions". In: *Astrophysical Journal* 564 (Jan. 2002), pp. 97–107. DOI: 10.1086/323363. eprint: arXiv:astro-ph/0107436.

[125] S. Klepser. "A generalized likelihood ratio test statistic for Cherenkov telescope data". In: *Astroparticle Physics* 36 (Aug. 2012), pp. 64–76. DOI: 10.1016/j.astropartphys.2012.04.008. arXiv:1112.0786 [astro-ph.IM].

[126] T.-P. Li and Y.-Q. Ma. "Analysis methods for results in gamma-ray astronomy". In: *Astrophysical Journal* 272 (Sept. 1983), pp. 317–324. DOI: 10.1086/161295.

[127] M. S. Longair. *High energy astrophysics*. Mar. 1992.

[128] C. R. Lynds, A. N. Stockton, and W. C. Livingston. "New Spectroscope Observations of Quasi-Stellar Sources." In: *Astrophysical Journal* 142 (Nov. 1965), p. 1667. DOI: 10.1086/148457.

[129] F. Makino et al. "X-ray outburst of the quasar 3C 279". In: *Astrophysical Journal, Letters* 347 (Dec. 1989), pp. L9–L12. DOI: 10.1086/185594.

[130] M. A. Malkan and R. L. Moore. "The ultraviolet excess of quasars. III - The highly polarized quasars PKS 0736 + 017 and PKS 1510 - 089". In: *Astrophysical Journal* 300 (Jan. 1986), pp. 216–223. DOI: 10.1086/163796.

[131] K. Mannheim. "The proton blazar". In: *Astronomy and Astrophysics* 269 (Mar. 1993), pp. 67–76. eprint: arXiv:astro-ph/9302006.

[132] K. Mannheim, P. L. Biermann, and W. M. Kruells. "A novel mechanism for nonthermal X-ray emission". In: *Astronomy and Astrophysics* 251 (Nov. 1991), pp. 723–731.

[133] L. Maraschi, G. Ghisellini, and A. Celotti. "A jet model for the gamma-ray emitting blazar 3C 279". In: *Astrophysical Journal, Letters* 397 (Sept. 1992), pp. L5–L9. DOI: 10.1086/186531.

[134] L. Maraschi and F. Tavecchio. "The Jet-Disk Connection and Blazar Unification". In: *Astrophysical Journal* 593 (Aug. 2003), pp. 667–675. DOI: 10.1086/342118. eprint: arXiv:astro-ph/0205252.

[135] L. Maraschi et al. "The 1993 multiwavelength campaign on 3C 279: The radio to gamma-ray energy distribution inlow state". In: *Astrophysical Journal, Letters* 435 (Nov. 1994), pp. L91–L95. DOI: 10.1086/187602.

[136] M. Mariotti. "MAGIC discovers VHE gamma-ray emission from the blazar 1ES 1727+502". In: *The Astronomer's Telegram* 3774 (Nov. 2011), p. 1.

[137] M. Mariotti. "VHE detection of the blazar 1ES 0033+595 by MAGIC". In: *The Astronomer's Telegram* 3719 (Oct. 2011), p. 1.

[138] A. P. Marscher. "Turbulent, Extreme Multi-zone Model for Simulating Flux and Polarization Variability in Blazars". In: *Astrophysical Journal* 780, 87 (Jan. 2014), p. 87. DOI: 10.1088/0004-637X/780/1/87. arXiv:1311.7665 [astro-ph.HE].

[139] A. P. Marscher et al. "Probing the Inner Jet of the Quasar PKS 1510-089 with Multi-Waveband Monitoring During Strong Gamma-Ray Activity". In: *Astrophysical Journal, Letters* 710 (Feb. 2010), pp. L126–L131. DOI: 10.1088/2041-8205/710/2/L126. arXiv:1001.2574 [astro-ph.CO].

[140] A. Mastichiadis and J. G. Kirk. "Variability in the synchrotron self-Compton model of blazar emission." In: *Astronomy and Astrophysics* 320 (Apr. 1997), pp. 19–25. eprint: astro-ph/9610058.

[141] D. Mazin and M. Raue. "New limits on the density of the extragalactic background light in the optical to the far infrared from the spectra of all known TeV blazars". In: *Astronomy and Astrophysics* 471 (Aug. 2007), pp. 439–452. DOI: 10.1051/0004-6361:20077158. eprint: astro-ph/0701694.

[142] D. Mazin et al. "Potential of EBL and cosmology studies with the Cherenkov Telescope Array". In: *Astroparticle Physics* 43 (Mar. 2013), pp. 241–251. DOI: 10.1016/j.astropartphys.2012.09.002. arXiv:1303.7124 [astro-ph.CO].

[143] M. Meyer et al. "Limits on the extragalactic background light in the Fermi era". In: *Astronomy and Astrophysics* 542, A59 (June 2012), A59. DOI: 10.1051/0004-6361/201118284. arXiv:1202.2867.

[144] R. Mirzoyan. "Discovery of Very High Energy Gamma-Ray Emission From Gravitationally Lensed Blazar S3 0218+357 With the MAGIC Telescopes". In: *The Astronomer's Telegram* 6349 (July 2014), p. 1.

[145] A. Moralejo et al. "MARS, the MAGIC Analysis and Reconstruction Software". In: *ArXiv e-prints* (July 2009). arXiv:0907.0943 [astro-ph.IM].

[146] D. Moro and U. Munari. "The Asiago Database on Photometric Systems (ADPS). I. Census parameters for 167 photometric systems". In: *Astronomy and Astrophysics, Supplement* 147 (Dec. 2000), pp. 361–628. DOI: 10.1051/aas:2000370.

[147] A. Mücke and R. J. Protheroe. "A proton synchrotron blazar model for flaring in Markarian 501". In: *Astroparticle Physics* 15 (Mar. 2001), pp. 121–136. DOI: 10.1016/S0927-6505(00)00141-9. eprint: astro-ph/0004052.

[148] A. Mücke et al. "BL Lac objects in the synchrotron proton blazar model". In: *Astroparticle Physics* 18 (Mar. 2003), pp. 593–613. DOI: 10.1016/S0927-6505(02)00185-8. eprint: astro-ph/0206164.

[149] A. Mücke et al. "Monte Carlo simulations of photohadronic processes in astrophysics". In: *Computer Physics Communications* 124 (Feb. 2000), pp. 290–314. DOI: 10.1016/S0010-4655(99)00446-4. eprint: astro-ph/9903478.

[150] K. Nalewajko. "Polarization Swings from Curved Trajectories of the Emitting Regions". In: *International Journal of Modern Physics D* 19 (2010), pp. 701–706. DOI: 10.1142/S0218271810016853. arXiv:1208.5472 [astro-ph.HE].

[151] K. Nalewajko et al. "Herschel PACS and SPIRE Observations of Blazar PKS 1510-089: A Case for Two Blazar Zones". In: *Astrophysical Journal* 760, 69 (Nov. 2012), p. 69. DOI: 10.1088/0004-637X/760/1/69. arXiv:1210.4552 [astro-ph.HE].

[152] P. L. Nolan et al. "Fermi Large Area Telescope Second Source Catalog". In: *Astrophysical Journal, Supplement* 199, 31 (Apr. 2012), p. 31. DOI: 10.1088/0067-0049/199/2/31. arXiv:1108.1435 [astro-ph.HE].

[153] M. Orienti et al. "Radio and γ-ray follow-up of the exceptionally high-activity state of PKS 1510-089 in 2011". In: *Monthly Notices of the RAS* 428 (Jan. 2013), pp. 2418–2429. DOI: 10.1093/mnras/sts201. arXiv:1210.4319 [astro-ph.HE].

[154] M. R. Orr, F. Krennrich, and E. Dwek. "Strong New Constraints on the Extragalactic Background Light in the Near- to Mid-infrared". In: *Astrophysical Journal* 733, 77 (June 2011), p. 77. DOI: 10.1088/0004-637X/733/2/77. arXiv:1101.3498 [astro-ph.CO].

[155] B. M. Peterson. *An Introduction to Active Galactic Nuclei*. Feb. 1997.

[156] M. Pohl and R. Schlickeiser. "On the conversion of blast wave energy into radiation in active galactic nuclei and gamma-ray bursts". In: *Astronomy and Astrophysics* 354 (Feb. 2000), pp. 395–410. eprint: astro-ph/9911452.

[157] J. Poutanen and B. Stern. "GeV Breaks in Blazars as a Result of Gamma-ray Absorption Within the Broad-line Region". In: *Astrophysical Journal, Letters* 717 (July 2010), pp. L118–L121. DOI: 10.1088/2041-8205/717/2/L118. arXiv:1005.3792 [astro-ph.HE].

[158] E. Prandini. "TeV observations of blazars and constraints on their redshifts: a detailed study of PG 1553+113 and PKS 1424+240 with MAGIC". PhD thesis. PhD Thesis, Universitatá degli Studi di Padova, 2011.

[159] R. J. Protheroe and R. W. Clay. "Ultra High Energy Cosmic Rays". In: *Publications of the Astron. Soc. of Australia* 21 (2004), pp. 1–22. DOI: 10.1071/AS03047. eprint: astro-ph/0311466.

[160] M. Punch et al. "Detection of TeV photons from the active galaxy Markarian 421". In: *Nature* 358 (Aug. 1992), p. 477. DOI: 10.1038/358477a0.

[161] J. Quinn et al. "Detection of Gamma Rays with E > 300 GeV from Markarian 501". In: *Astrophysical Journal, Letters* 456 (Jan. 1996), p. L83. DOI: 10.1086/309878.

[162] F. M. Rieger, E. de Oña-Wilhelmi, and F. A. Aharonian. "TeV astronomy". In: *Frontiers of Physics* 8 (Dec. 2013), pp. 714–747. DOI: 10.1007/s11467-013-0344-6. arXiv:1302.5603 [astro-ph.HE].

[163] W. A. Rolke, A. M. López, and J. Conrad. "Limits and confidence intervals in the presence of nuisance parameters". In: *Nuclear Instruments and Methods in Physics Research A* 551 (Oct. 2005), pp. 493–503. DOI: 10.1016/j.nima.2005.05.068. eprint: arXiv:physics/0403059.

[164] G. B. Rybicki and A. P. Lightman. *Radiative processes in astrophysics*. 1979.

[165] S. Saito et al. "Very Rapid High-amplitude Gamma-Ray Variability in Luminous Blazar PKS 1510-089 Studied with Fermi-LAT". In: *Astrophysical Journal, Letters* 766, L11 (Mar. 2013), p. L11. DOI: 10.1088/2041-8205/766/1/L11. arXiv:1302.0335 [astro-ph.HE].

[166] R. T. Schilizzi et al. "VLBI, MERLIN and HST observations of the giant radio galaxy 3C 236". In: *Astronomy and Astrophysics* 368 (Mar. 2001), pp. 398–407. DOI: 10.1051/0004-6361:20000288. eprint: arXiv:astro-ph/0012231.

[167] C. K. Seyfert. "Nuclear Emission in Spiral Nebulae." In: *Astrophysical Journal* 97 (Jan. 1943), p. 28. DOI: 10.1086/144488.

[168] M. Sikora, M. C. Begelman, and M. J. Rees. "Comptonization of diffuse ambient radiation by a relativistic jet: The source of gamma rays from blazars?" In: *Astrophysical Journal* 421 (Jan. 1994), pp. 153–162. DOI: 10.1086/173633.

[169] M. Sikora and G. Madejski. "On Pair Content and Variability of Subparsec Jets in Quasars". In: *Astrophysical Journal* 534 (May 2000), pp. 109–113. DOI: 10.1086/308756. eprint: arXiv:astro-ph/9912335.

[170] M. Sikora et al. "Are Quasar Jets Dominated by Poynting Flux?" In: *Astrophysical Journal* 625 (May 2005), pp. 72–77. DOI: 10.1086/429314. eprint: astro-ph/0502115.

[171] M. Sikora et al. "Electron injection by relativistic protons in active galactic nuclei". In: *Astrophysical Journal, Letters* 320 (Sept. 1987), pp. L81–L85. DOI: 10.1086/184980.

[172] J. Sitarek et al. "Analysis techniques and performance of the Domino Ring Sampler version 4 based readout for the MAGIC telescopes". In: *Nuclear Instruments and Methods in Physics Research A* 723 (Sept. 2013), pp. 109–120. DOI: 10.1016/j.nima.2013.05.014. arXiv:1305.1007 [astro-ph.IM].

[173] J. Sitarek et al. "Physics performance of the upgraded MAGIC telescopes obtained with Crab Nebula data". In: *ArXiv e-prints*. International Cosmic Ray Conference (Aug. 2013). arXiv:1308.0141 [astro-ph.IM].

[174] P. Sreekumar et al. "EGRET Observations of the North Galactic Pole Region". In: *Astrophysical Journal* 464 (June 1996), p. 628. DOI: 10.1086/177352.

[175] F. W. Stecker, O. C. de Jager, and M. H. Salamon. "TeV gamma rays from 3C 279 - A possible probe of origin and intergalactic infrared radiation fields". In: *Astrophysical Journal, Letters* 390 (May 1992), pp. L49–L52. DOI: 10.1086/186369.

[176] H. S. Stockman, R. L. Moore, and J. R. P. Angel. "The optical polarization properties of 'normal' quasars". In: *Astrophysical Journal* 279 (Apr. 1984), pp. 485–498. DOI: 10.1086/161912.

[177] C. N. Tadhunter et al. "Optical Spectroscopy of a Complete Sample of Southern 2-JY Radio Sources". In: *Monthly Notices of the RAS* 263 (Aug. 1993), p. 999.

[178] M. Tavani et al. "Discovery of Powerful Gamma-Ray Flares from the Crab Nebula". In: *Science* 331 (Feb. 2011), pp. 736–. DOI: 10.1126/science.1200083. arXiv:1101.2311 [astro-ph.HE].

[179] M. Tavani et al. "The AGILE Mission". In: *Astronomy and Astrophysics* 502 (Aug. 2009), pp. 995–1013. DOI: 10.1051/0004-6361/200810527. arXiv:0807.4254.

[180] F. Tavecchio, L. Maraschi, and G. Ghisellini. "Constraints on the Physical Parameters of TeV Blazars". In: *Astrophysical Journal* 509 (Dec. 1998), pp. 608–619. DOI: 10.1086/306526. eprint: arXiv:astro-ph/9809051.

[181] F. Tavecchio et al. "TeV BL Lac objects at the dawn of the Fermi era". In: *Monthly Notices of the RAS* 401 (Jan. 2010), pp. 1570–1586. DOI: 10.1111/j.1365-2966.2009.15784.x. arXiv:0909.0651 [astro-ph.HE].

[182] A. M. Taylor, I. Vovk, and A. Neronov. "Extragalactic magnetic fields constraints from simultaneous GeV-TeV observations of blazars". In: *Astronomy and Astrophysics* 529, A144 (May 2011), A144. DOI: 10.1051/0004-6361/201116441. arXiv:1101.0932 [astro-ph.HE].

[183] D. Tescaro et al. "The readout system of the MAGIC-II Cherenkov Telescope". In: *ArXiv e-prints* (July 2009). arXiv:0907.0466 [astro-ph.IM].

[184] D. J. Thompson et al. "EGRET observations of active galactic nuclei - 0836 + 710, 0454 - 234, 0804 + 499, 0906 + 430, 1510-089, and 2356 + 196". In: *Astrophysical Journal, Letters* 415 (Sept. 1993), pp. L13–L16. DOI: 10.1086/187021.

[185] S. C. Unwin et al. "Superluminal motion in the quasar 3C 279". In: *Astrophysical Journal* 340 (May 1989), pp. 117–128. DOI: 10.1086/167379.

[186] C. M. Urry and P. Padovani. "Unified Schemes for Radio-Loud Active Galactic Nuclei". In: *Publications of the ASP* 107 (Sept. 1995), p. 803. DOI: 10.1086/133630. eprint: arXiv:astro-ph/9506063.

[187] F. Vagnetti, A. Cavaliere, and E. Giallongo. "BL Lacertae objects and radio-loud quasars within an evolutionary unified scheme". In: *Astrophysical Journal* 368 (Feb. 1991), pp. 366–372. DOI: 10.1086/169700.

[188] S. I. Vavilov. " " In: *C. R. Acad. Sci. U.S.S.R. - Doklady Akad. Nauk SSSR* 8 (1934), p. 457.

[189] VERITAS Collaboration et al. "A connection between star formation activity and cosmic rays in the starburst galaxy M82". In: *Nature* 462 (Dec. 2009), pp. 770–772. DOI: 10.1038/nature08557. arXiv:0911.0873 [astro-ph.CO].

[190] VERITAS Collaboration et al. "Detection of Pulsed Gamma Rays Above 100 GeV from the Crab Pulsar". In: *Science* 334 (Oct. 2011), pp. 69–. DOI: 10.1126/science.1208192. arXiv:1108.3797 [astro-ph.HE].

[191] T. C. Weekes et al. "Observation of TeV gamma rays from the Crab nebula using the atmospheric Cerenkov imaging technique". In: *Astrophysical Journal* 342 (July 1989), pp. 379–395. DOI: 10.1086/167599.

[192] A. E. Wehrle et al. "Kinematics of the Parsec-Scale Relativistic Jet in Quasar 3C 279: 1991-1997". In: *Astrophysical Journal, Supplement* 133 (Apr. 2001), pp. 297–320. DOI: 10.1086/320353. eprint: astro-ph/0008458.

[193] A. E. Wehrle et al. "Multiwavelength Observations of a Dramatic High-Energy Flare in the Blazar 3C 279". In: *Astrophysical Journal* 497 (Apr. 1998), p. 178. DOI: 10.1086/305461. eprint: arXiv:astro-ph/9711243.

[194] M. Weidinger, M. Rüger, and F. Spanier. "Modelling the steady state spectral energy distribution of the BL-Lac Object PKS 2155-30.4 using a selfconsistent SSC model". In: *Astrophysics and Space Sciences Transactions* 6 (Jan. 2010), pp. 1–7. DOI: 10.5194/astra-6-1-2010. arXiv:1001.2145 [astro-ph.HE].

[195] M. Weidinger and F. Spanier. "Variability along the Blazar-Sequence - Hints for extragalactic Cosmic Rays?" In: International Cosmic Ray Conference 6 (Aug. 2011). eprint: 1109.1975 (astro-ph.HE).

[196] A. R. Whitney et al. "Quasars Revisited: Rapid Time Variations Observed Via Very-Long-Baseline Interferometry". In: *Science* 173 (July 1971), pp. 225–230. DOI: 10.1126/science.173.3993.225.

[197] R. Zanin. "Observation of the Crab pulsar wind nebula and microquasar candidates with MAGIC". PhD thesis. PhD Thesis, Universitat Autònoma de Barcelona, 2011.

[198] G. T. Zatsepin and V. A. Kuz'min. "Upper Limit of the Spectrum of Cosmic Rays". In: *Soviet Journal of Experimental and Theoretical Physics Letters* 4 (Aug. 1966), p. 78.

[199] E. G. Zweibel and M. Yamada. "Magnetic Reconnection in Astrophysical and Laboratory Plasmas". In: *Annual Review of Astron and Astrophys* 47 (Sept. 2009), pp. 291–332. DOI: 10.1146/annurev-astro-082708-101726.

Acknowledgements

I would like to thank my supervisor, Elisa Bernardini, for her guidance and for the opportunities she gave me during these years. Deepest thanks to my co-supervisor, office mate and friend Rebecca Gozzini for her continous support and infinite patience. I am very grateful to Kathin Mallot for her advices and all the proof readings. Many thanks also to Konstancja Satalecka for her support during the initial phase of my PhD.

I am immensely grateful to Elina Lindfors for all her good avdices and for her constant availability. Many thanks to Fabrizio Tavecchio for all the discussions, to Karsten Berger for his constant help and for sharing with me the work on 1ES 1727+502. Special thanks to all the collaborators I worked with on the publications on 3C 279 and PKS 1510-089, Julian Sitarek for his technical advices, Cornelia Schultz for being my cross-checker and proof-reader, Ulisses Barres de Almeida and Koji Saito. Many thanks to Saverio Lombardi and Abelardo Moralejo for their technical help.

I am deeply grateful to the MAGIC group in Udine for introducing me to the MAGIC collaboration and the world of astrophysics.

Special thanks to all my shift companions for all our adventures in La Palma and to Gianluca Giavitto for his patience.

I am very grateful to all the members of the MAGIC collaboration for the unforgetable experiences we shared. I would also like to thank the whole astroparticle group at DESY Zeuthen for making my PhD time special.

Last, I would like to deeply thank my family for making all this possible and to Andrea for being always at my side.

Selbständigkeitserklärung

Hiermit erkläre ich, dass ich diese Arbeit selbstständig ohne fremde Hilfe verfasst und keine anderen als die angegeben Literatur und Hilfsmittel benutzt habe.

Gessica De Caneva

Berlin, 6.10.2014

List of Publications

Publications as corresponding author

1. MAGIC gamma-ray and multi-frequency observations of flat spectrum radio quasar PKS 1510-089 in early 2012, Aleksić et al., Astronomy & Astrophysics (2014), 569, A46

2. MAGIC observations and multifrequency properties of the flat spectrum radio quasar 3C 279 in 2011, Aleksić et al., Astronomy & Astrophysics (2014), 567, A41

3. Discovery of very high energy gamma-ray emission from the blazar 1ES 1727+ 502 with the MAGIC Telescopes, Aleksić et al., Astronomy & Astrophysics (2014), 563, A90

Publications as a member of the MAGIC Collaboration

1. The major upgrade of the MAGIC telescopes, Part I: The hardware improvements and the commissioning of the system, Aleksić et al., submitted to Astroparticle Physics (arXiv:1409.6073)

2. The major upgrade of the MAGIC telescopes, Part II: The achieved physics performance using the Crab Nebula observations, Aleksić et al., submitted to Astroparticle Physics (arXiv:1409.5594)

3. First broadband characterization and redshift determination of the VHE blazar MAGIC J2001+439, Aleksić et al., accepted for publication in Astronomy & Astrophysics (arXiv:1409.3389)

4. Probing the very-high-energy gamma-ray spectral curvature in the blazar PG 1553+113 with the MAGIC telescopes, Aleksić et al., (arXiv:1408.1975)

5. MAGIC search for VHE γ-ray emission from AE Aquarii in a multiwavelength context, Aleksić et al., Astronomy & Astrophysics (2014), 568, A109

6. Discovery of TeV γ-ray emission from the pulsar wind nebula 3C 58 by MAGIC, Aleksić et al., Astronomy & Astrophysics (2014), 567, L8

7. MAGIC long-term study of the distant TeV blazar PKS 1424+240 in a multiwavelength context, Aleksić et al., Astronomy & Astrophysics (2014), 567, A135

8. Measurement of the Crab Nebula spectrum over three decades in energy with the MAGIC telescopes, Aleksić et al., submitted to Journal of High Energy Astrophysics (arXiv:1406.6892)

9. Search for very high energy gamma-rays from the z = 0.896 quasar 4C +55.17 with the MAGIC telescopes, Aleksić et al., Monthly Notices of the RAS (2014), 440, 530

10. Multifrequency Studies of the Peculiar Quasar 4C +21.35 during the 2010 Flaring Activity, Ackermann et al., Astrophysical Journal (2014), 786, 157

11. Detection of bridge emission above 50 GeV from the Crab pulsar with the MAGIC telescopes, Aleksić et al., Astronomy & Astrophysics (2014), 565, L12

12. Contemporaneous observations of the radio galaxy NGC 1275 from radio to very high energy γ-rays, Aleksić et al., Astronomy & Astrophysics (2014), 564, A5

13. Rapid and multiband variability of the TeV bright active nucleus of the galaxy IC 310, Aleksić et al., Astronomy & Astrophysics (2014), 563, A91

14. MAGIC upper limits on the GRB 090102 afterglow, Aleksić et al., Monthly Notices of the RAS (2014), 437, 3103

15. Optimized dark matter searches in deep observations of Segue 1 with MAGIC, Aleksić et al., Journal of Cosmology and Astroparticle Physics (2014), 2, 8

16. MAGIC reveals a complex morphology within the unidentified gamma-ray source HESS J1857+026, Aleksić et al., accepted for publication in Astronomy & Astrophysics (arXiv:1401.7154)

17. The simultaneous low state spectral energy distribution of 1ES 2344+514 from radio to very high energies, Aleksić et al., Astronomy & Astrophysics (2013), 556, A67

18. Very high energy gamma-ray observation of the peculiar transient event Swift J1644+57 with the MAGIC telescopes and AGILE, Aleksić et al., Astronomy & Astrophysics (2013), 552, A112

19. Observations of the magnetars 4U 0142+61 and 1E 2259+586 with the MAGIC telescopes, Aleksić et al., Astronomy & Astrophysics (2013), 549, A23

20. Discovery of VHE γ-rays from the blazar 1ES 1215+303 with the MAGIC telescopes and simultaneous multi-wavelength observations, Aleksić et al., Astronomy & Astrophysics (2012), 544, A142

21. MAGIC observations of the giant radio galaxy M 87 in a low-emission state between 2005 and 2007, Aleksić et al., Astronomy & Astrophysics (2012), 544, A96

22. High zenith angle observations of PKS 2155-304 with the MAGIC-I telescope, Aleksić et al., Astronomy & Astrophysics (2012), 544, A75

23. Detection of VHE γ-Rays from HESS J0632+057 during the 2011 February X-Ray Outburst with the MAGIC Telescopes, Aleksić et al., Astrophysical Journal, Letters(2012), 754, L10

24. Mrk 421 active state in 2008: the MAGIC view, simultaneous multi-wavelength observations and SSC model constrained, Aleksić et al., Astronomy & Astrophysics (2012), 542, A100

25. Constraining cosmic rays and magnetic fields in the Perseus galaxy cluster with TeV observations by the MAGIC telescopes, Aleksić et al., Astronomy & Astrophysics (2012), 541, A99

26. Morphological and spectral properties of the W51 region measured with the MAGIC telescopes, Aleksić et al., Astronomy & Astrophysics (2012), 541, A13

27. Phase-resolved energy spectra of the Crab pulsar in the range of 50-400 GeV measured with the MAGIC telescopes, Aleksić et al., Astronomy & Astrophysics (2012), 540, A69

28. PG 1553+113: Five Years of Observations with MAGIC, Aleksić et al., Astrophysical Journal (2012), 748, 46

29. Detection of very-high energy γ-ray emission from NGC 1275 by the MAGIC telescopes, Aleksić et al., Astronomy & Astrophysics (2012), 539, L2.

30. Discovery of VHE γ-ray emission from the BL Lacertae object B3 2247+381 with the MAGIC telescopes, Aleksić et al., Astronomy & Astrophysics (2012), 539, A118

31. Detection of the γ-Ray Binary LS I +61deg303 in a Low-flux State at Very High Energy γ-Rays with the MAGIC Telescopes in 2009, Aleksić et al., Astrophysical Journal (2012), 746, 80

32. Performance of the MAGIC stereo system obtained with Crab Nebula data, Aleksić et al., Astroparticle Physics (2012), 35, 435

33. Observations of the Crab Pulsar between 25 and 100 GeV with the MAGIC I Telescope, Aleksić et al., Astrophysical Journal (2011), 742, 43

Conference proceedings

1. MAGIC latest results and multiwavelength observations of FSRQs: 3C 279 and PKS 1510-089, Presenter: Ulisses Barres de Almeida, talk at the *33rd International Cosmic Ray Conference, Rio de Janeiro (Brazil) - July 2013*, G. De Caneva *et al.*, Proc. preprint available at `http://143.107.180.38/indico/contributionDisplay.py?contribId=644&sessionId=3&confId=0`

2. MAGIC discovery and multiwavelength observations of the BL Lac 1ES 1727+502, Presenter: K. Berger, poster at the *33rd International Cosmic Ray Conference, Rio de Janeiro (Brazil) - July 2013*, K. Berger *et al.*, Proc. preprint available at arXiv:1308.3498 [astro-ph.HE]

3. The FSRQs 3C 279 and PKS 1510-089: MAGIC latest results and multiwavelength observations, Presenter: G. De Caneva, talk at the *HEPRO-IV Conference, Heidelberg (Germany) - July 2013*, G. De Caneva *et al.*, International Journal of Modern Physics Conference Series, 28, 60176

4. VHE gamma-ray emission from the FSRQs observed by the MAGIC telescopes, Presenter: E. Lindfors, talk at the *Fourth International Fermi Symposium, Monterey (California)- October 2012*, E. Lindfors *et al.*, Proc. preprint available at arXiv:1303.2102 [astro-ph.HE]

5. Flat Spectrum Radio Quasars: MAGIC results and unexpected features, Presenter: G. De Caneva, poster at the *Gamma2012 conference, Heidelberg (Germany) - July 2012*, G. De Caneva *et al.*, Proc. of the 5th International Meeting Eds. F.A. Aharonian, W. Hofmann and F.M. Rieger, American Institute of Physics Conference Series, 1505, 502

6. MAGIC discovery of the BL Lac 1ES 1727+502: multiwavelength observations, spectral behavior and variability, Presenter: G. De Caneva, poster at the *Gamma2012 conference, Heidelberg (Germany) - July 2012*, G. De Caneva

et al., Proc. of the 5th International Meeting Eds. F.A. Aharonian, W. Hofmann and F.M. Rieger, American Institute of Physics Conference Series, 1505, 526

7. Emission models and EBL as a tool to measure the redshift of BL Lac objects, Presenter: G. De Caneva, poster at the *32nd International Cosmic Ray Conference, Beijing (China)- August 2011*, N. Mankuzhiyil *et al.*, International Cosmic Ray Conference, 8, 167

Gessica De Caneva

Berlin, 6.10.2014